AlGaN UV Photodetectors: From micro to nano

A THESIS

SUBMITTED TO THE DEPARTMENT OF PHYSICS

AND THE GRADUATE SCHOOL OF ENGINEERING AND SCIENCES

OF BILKENT UNIVERSITY

IN PARTIAL FULFILLMENT OF THE REQUIREMENTS

FOR THE DEGREE OF

DOCTOR OF PHILOSOPHY

By

Serkan Bütün

December 2011

I certify that I have read this thesis and that in my opinion it is fully adequate, in scope and in quality, as a thesis for the degree of Doctor of Philosophy.

____

Prof. Dr. Ekmel Özbay (Supervisor)

I certify that I have read this thesis and that in my opinion it is fully adequate, in scope and in quality, as a thesis for the degree of Doctor of Philosophy.

____

Prof. Dr. Süleyman Özçelik

I certify that I have read this thesis and that in my opinion it is fully adequate, in scope and in quality, as a thesis for the degree of Doctor of Philosophy.

____

Assoc. Prof. Dr. Ceyhun Bulutay

I certify that I have read this thesis and that in my opinion it is fully adequate, in scope and in quality, as a thesis for the degree of Doctor of Philosophy.

____

Assoc. Prof. Dr. M. Özgür Oktel

I certify that I have read this thesis and that in my opinion it is fully adequate, in scope and in quality, as a thesis for the degree of Doctor of Philosophy.

____

Assit. Prof. Dr. Ali Kemal Okyay

Approved for the Graduate School of Engineering and Sciences:

____

Prof. Dr. Levent Onural

Director of Graduate School of Engineering and Sciences

ABSTRACT

AlGaN UV PHOTODETECTORS: FROM MICRO TO NANO

Serkan Bütün

PhD in Physics

Supervisor: Prof. Dr. Ekmel Özbay

December, 2011

The absorption edge of AlGaN based alloys can be tuned from deep UV to near UV by changing the composition. This enables the use of the material in various technological applications such as military, environmental monitoring and biological imaging. In this thesis, we proposed and demonstrated various UV photodetectors for different purposes. The multi-band photodetectors have the unique ability to sense the UV spectrum in different portions at the same time. We demonstrated monolithically integrated dual and four-band photodetectors with multi layer structures grown on sapphire. This was achieved through epitaxial growth of multi AlGaN layers with decreasing Al content. We suggested two different device architectures. First one has separate filter and active layers, whereas the second one has all active layers which are used as filter layers as well. The full width at half maximum (FWHM) values for the dual band photodetector was 11 and 22 nm with more than three orders of magnitude inter-band rejection ratio. The self-filtering four band photodetector has FWHMs of 18, 17, 22 and 9 nm from longer to shorter bands. Whereas photodetector with separate filter layers has FWHMs of 8, 12, 11 and 8 nm, from longer to shorter bands. The overall inter-band rejection ration was increased from about one to two of magnitude after incorporating the passive filter layers. The plasmonic enhancement of photonic devices has attracted much

attention for the past decade. However, there is not much research that has been conducted in UV region. In the second part of this thesis, we fabricated nano-structures on GaN based photodetectors and improved the responsivity of the device. We have fabricated Al nano-particles on sapphire with e-beam lithography. We characterized their response via spectral extinction measurements. We integrated these particles with GaN photodetectors and had enhancement of %50 at the plasmonic resonance of the nano-particles. Secondly, we have fabricated sub-wavelength photodetectors on GaN coupled with linear gratings. We had 8 fold enhancement in the responsivity at the plasmonic resonance frequency of the grating at normal incidence. Numerical simulations revealed that both surface plasmons and the unbound leaky surface waves played a role in the enhancement. We, finally, conducted basic research on the current transport mechanisms in Schottky barriers of AlGaN based materials. Experiments revealed that the tunneling current plays a major role in current transport. In addition incorporation, of a thin insulator between metal-semiconductor interface reduces the undesired surface states thereby improving the device performance.

Keywords: AlGaN, GaN, photodetector, multi-band, dual-band, MSM, Schottky, plasmonics, surface plasmon polariton, grating, nano-particle , localized surface plasmon resonance

ÖZET

AlGaN UV FOTODEDEKTÖRLER: MİKRODAN NANOYA

Serkan Bütün

Fizik doktora

Tez Yöneticisi: Prof. Dr. Ekmel Özbay

Aralık, 2011

AlGaN temelli alaşımların soğurma kesimi Al oranı değiştirilerek derin UV dalgaboylarından yakın UV dalgaboylarına kadar ayarlanabilir. Bu özellik, malzemeyi, askeri, çevresel ve biyolojik görüntüleme gibi pek çok teknolojik alanlarda kullanma imkanı sağlamaktadır. Bu çalışmamızda, farklı uygulamalara yönelik UV fotodedektörler tasarladık ve ürettik. Çoklu bantlarda soğurma yapabilen dedektörler UV ışığı farklı dalgaboylarında algılayabilmektedirler. Bu amaçla, tek seferde büyütülmüş çoklu AlGaN katmanları üzerinde iki ve dört bantlı fotodedektörler ürettik. Bu, yukarı doğru azalan Al oranlarında AlGaN katmanları büyütülerek sağlandı. İki farklı tipte aygıt tasarımı yapıldı. Birinci tipte fotodedektör dört aktif soğurma katmanından oluştu. Her katman aynı zamanda diğer bantlar için filtre görevi gördü. İkinci tipte ise, her bant için farklı Al oranında bir aktif soğuma ve bir pasif filtre katmanı vardı. İki bantlı fotodedektörün her bandı için yarı doruk genişliği (YDG) kısa ve uzun bantlar için sırasıyla 11 ve 22 nm olarak ölçüldü. Bantlar arası bin kattan fazla kontrast ölçüldü. Birinci tip dört bantlı fotodedektör uzun banttan kısa banda doğru 18, 17, 22 ve 9 nm YDG gösterirken ikinci tip dört bantlı fotodedektör 8, 12, 11 ve 8 nm YDG gösterdi. Ayrıca bantlar arası kontrast on kattan yüz kata çıktı. Fotonik aygıtların plazmonik yapılarla güçlendirilmesi geçtiğimiz on yıldır çok ilgi çekmektedir. Fakat UV bölgede, bu konuda yapılmış çalışma hemen hemen

hiç yoktur. Çalışmamızın ikinci kısmında ürettiğimiz çeşitli nano-yapıları GaN fotodedektörler ile bütünleştirdik ve fotodedektör cevabında bir iyileşme gözlemlerdik. Elektron mikroskobu ile safir üzerine Al nano-parçacıklar ürettik. Spektral geçirgenlik ölçümleri ile bu parçacıkların karakterizasyonu yaptık. Aynı nano-parçacıkları GaN fotodedektörler üzerine koyduğumuzda dedektör cevabında bir buçuk kata varan iyileşme gözlemledik. İkinci olarak, dalgaboyu altı fotodedektörler ürettik. Bu dedektörleri Al kırınım ağı ile bütünleştirdik. Kırınım ağının plasmonik çınlama dalgaboyu civarcında yüzeye dik aydınlatma ile fotodedektör cevabında sekiz kata varan bir iyileşme tespit ettik. Bilgisayar simülasyonları bu iyileşmenin hem yüzey plazmonlarına hem de yüzeyde oluşan sızıntı radyasyonuna bağlı olduğunu gösterdi. Son olarak AlGaN temelli malzemelerde Schottky tipi bariyerlerindeki akım mekanizmalarını inceleyen temel araştırmalar yaptık. Sonuçlara göre baskın akım mekanizmasının tünelleme akımı olduğu tespit edildi. Ayrıca metal-yarıiletken arayüzüne koyulacak ince yalıtkan katmanların istenmeyen ara-yüzey enerji seviyelerini düşürdüğü ve bu sayede aygıt performansını artırdığı gözlenmiştir.

Anahtar sözcükler: AlGaN, GaN, photodetector, çoklu bant, iki-bant, MSM, Schottky, plazmonik, yüzey plazmon polaritonları, kırınım ağı, nano-parçacık, sınırlandırılmış yüzey plazmon çınlamaları.

Acknowledgements

I am honored to present my sincere gratitude to my supervisor Prof. Dr. Ekmel Özbay for his endless support, guidance, motivation and encouragement during this research. I was a life time experience and such a great honor to work with him.

I would like to thank to Prof. Dr. Süleyman Özçelik, Assoc. Prof. Dr. Ceyhun Bulutay, Assoc. Prof. Dr. Mehmet Özgür Oktel, and Asst. Prof. Dr. Ali Kemal Okyay for being in my thesis committee. I am grateful for their valuable time and comments for evaluating this thesis.

I would like to thank to all the former and present personnel of the Nanotechnology Research Center for being good friends, understanding and making life easier. I would like to thank specifically Dr. Mutlu Gökkavas for his help, valuable experiences and suggestions especially in multi color photodetector work. I am indepted to Mrs. Neval Ayşegül Cinel for her help in simulations of the plasmonic structures. I would also like to thank Dr. HongBo Yu on behalf of the MOCVD team. This work would not be possible without their efforts. I appreciate the efforts of Dr. Engin Arslan in our work on Schottky barriers for modeling our measurements.

I also would like to mention the help of some people in Semiconductor Technologies Advanced Research Lab of Gazi University, Prof. Dr. Semsettin Altındal, Dr. Sefer Bora Lişesivdin, Mrs. Yasemin Safak, Mrs. Habibe Uslu and Mr. Ilke Tasçıoglu for their parts in C-V measurements as well as comments in our collaborations.

I also thank to all the former and present faculty members and personnel of the Advanced Research Laboratory and the Department of Physics. It was an honor to work aside with these hardworking people. Another special thank goes here to Mr. Murat Güre and Ergun Kahraman for their technical support and guidance in the laboratory.

I hereby would like to acknowledge and extend my heartfelt gratitude to the following persons with whom I made personal acquaintance with in Özbay group, Advanced Research Laboratory and the department of Physics during my Ph.D. Dr. Dündar Yılmaz, Dr. Koray Aydın, Dr. Hümeyra Çağlayan, Dr. Bayram Bütün, Dr. Turgut Tut, Dr. Kamil Boratay Alıcı, Dr. Funda Tamara Gündoğdu, Dr. Irfan Bulu, Dr. Aşkın Kocabaş, Mr. Deniz Çalışkan, Mr. Atilla Özgür Çakmak, Mr. Evrim Çolak, Mr. Hüseyin Çakmak, Mr, Semih Çakmakyapan, Mr. Özgür Kazar, Mr. Erkin Ülker, Mr. Mustafa Öztürk, Mrs. Pakize Demirel and many more, I thank you all for your friendship and valuable suggestions.

I am indebted to my parents and my brother for their love, encouragement and support.

Finally, I dedicate this work to my wife and my son. I am so much thankful for their love, endless trust and bringing joy to my life.

Contents

ABSTRACT .... **iii**

ÖZET .... **v**

Acknowledgements .... **vii**

Contents .... **ix**

List of Figures .... **xiii**

List of Tables .... **xvi**

Chapter 1 Introduction **1**

1.1 Motivation 4

1.2 Organization of the thesis 5

Chapter 2 Theoretical Background **6**

2.1 A brief introduction to semiconductor physics 6

2.1.1 Electrical properties 6

2.1.2 Optical properties 8

2.1.3 The Schottky Junction 9

2.2 MSM photodetectors 11

2.2.1 Characterization of the photodetectors 12

2.3 Fundamentals of surface plasmon polaritons 13

2.3.1 Surface plasmon polaritons 13

2.3.2 Localized surface plasmon resonance 17

Chapter 3 Multi-color Sensitive Photodetectors **20**

3.1 Introduction 20
3.2 Dual-Color sensing UV photodetectors 21
3.2.1 Concept 22
3.2.2 Fabrication and Results 23
3.2.3 Conclusion 30
3.3 Four-Color sensing UV photodetectors 31
3.3.1 Concept 32
3.3.2 Fabrication and Results 32
3.3.3 Conclusion 42
3.4 Four-Color sensing UV photodetectors with extra filter layers 42
3.4.1 Concept 43
3.4.2 Fabrication and Results 43
3.4.3 Conclusion 47
Chapter 4 UV Sensitive Nano-structured Photodetectors 49
4.1 Introduction 49
4.2 LSPR enhanced MSM UV photodetectors 50
4.2.1 Introduction 50
4.2.2 Fabrication and Results 51
4.2.3 Conclusion 54
4.3 Sub-wavelength UV photodetector with integration of a nanoantenna 56
4.3.1 Introduction 56
4.3.2 Fabrication of the Plasmonic Photodetectors 57
4.3.3 Characterization of Nano-Photodetectors 60

4.3.4 FDTD Simulations ... 62

4.3.5 Conclusion ... 64

Chapter 5 Current Transport Mechanism Investigations of AlGaN Based Heterostructures ... 66

5.1 Current transport mechanisms and trap state investigations in (Ni/Au)-AlN/GaN Schottky barrier diodes ... 66

5.1.1 Introduction ... 67

5.1.2 Fabrication and Results ... 68

5.1.3 Conclusions ... 77

5.2 Electrical characterization of MS and MIS structures on AlGaN/AlN/GaN heterostructures ... 78

5.2.1 Introduction ... 78

5.2.2 Fabrication an Results ... 80

5.2.3 Conclusions ... 93

5.3 Leakage current investigation of Ni/Au Schottky contacts on GaN based heterostructures ... 94

5.3.1 Introduction ... 94

5.3.2 Fabrication and Results ... 95

5.3.3 Conclusion ... 98

Chapter 6 Conclusion ... 100

Bibliography ... 103

Appendix ... 116

A. Microfabrication techniques used in this study ... 116

A1. Sample Preparation ... 116

A2. Photolithography ... 117

A3. Etching 118

A4. Metallization 118

A5. Dielectric Coating 118

B. Nanofabrication techniques used in this study 119

B1. E-beam lithography 119

C. Publication list in SSI journals 119

List of Figures

Figure 2.1: Energy bands of wurtzite GaN along symmetry lines of the Brillouin zone. (adopted form[73]) 7

Figure 2.2: Absorption coefficient of $Al_xGa_{1-x}N$ epitaxial films grown on sapphire. (adopted from [76]).. 9

Figure 2.3: Band diagram of a metal-semiconductor-metal photodetector........ 10

Figure 2.4: Dielectric permittivity functions of metals 14

Figure 2.5: Dispersion relation of the SPPs on Al/Air interface. 16

Figure 2.6: Extinction spectra of Al nano-spheres in air. 19

Figure 3.1: Conceptual drawing of the dual color MSM photodetector cross-section. 22

Figure 3.2: Spectral transmission measurements: 25

Figure 3.3:IV characterization of the dual color photodetectors 28

Figure 3.4: Spectral responsivity measurements of the dual-color photodetectors. 29

Figure 3.5: Schematic diagram of the spectral photoconductivity setup 31

Figure 3.6: Schematic illustration of how a four-band photodetector works. 33

Figure 3.7: Fabrication of the four-band photodetectors. 34

Figure 3.8: Spectral transmission measurements of the wafer 1. 34

Figure 3.9: Normalized Quantum efficiency of the photodetector 36

Figure 3.10: IV Measurements of the four band photodetector 38

Figure 3.11: Comparison of the spectral response and the transmission measurements. 40

Figure 3.12: IV measurements of the fabricated photodetectors on sample 2. The numbers denote the quadrants from top to bottom. 41

Figure 3.13: Spectral transmission measurements of the recess etched 8 layered sample. 44

Figure 3.14: Spectral normalized quantum efficiency measurements of the four-color sample with extra filter layers. 46

Figure 3.15: Spectral responsivity measurements of the four-color photodetector with extra filter layers in log scale. 46

Figure 3.16: Leakage current characteristics of the four-color photodetector with filter layers. 47

Figure 4.1: Conceptual drawing of an LSPR enhanced MSM photodetector. (viewed from the top) 51

Figure 4.2: A photograph of the micro-transmission setup. 52

Figure 4.3: Fabricated Al nano-particles: 53

Figure 4.4: Spectral quantum efficiency measurement of LSPR enhanced photodetector along with the control sample. 55

Figure 4.5: Enhancement of the quantum efficiency with Al nano-particles. 55

Figure 4.6: Conceptual drawing of the nano-structured MSM photodetector ... 59

Figure 4.7: Characterization and the optimization of the plasmonic gratings. .. 60

Figure 4.8: The fabrication and the measurements of the subwavelengt photodetectors. 62

Figure 4.9: Numerical simulations of the designed grating structures. 64

Figure 5.1: The J–V characteristics of (Ni/Au)–AlN/GaN SBDs. 70

Figure 5.2: The fitting of the tunneling current expression. 71

Figure 5.3: The temperature dependences of the tunneling saturation current density (J_{s_tunnel}) and the characteristic energy of tunneling (E_{00}) for (Ni/Au)-AlN/GaN SBDs. 72

Figure 5.4: (a) Typical measured capacitance and (b) conductance data as a function of voltage for (Ni/Au)–AlN/GaN SBDs measured at 0.7, 1, 2, and 3 kHz. 73

Figure 5.5: Equivalent circuit model of (Ni/Au)–AlN/GaN SBDs used to extract trap parameters from the experimental measurements. 74

Figure 5.6: Parallel conductance as a function of frequency for (Ni/Au)–AlN/GaN SBDs at different bias voltage values. 75

Figure 5.7: Experimentally derived density (D_t) and time constants (τ_t) of the trap statesas a function of energy separation from the conduction-band edge (E_c - E_t). for (Ni/Au)–AlN/GaN SBDs. 76

Figure 5.8: AFM surface topography images of the SBD HEMTs 83

Figure 5.9: Forward and reverse bias semi-logarithmic I-V characteristics of SBD HEMT and MIS HEMTs. 83

Figure 5.10: The I-V analysis of the SBDs. 87

Figure 5.11: Density of interface states N_{ss} as a function of E_c-E_{ss} 89

Figure 5.12: The measured (a) C–V and (b) G/ω–V characteristics of SBD HEMTs and MIS HEMTs measured at 1 MHz 92

Figure 5.13: Density of interface states N_{ss} as a function of E_c–E_{ss} 93

Figure 5.14: Schematic presentation of the fabricated AlInN device used for the leakage current investigation. 96

Figure 5.15: Temperature dependent IV characteristics of Ni/Au Schottky contacts on AlInN. 98

Figure 5.16: Measured reverse-bias current density divided by electric field vs. square root of electric field. 99

Figure 5.17: Temperature dependence of the slope and intercept functions f_1 and f_2 as a function of $1/T$. 99

List of Tables

Table 3.1: Epitaxial layer content of the dual-color photodetector wafer. 26

Table 3.2: The summary of the epitaxial structure of the sample 1 for the four color photodetector. 35

Table 3.3: The summary of the epitaxial structure of the sample 2 for the four color photodetector. 38

Table 3.4: Bias conditions and the measured peak responsivity, quantum efficiency with corresponding FWHM values of the four-color UV photodetector of sample 2... 41

Table 3.5: The summary of the epitaxial structure of the eight layer for the four color photodetector with extra filter layers. 45

Table 3.6: Bias conditions and the measured peak responsivity, quantum efficiency with corresponding FWHM values of the four-color UV photodetector with filter layers. 45

Table 5.1: Temperature dependent values of the tunneling saturation current density 70

Table 5.2: The summary of the epitaxial structure of the $Al_{0.22}Ga_{0.78}N$ wafer. . 81

Table 5.3: The passivation layer thickness dependent values of parameters determined from I-V characteristics of SBD HEMTs and MIS HEMTs. 85

Table 5.4 The summary of the epitaxial structure of the $Al_{0.83}In_{0.17}N$ wafer. 96

Chapter 1
Introduction

The interest in capturing the light dates way back into the history. The early notes mentioning of camera obscura[1] are found in ancient China by Mo-Ti[1] (470 to 390 BC). Later Greek philosopher Aristotle (384 to 322 BC) explained [2] the operation principles of the camera. After the photochemicals such as silver nitrate and silver chlorite had been discovered, around 13th to 18th centuries, Niepce accomplished the fixing the image on a metal plate in 1826[3]. After the discovery of the effect of light on the conductivity of selenium and then of the photoelectric effect by Hertz[4] the photomultiplier tubes (PMT) were invented in 1934[5]. The main kicker in those days was the urgent need for a television camera. On the other hand, solid state photodetectors were investigated intensively after the semiconductors emerged around mid-nineteens. Today, we have many types of photodetectors based on semiconductors such as photodiodes from UV to terahertz regimes, charged coupled devices and CMOS sensors.

The earliest reference to the ultraviolet (UV) radiation was in the beginning of 19th century by Thomas Young's experiments in which he showed the wave nature of this invisible radiation. Typically wavelengths of 100 to 400 nm are considered as UV. It is a highly ionizing radiation with its energy higher than 3.1 eV. The spectrum further divided in to three sub-regions although it covers relatively small portion of the whole electromagnetic spectrum. This is because even a small change in the energy of the UV radiation may result in diverse effects on biological or chemical substances. Usually, the region from 400 to 320 is referred as UVA, 280 to 320 nm is referred as UVB and 100 to 280 nm is referred as UVC.[6] Wavelengths below 280 nm is often regarded as

[1] Camera obscura is the first camera which uses a pinhole to project an image on a screen in a dark environment.

the solar blind region since the stratospheric ozone layer absorbs almost all of the radiation in this region. Natural UV sources are very hot objects like the sun. The 9% of the solar radiation from the sun falls in to the UV spectrum [7]. Each subdivision has different effects on earth. For instance, UVA radiation stimulates the photosynthesis, and has some role in the synthesis of some vitamins. However prolonged exposures may lead to sunburn and premature aging. UVB is very detrimental for living species. It causes skin cancer, acute sunburns and cataracts. However, it activates the vitamin D. UVC is the most dangerous of all three. It can ionize the DNA thereby cause severe mutations. Nevertheless all of the radiation from the sun in this range is absorbed by ozone layer.[7]. Therefore it is crucial to have photosensitive receptors working in different portions of the UV radiation.

UV monitoring has many potential civil and military applications. For instance in situ temperature monitoring in nuclear power plants and internal combustion engines, telecommunication (inter-satellite communication in particular), secure non-line of sight communication, ozone layer monitoring, bio-chemical agent detection, instrument calibration for UV lithography, missile plume detection etc.[8, 9]

One must use wide band gap materials so as to detect UV radiation. Optoelectronics based on widely used Si and GaAs can operate in the UV region. However their absorption is very limited. They cannot withhold the severe conditions such as high temperature and high levels of radiation as nearby the most of the UV sources [8]. In addition they are intrinsically responsive to the visible and near infrared (IR) radiation. Therefore it is better to use a material which is intrinsically immune to the visible and IR radiation.

III-V nitrides have attracted much attention in the last couple of decades. Their room temperature direct band gaps (3.4 eV GaN, 6.2 eV AlN and 1.9 eV InN) promises very wide range optoelectronic devices. AlGaN alloys, in particular, have the ability to tune the band edge from 360 to 190 nm by varying Al mole fraction. Moreover, their direct band gap allows the precise tunability

of the material with a sharp cut off. They are immune to aging due to the high energetic radiation compared to the narrow band gap materials. Their resistance to high electric field is higher due to the wide band gap which makes them further beneficial for down scaling to the sub-micron dimensions[7, 10, 11].

UV photodetectors based on $Al_xGa_{1-x}N$ have been reported after the first successful demonstration of UV photodetectors [12, 13], such as the Schottky barrier [14, 15], p – i – n [16-18], and MSM [19-27] photodetectors.

Optoelectronic devices are getting smaller for better performance in terms of sensitivity, spatial resolution and high speed operation along with the technological developments. The nano-scaled integrated circuit elements have gained much attention due to the demand from the market for flexible, faster and more responsive electronic components. The down side of this miniaturization of the individual circuit elements, however, is the reduction of the absorption cross section for photodetectors in particular. Furthermore, when the device size is shorter than the wavelength, diffraction limits the amount of detectible radiation [28-31].

An intelligently designed plasmonic antenna can overcome this problem [32]. Surface plasmons (SP) are known as coupled plasma oscillations in metal-dielectric interfaces. The effective wavelength of bound surface plasmons is significantly less than the free space wavelength of the radiation[33]. Therefore light can be localized in a more confined volume with the help of the SPs. The experiments of Ebbessen et al.[34-39] have shown that light can be focused down to nearly 10% of its free space wavelength. There are many both experimental and theoretical reports indicating the enhanced responsivity of a photodetector is due to the excitation of surface plasmons [40-46] incorporating the extraordinary light transmission phenomenon. However it is not yet clear whether this enhancement is because of the surface plasmon excitation or leaky surface waves [47].

Localized surface plasmon resonance (LSPR) is a manifestation of SPs on nano-sized metallic particles. SPs interfere constructively at a resonance

frequency depending on the size and the shape of the particle. Thus, a strong extinction is apparent in the transmission spectrum of the nano-particles [48]. This extinction causes the localization of the electric field at the resonance frequency near the vicinity of the particle. This property has led the use of metal nano-particles in many applications such as surface enhanced Raman scattering [49-52] and biosensing [52-61]. There are also reports suggesting that this localized field can as well enhance the light absorption in the vicinity of the nano-particles for thin film and organic photovoltaics [62-71].

1.1 Motivation

The demand for UV optoelectronics has been expanding each day. The developments in the sensor technologies require devices working in very diverse spectrum. Therefore improving the performance and the functionality of UV photodetectors will fulfill the needs of the industry for the innovated products. A monolithically integrated multi-color UV sensor will significantly increase the radiation sensing capability of a photodetector as well as the simplicity of usage in comparison with the separate devices.

On the other hand making sub-wavelength sized devices has many physical insights as well as potential applications. Most of the work done in solar cells and photodetectors were, at most, in the red. This is mostly due to inadequacy of the dielectric constant of the commonly used metals Au and Ag. There is a huge gap from red to UV. By fabricating a nano-patterned antenna on top of a GaN photodetector, we were able to enhance the responsivity by eight-fold. The effective size of the photodetector was less than half of the incident wavelength.

We demonstrated that if one used Al nano-particle on a UV sensitive photodetector instead of Au or Ag, a plasmonic enhancement in UV can be attained. We further proved this enhancement via numerical simulations. This demonstration proves experimentally that LSPR can be utilized from UV to IR.

In addition, we have preformed more fundamental investigations on current transport mechanisms of the Ni-AlGaN based Schottky contacts for a deeper understanding since all of our photodetectors involve Schottky contacts. The investigation revealed that tunneling current is mostly the dominant on these contacts. Therefore operating temperature is less effective on device performance as opposed to the thermionic emission.

1.2 Organization of the thesis

We give a brief theoretical background in the chapter 2. The basic semiconductor physics and the principles of the MSM photodetector are covered first. Then, an overview of surface plasmon polaritons is provided.

In the chapter 3, we present our results on multi-color sensitive UV photodetector. First we discuss the dual color sensitive device. Then we compare our results of two different 4-color devices.

The nano-structure decorated UV photodetectors are discussed in the chapter 4. The first part is dedicated to LSPR enhanced GaN photodetectors. We present the nano-antenna integrated photodetector in the second part.

The investigations on the current transport mechanism of AlGaN based Schottky contacts are given in chapter 5. Current transport mechanisms and trap state investigations in (Ni/Au)-AlN/GaN Schottky barrier diodes are discussed in the first part. Then electrical characterization of MS and MIS structures on AlGaN/AlN/GaN heterostructures is covered. In the end, leakage current investigation of Ni/Au Schottky contacts on GaN based heterostructures is presented.

We give our final remarks and possible future directions of this study in Chapter 6.

We provided detailed fabrication steps used throughout this study in the Appendix.

Chapter 2

Theoretical Background

2.1 A brief introduction to semiconductor physics

A semiconductor is defined as a chemical element or a compound that has the electrical conductivity, ζ, higher than the insulators and lower than the common metals. The most common form of the semiconductors is the crystalline solids. Electrons have only certain bands in these materials due to the symmetric arrangement of the atoms in the crystal (Figure 2.1). The void between the uppermost valance band and the lower most conduction band is called the band gap of the semiconductor. That is, the minimum energy required to excite an electron from ground state to a conduction band is equal to the band gap and is usually expressed in terms of eV.

In this chapter we will discuss the electrical and optical properties of semiconductors (mostly in the context of GaN). Thereafter, we will briefly discuss the Schottky junction.

2.1.1 Electrical properties

The electronic band structure (*E-k* relation) of a semiconductor is obtained by solving the Schrödinger equation. Bloch theorem states that if the potential, $V(\boldsymbol{r})$, is periodic with the periodicity of the lattice, the solution of the Shrödinger equation

$$\left[-\frac{\hbar}{2m}\boldsymbol{\nabla}^2 + V(\boldsymbol{r})\right]\phi(\boldsymbol{r}) = E_k\phi_k(\boldsymbol{r}) \tag{2.1}$$

are of the form

$$\phi_k(\boldsymbol{r}) = e^{i\boldsymbol{k}\cdot\boldsymbol{r}}U_n(\boldsymbol{k},\boldsymbol{r}) \tag{2.2}$$

where $U_n(\boldsymbol{k},\boldsymbol{r})$ is periodic in $\boldsymbol{r}$ with the periodicity of the direct lattice and n is the band index [72].

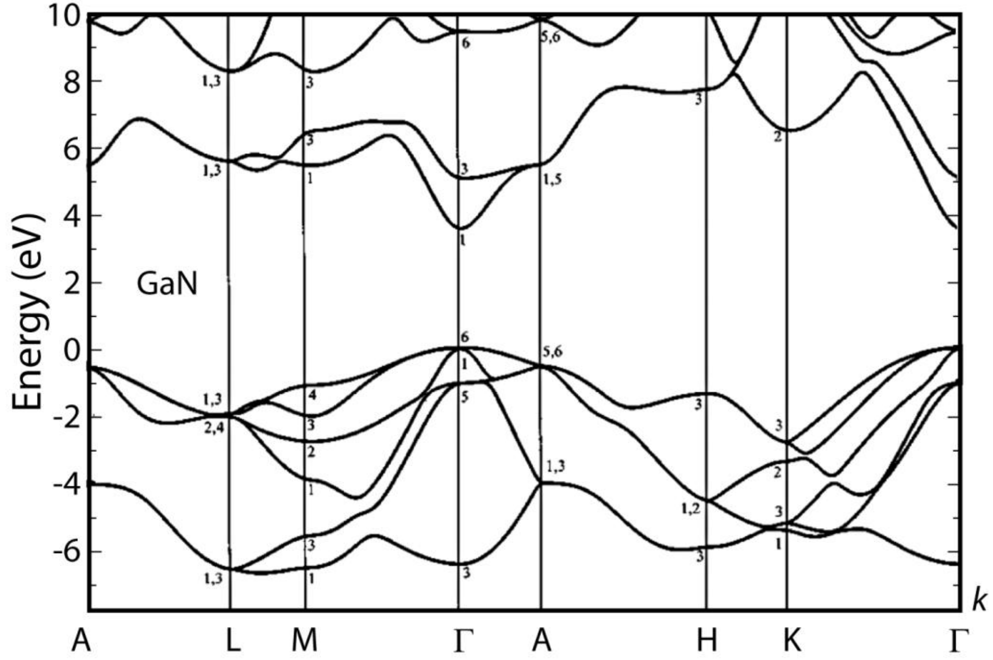

Figure 2.1: Energy bands of wurtzite GaN along symmetry lines of the Brillouin zone. (adopted form[73][1])

There are many numerical methods for calculating the band structure of the semiconductors. For instance, Yeo *et al.* calculated the band structure of GaN using empirical pseudopotential method. (Figure 2.1). They predicted the band gap of GaN as 3.42 eV.

2.1.1.1 The Band-gap of $Al_xGa_{1-x}N$

The band gap of $Al_xGa_{1-x}N$ with respect to Al concentration x is calculated with the empirical formula

$$E_g = xE_{g,AlN} + (1-x)E_{g,AlN} - bx(1-x) \tag{2.3}$$

where b ($0<b<1$) is the bowing parameter which is measured experimentally. There are a number of values for b reported in the literature [74]. In this work we used $b = 0.62$ eV.

[1] Permission obtained from AIP under the license number 2800490336991. A copy of the license agreement is attached at the end of this thesis.

2.1.2 Optical properties

The interactions between photons and the electrons in a semiconductor form the basics of the technologies such as telecommunication, solid state lighting, and sensing [75]. There are many mechanisms involved in the absorption process such as interband and intraband transitions and exitonic effects. Intraband absorption mechanism is often described with a Drude-like model where a sinusoidal electric field interacts with electrons and holes. Interband absorption which involves transitions from valance band to conduction band is the most important process, which is the basis for solid state photodetectors and emitters. Excitonic effects, in addition, explain the behavior of the absorption coefficient near the band edge.

The absorption coefficient is usually determined with various measurements rather than the numerical calculation. The most common method is spectral reflectance/transmittance measurements. Reflection and the transmission coefficients for normal incidence are given by [72]

$$T = \frac{(1-R^2)e^{-\frac{4\pi w}{\lambda}}}{1-R^2e^{-\frac{8\pi w}{\lambda}}} \tag{2.4}$$

$$R = \frac{(1-n)^2+k^2}{(1+n)^2+k^2} \tag{2.5}$$

where, w and λ are the thickness of the sample and the wavelength of the incident light, respectively. n and k are real and the imaginary parts of the index of refraction respectively. The absorption coefficient per unit length is than defined by

$$\alpha = \frac{4\pi k}{\lambda} \tag{2.6}$$

The absorption coefficient can be determined by analyzing $T(\lambda)$ and $R(\lambda)$. Brunner *et al.* measured the absorption coefficient of AlGaN films grown on sapphire with different Al content using transmission and photothermal

deflection spectroscopy [76]. We used these values as a reference for our AlGaN films in this thesis.

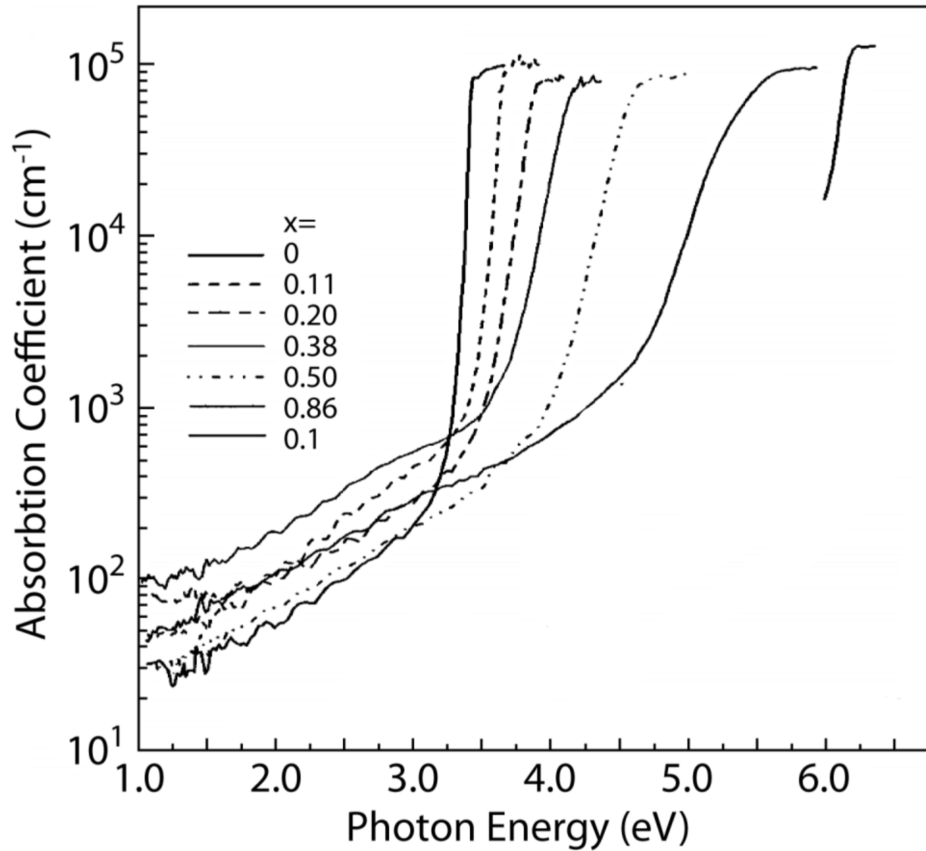

Figure 2.2: Absorption coefficient of $Al_xGa_{1-x}N$ epitaxial films grown on sapphire. (adopted from [76][1])

2.1.3 The Schottky Junction

Schottky junction (also known as metal-semiconductor junction) is made up of a metal and a semiconductor material. The name is given after *W. Schottky* who explained the rectifying behavior of this type of contact in 1930.

[1] Permission obtained from AIP under the license number 2800490798464. A copy of the license agreement is attached at the end of this thesis.

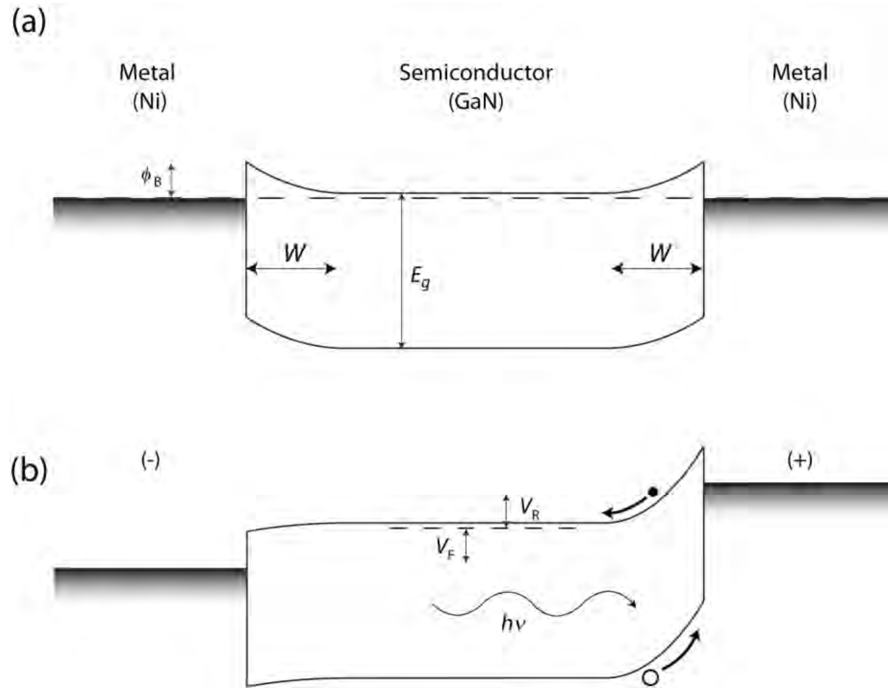

Figure 2.3: Band diagram of a metal-semiconductor-metal photodetector.(a) at zero bias and (b) at a bias of V=V_F=V_R. Here the Fermi level, shown as dashed line, illustrated close to the conduction band because our GaN substrate is intrinsically n-type.

When a metal and a semiconductor are in contact, Fermi levels coincide in thermal equilibrium (See Figure 2.3a).This causes a built in potential, ϕ_B, between the contacts. This barrier is expressed as

$$e\phi_B = e(\phi_m - \chi) \quad (2.7)$$

where ϕ_m, and χ are the work function of the metal and the electron affinity of the semiconductor, respectively and e is the elementary charge. Under the abrupt junction approximation the depletion width W is given as,

$$W=\sqrt{\frac{2\epsilon}{eN_D}\left(\phi_B - V - \frac{kT}{e}\right)} \quad (2.8)$$

where V is the applied bias voltage. There are mainly four current transport mechanisms in Schottky junctions. Such as thermionic emission – transport of electrons over the barrier (common for moderately doped semiconductors), quantum mechanical tunneling – important for heavily doped semiconductors,

recombination in space charge region and recombination in neutral region under forward bias.

The thermionic emission current density can be expressed as

$$J = J_S\left(\exp\left(\frac{eV}{kT}\right) - 1\right) \quad (2.9)$$

$$J_s = A^{**}T^2 \exp\left(-\frac{e\phi_B}{kT}\right) \quad (2.10)$$

where A^{**} is the effective Richardson constant and J_S, is the saturation current density.

When the tunneling current become the dominant mechanism in the current transport, the current density may be expressed as

$$J_t = J_{t_S} \exp\left(-\frac{e\phi_B}{E_{00}}\right) \quad (2.11)$$

where E_{00} is the characteristic tunneling energy that is related to the tunnel effect transmission probability and J_{tS} is the tunnel saturation current density.

For detailed derivation of the equations (2.7) through (2.11) please refer to the reference [72].

2.2 MSM photodetectors

Metal-semiconductor-metal (MSM) photodetectors are very easy to realize especially in materials like AlGaN/GaN. Due to growth complexities it is very difficult to grow complex epitaxial structures. In contrary, MSM devices just require a single epitaxial layer. Moreover the fabrication of these kinds of devices is straightforward. They are compatible with integrated circuit processing and suitable for high speed applications. Despite of these nice properties, there is problem due to the basic properties of metals. Metals are very good reflectors of the electromagnetic radiation. In addition skin depth values for metals are very small (~15-20 nm). Therefore in MSM structures only the half of the light can reach through the semiconductor. There are two possible

solutions to overcome this problem. First one is to make the electrodes as thin as possible so that they can transmit as much light as possible. The other method is back illumination of the device. But in this case your substrate and underlying layers should also be transparent to the incident radiation.

A typical MSM photodetector is consists of two back-to-back Schottky diodes (Figure 2.3). When a bias, V, is applied one of the diodes become forward and the other becomes reverse bias. There occurs an overall electric field between the contacts. The photo-generated carriers have to drift through the separation distance between the contacts. Therefore the speed of an MSM photodetector is often limited by this transit time.

2.2.1 Characterization of the photodetectors

The typical photodetector characterization methods include current-voltage (IV), spectral quantum efficiency and responsivity, noise and the temporal response. In this thesis we used IV and spectral quantum efficiency and responsivity measurements for the characterization of our photodetectors.

IV behavior of our MSM photodetectors is similar to the reversed bias Schottky junction. The details are represented in section 2.1.3.

Quantum efficiency of a photodetector is defined as the probability of generating an electron-hole pair which will contribute to the photocurrent by a single photon. It is a wavelength dependent quantity and is expressed conventionally as

$$\eta(\lambda) = (1 - R)\left(1 - e^{-\alpha(\lambda)d}\right) \qquad (2.12)$$

where R is the reflectivity of the top surface, $\alpha(\lambda)$ is the absorption coefficient and d is the absorptive layer thickness. Efficiency is increasing with the increasing absorption layer thickness. But thick layers cause longer carrier transit times. Therefore it makes the detector slower. This phenomenon is called the efficiency-bandwidth trade off.

Responsivity is another figure of merit to characterize a photodetector. It is defined as the produces outcome (current or voltage) per incident optical power. Therefore it has the units usually A/W or V/W. The responsivity is related to the quantum efficiency as

$$R(\lambda) = \frac{I_{ph}}{P} = \frac{\eta e}{h\nu} = \eta \frac{\lambda}{1240} \tag{2.13}$$

where λ is expresses in *nm*.

2.3 Fundamentals of surface plasmon polaritons

In this chapter we will briefly discuss the physical mechanisms behind the surface plasmons polaritons.

2.3.1 Surface plasmon polaritons

An interesting manifestation of solution to Maxwell's equation on metal-dielectric interfaces is that there exist non-radiative surface bound electromagnetic waves with a broad spectrum of eigenfrequencies, ω from zero to $\omega_P/\sqrt{2}$ depending on the wavevector $\boldsymbol{k}$, where ω_P is the bulk plasma frequency. Dielectric permittivity plays an important role on how does these surface bound waves behave. Drude-Lorentz model treats electrons simply as a free cloud on a positive immobile background. Electrons are displaced by an external electric field which has a frequency (~10^{15} Hz) much lower than their relaxation time (~10^{-18} s). This motion is modeled with a Lorentz oscillator with a damping factor, Γ, and a characteristic oscillation frequency, ω_0, which defines the restoring force exerted on electrons by the nuclei. Drude simply states that electrons in metals are free to move therefore one does not need a restoring force for metals. The resulting dielectric function in this model is

$$\varepsilon = \varepsilon_1 + i \cdot \varepsilon_2 \tag{2.14}$$

$$\varepsilon_1 = 1 - \frac{\omega_P^2}{\omega^2 + \Gamma^2} \tag{2.15}$$

$$\varepsilon_2 = \frac{\omega_P^2 \cdot \Gamma}{\omega(\omega^2 + \Gamma^2)} \tag{2.16}$$

A more rigorous derivation is given in reference [77]. This model explains some metals well such as aluminum and zinc (Figure 2.4a) where as does not for especially some transition metals like silver and gold. (Figure 2.4b) The main reason behind is the interband transitions from the valance orbitals which are just below the Fermi level. Excitation with visible frequencies can cause these transitions. Therefore the upper bound frequency for the surface plasmon polaritons shifts towards red.

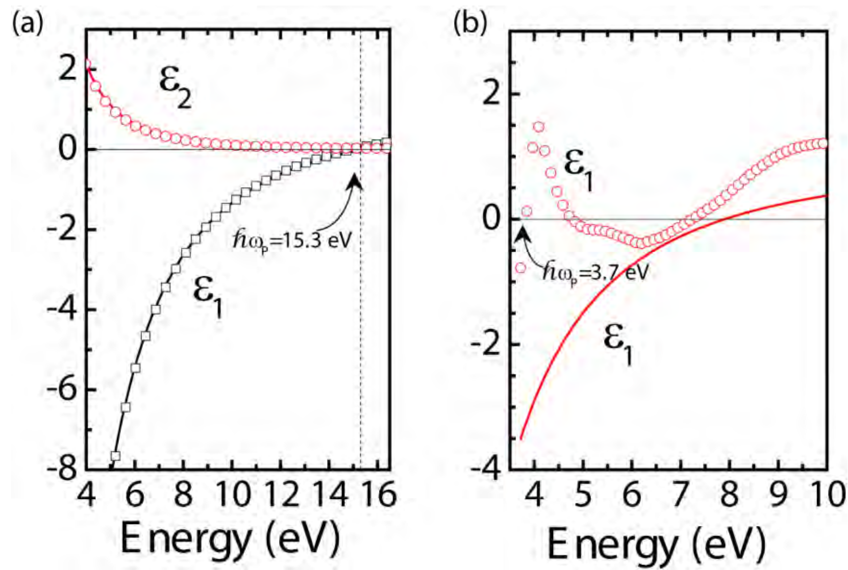

Figure 2.4: Dielectric permittivity functions of metals (a) aluminum and (b) silver. The dots are experimental data and the solid lines are calculated using Drude-Lorentz model.

Surface plasmon polaritons are surface bound electromagnetic waves produced by coherent fluctuations of surface charges by the presence of photons [33]. Electric field lines originated at positive charges ends at the negative ones. The parallel components of the electric, $E_{//}$, and the magnetic $H_{//}$ fields are continuous. Moreover we can assume that the surface charge density at the boundary, $\rho=0$, since the relaxation time of the electrons is very short compared to the frequency of the electromagnetic field. Therefore we have the continuity of the displacement field $D_{\perp}$

$$\Delta D_{\perp} = \varepsilon \Delta E_{\perp} = 0 \tag{2.17}$$

Since the electric field lines are in opposite direction across the boundary, one should have $\varepsilon<0$ for one of the parts. Metals and highly doped semiconductors satisfy this condition when $\omega<\omega_P$.

The dispersion relation of the SPPs can be derived using Maxwell's equations and appropriate boundary conditions. The well known dispersion relation can be calculated by incorporating the continuity of the tangential components of *E* and *H* fields and the perpendicular components of *D* and *B* fields as

$$k_{SPP} = k_0\sqrt{\frac{\varepsilon_m\varepsilon_d}{\varepsilon_m+\varepsilon_d}} \tag{2.18}$$

where k_{SPP} is the SPP wavevector and $k_0=\omega/c$ is the free space wavevector of the incident photon. A more detailed derivation is presented in [78]. Figure 2.5a shows the calculated dispersion relation on Al/Air interface. There is a bound SPP mode up to $\omega<\omega_R$ (ω_R=10.8 eV as predicted by Drude-Lorentz model). The radiating bulk plasmon modes in the transparency region where $\omega>\omega_R$ can be explained using free electron model which are beyond the scope of this thesis. The free electron model depicts a natural band gap for $\omega_R<\omega<\omega_P$. However the real metals have the damping factor which sets a maximum for SPP wavevector giving rise to a *quasibound* leaky mode [78].

If one assumes $\varepsilon_2<|\varepsilon_1|$ for the real and imaginary parts of the metal dielectric function ε_m, the real and the imaginary parts of the $k_{SPP}=k'_{SPP} + i\,k''_{SPP}$ can be written as

$$k'_{SPP} = \frac{\omega}{c}\sqrt{\frac{\varepsilon_1}{\varepsilon_1+1}} \tag{2.19}$$

$$k''_{SPP} = \frac{\omega}{c}\sqrt[\frac{3}{2}]{\frac{\varepsilon_1}{\varepsilon_1+1}}\frac{\varepsilon_2}{2\varepsilon_1^2} \tag{2.20}$$

Given that the dielectric constant of the air is 1. Therefore for an air/metal interface the conditions $|\varepsilon_1|>1$ and $\varepsilon_1<0$ should be met in order to have k'_{SPP} real.

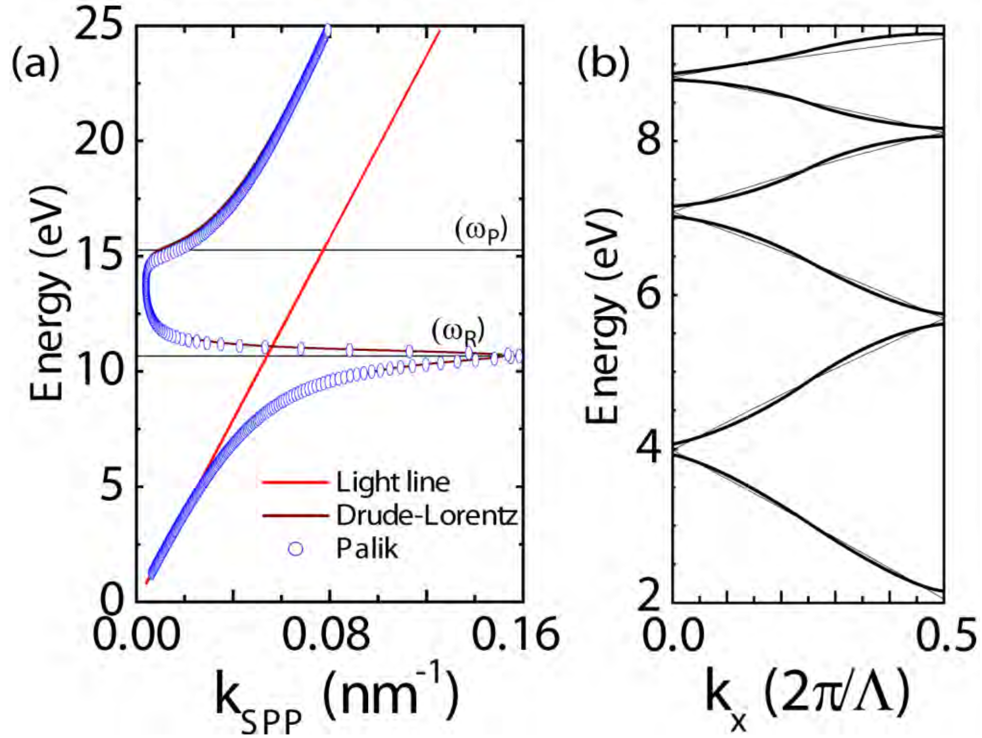

Figure 2.5: Dispersion relation of the SPPs on Al/Air interface. (a) on a smooth surface. (b) on a grating with 300 nm period.

The intensity of the SPP as it propagates along the surface decreased as $exp(-x \cdot k''_{SPP})$, x being the propagation direction. The length along which the intensity drops by $1/e$ is given as [33]

$$L_i = \frac{1}{2k''_{SPP}} \tag{2.21}$$

One other consequence followed by the SPP dispersion relation is that, the SPP line always lies below the light line. That is its momentum is always grater then the light at the same frequency. Therefore the missing momentum must be supplied in order to excite SPPs. Maier reported five mechanisms to excite surface plasmons [78]. They are charged particle impact, prism coupling, grating coupling, the near field excitation and excitation by highly focused optical beam. In this thesis we only used grating coupling. Therefore we will briefly describe the mechanism.

When a grating is fabricated on a flat metal/dielectric interface, the SPP dispersion relation (Equation (2.18)) modifies as follows. The SPP dispersion given in figure 2.5a shifts in reciprocal space by $m2\pi/\Lambda$, where Λ is the period of the grating, and m is an integer. The dispersion curves are than projected to the first Brillion zone. At the crossing sites of the curves, waves interfere and a small band gap opens. The periodicity, depth and the pitch of the grating effects this band gap formation [79]. The modified dispersion relation can be written as

$$k_{SPP} = k_0 sin\alpha \pm l\frac{2\pi}{\Lambda} = k_0\sqrt{\frac{\varepsilon_m \varepsilon_d}{\varepsilon_m + \varepsilon_d}} \qquad l = 1,2, \ldots (2.22)$$

where α is the angle of incidence. The first three SPP modes on Al/air interface with a grating with 300 nm period is illustrated in figure 2.5. Here the band gap openings are sketched. The thin lines under are the actual calculated SPP modes using the equation (2.22). As a consequence of the periodicity in the grating, we now have modes over $k_x=0$. Therefore SPP modes can be excited at normal incidence.

2.3.2 Localized surface plasmon resonance

The light is scattered by the small metal particles because of the resonant plasma oscillations of the conduction electrons. In the previous chapter we have investigated the surface plasmons which propagate along the metal dielectric surface. In a small particle, on the other hand, there is not enough space for surface plasmons to propagate. Instead there occurs a resonant mode depending on the size and shape of the particle. This resonance is called localized surface plasmon resonance (LSPR). Electric field becomes highly localized in the vicinity of the particle at the resonance frequency. This localization effect can be used in various practical applications as stated in the introduction.

The quantitative analysis of the behavior of metallic nano-particles requires rigorous calculations. Nevertheless, these formulations are limited to basic geometries like spheres. Kuwata *et al.* developed an analytical model for ellipsoid particles [80] however they establish their model based on

experimental data. Because of analytical limitations, finite difference time domain (FDTD) simulations are often used to predict resonance of a specific nano-particle.

The most basic formulation can be based on assuming the relaxation time within the particle is much shorter than the period of the oscillations. Then one may assume the particle is a spherical object with radius $r \ll \lambda$, in a uniform electric field. Then, using the appropriate boundary conditions at infinity and the surface of the sphere the polarizability, α, can be calculated as [78]

$$\alpha = 4\pi r^3 \frac{\varepsilon - \varepsilon_m}{\varepsilon + 2\varepsilon_m} \tag{2.23}$$

where ε and ε_m are the dielectric constants of metal and the surrounding medium, respectively. The most important consequence of this model is that there exist a resonance at $re(\varepsilon)=-2\varepsilon_m$ which corresponds to $\omega_P/\sqrt{3}$ for Drude like metals. However it does not explain the size dependency of the resonance. Note that this model is only valid for vanishingly small particles.

Mie has established a more general theory to explain the scattering from the gold nano-particles which later called after him as *Mie Theory*. The polarizability in this theory for larger particles with sizes comparable to the wavelength of excitation can be written as [80, 81]

$$\alpha = \frac{1 - \frac{1}{10}(\varepsilon + \varepsilon_m)x^2 + o(x^4)}{\frac{1}{3} + \frac{\varepsilon_m}{\varepsilon - \varepsilon_m} - \frac{1}{30}(\varepsilon + 10\varepsilon_m)x^2 - i\frac{4}{3}\pi^2 \varepsilon_m^{3/2} \frac{V}{\lambda} + O(x^4)} V \tag{2.24}$$

Where V is the volume of the nanoparticle and $x = 2\pi r/\lambda$, the size parameter. The quadratic term in the numerator explains the retardation effect in excitation of the whole volume of the particle which shifts the resonance. The quadratic term in the denominator shifts the resonance further due to the retardation of the depolarization field. For Drude-like metals this shift in resonance is towards red as particle size increases. The extinction spectra of Al nano-spheres in air as an example is calculated with this model and plotted in figure 2.6.

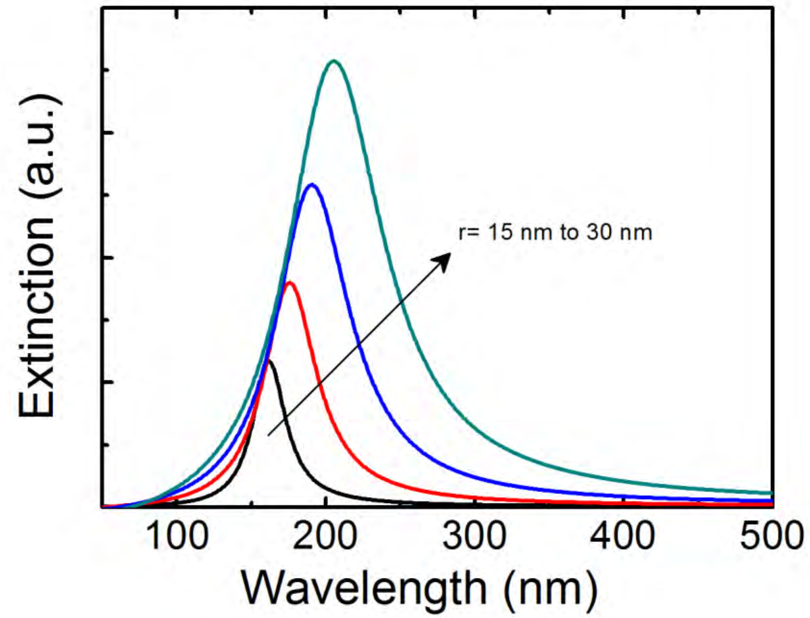

Figure 2.6: Extinction spectra of Al nano-spheres in air. Curves are calculated using equation (2.24).

Chapter 3
Multi-color Sensitive Photodetectors

3.1 Introduction

Light detection is crucial for many technological applications for instance telecommunication, sensing, imaging, temperature monitoring, range measuring, remote control devices and environmental monitoring. A photodetector must somehow convert the electromagnetic energy of the light to a measurable entity. There are mainly three different techniques used for light detection such as photon detectors, thermal detectors and coherent receivers. They all have their own advantage in certain portions of electromagnetic spectrum. In this chapter we worked on UV MSM photodiodes which fall in to the photon detectors category.

The detection of the highly energetic UV light requires wide band gap semiconductors such as AlN, GaN, BN, diamond and SiC [8]. AlN/AlGaN/GaN based UV photodetectors have been widely investigated through past couple of decades [7, 9, 82-87]. Previously, we focused on this particular area, as well. We published a number of articles during that research on various types of photodetectors based on AlGaN material system [15, 19, 20, 23, 88-99]. In this thesis we worked on multi-color sensitive UV photodetectors for further improvement of our previous work.

Detection light in multi-bands has number of advantages over single band. Ability to analyze narrow multi-bands increases the spectral resolution and in some cases spatial resolution as well. Thus the probability of false alarms can be decreased. Current multi band detectors utilize IR/IR [100], UV/IR or UV/visible/IR bands. Multi UV band detectors will further improve the photodetector performance in UV applications such as high temperature sensing, missile plume detection or non-line of sight communication etc.

One method to achieve narrow band detection is the utilization resonant cavity enhancement. Such devices were realized in wavelengths other than UV [101, 102]. The other technique is the usage of highly absorptive filters between the active layers which is rather suitable for AlGaN system. A similar device was reported on a Si photodiode for monitoring laser diodes [103].

We proposed and fabricated multi band photodetectors with and without intermediate filter layers. The capability of detection of different colors on a single chip is the main advantage of these devices. The device can be mounted on a single platform and performs multiple band detection which decreases the size and the cost.

In this chapter we present our work on dual-color and four-color sensing UV photodetectors.

3.2 Dual-Color sensing UV photodetectors

This section was published as "Dual-color ultraviolet metal-semiconductor-metal AlGaN photodetectors" Mutlu Gokkavas, Serkan Bütün, HongBo Yu, Turgut Tut, Bayram Bütün and Ekmel Özbay, Appl. Phys. Lett., 89, 143503 (2006). Reproduced (or 'Reproduced in part') with permission from American Institute of Physics. © 2006 American Institute of Physics.

In this chapter we presented back-illuminated ultraviolet metal-semiconductor-metal photodetectors with two separate spectral responsivity bands on a single $Al_xGa_{1-x}N$ heterostructure. This was achieved through epitaxial growth of three AlGaN layers with decreasing Al content. Two of the layers (bottom and top) were the active layers for each band and the one in the middle acts as epitaxial filter. We reached to the bottom layer by recess etching of the top and the filter layer. The top detector has responsivity of 0.12 A/W at 310 nm with 10 V bias and 11 nm full width at half maximum (FWHM), whereas the bottom detector has peak responsivity of 0.1 A/W at 254 nm with 25 V and 22 nm FWHM. Both detectors performed well in terms of dark current with less than 10 fA leakage current.

3.2.1 Concept

Dual-band MSM photodetector structure consists of three successive layers of epitaxial materials grown on a transparent substrate. The bottom and the top layers are the active layers on which the photodetectors are made. The middle layer blocks light with wavelength below the cut-off wavelength of itself. Thus, it acts as a filter layer for wavelengths below the cut-off.

The growth of AlGaN expitaxial material requires higher temperature as the Al content increases. Therefore growth order should be higher Al content to lower which necessitates the back side illumination of the device. This requirement further simplifies fabrication as it eliminates the deposition of the semi-transparent MSM contacts.

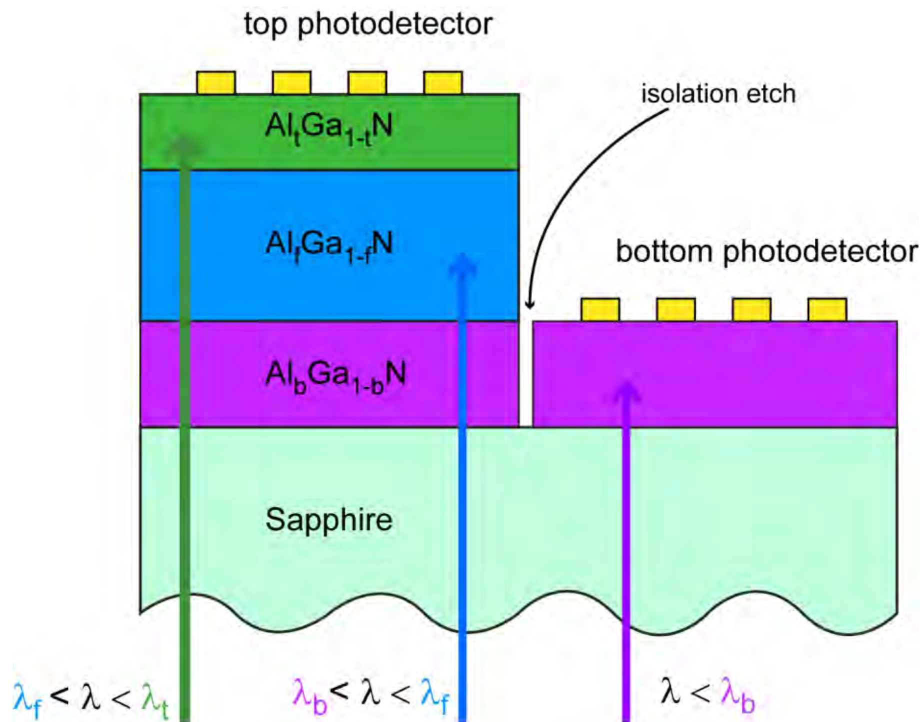

Figure 3.1: Conceptual drawing of the dual color MSM photodetector cross-section.

Figure 3.1 shows the concept of a dual-band photodetector structure. The bottom (violet), middle (blue) and top (green) layers consist of AlGaN layers

with cut-off wavelengths λ_b, λ_f and λ_t. Therefore, only light with, $\lambda > \lambda_b$ can reach to the middle layer the rest is absorbed in the bottom layer due to the high absorption coefficient. Furthermore, middle absorbs all the light with $\lambda < \lambda_f$ therefore only light with $\lambda f < \lambda < \lambda_t$ can be absorbed in the top (green) layer. In the end, blue layer acts as a filter layer to divide the spectrum in half.

3.2.2 Fabrication and Results

We used low-pressure metal organic chemical vapor deposition for the growth of the photodetector structure used in this study. Aixtron AG AIX 200/4 RF-S model reactor, which was installed in Nanotechnology Research Center in Bilkent University, was used for the growth. C-plane double side polished 2 inch diameter sapphire was chosen as substrate is used for AlGaN growth. There are other substrates such as Si and SiC which are widely investigated in AlGaN research but they are not transparent in the range we are interested.

Epitaxial growth was initialized with the typical cleaning process to remove surface contamination. The substrate was annealed at 1100 °C under H_2 with flow rate of 3500 sccm at 100 mbar for 10 min. There is a 10% lattice mismatch between the AlN and the sapphire substrate. This causes formation of dislocations and cracks if the material (AlN) is grown directly on the substrate. In order to avoid that, a thin nucleation layer is grown at low temperature with relatively poor crystal quality. The nucleation layer was grown at 550 °C and the thickness was 15 nm. The temperature of the reactor was increased to 1130 °C and the pressure was decreased to 25 mbar after the deposition of the AlN nucleation layer. A 400 nm thick $Al_{0.5}Ga_{0.5}N$ bottom detector active layer was grown at a rate of 2 µm/h. We wanted an abrupt junction between the bottom detector layer and the following 1 µm thick $Al_{0.25}Ga_{0.75}N$ filter layer. Therefore another nucleation layer under the same conditions is grown next. The growth temperature and the pressure of the filter layer were 1080 °C and 50 mbar, respectively. Finally, a 250 nm thick $Al_{0.2}Ga_{0.8}N$ top detector active layer was grown under the same conditions. The composition was changed by altering the

flow rates of the precursors. We did not employ another nucleation layer between the filter and the top detector layers because the composition was not severely different in these layers. No intentional doping was applied during the entire growth process. Trimethylaluminum, trimethylgallium, and ammonia (NH_3) were used as reaction precursors for the Al, Ga, and N, respectively. Trimethylaluminum and Trimethylgallium were carried through the bubblers with hydrogen gas.

We performed spectral transmission measurements in order to determine the actual Al content and the layer thicknesses of the photodetector structure. Our transmission setup consists of a Xe UV enhanced broad band light source, UV enhanced fiber optic cables, collimating optics mounted on a sample stage and Oceanoptics USB4000 UV enhanced spectrometer. (Figure 3.2a)

Consecutive transmission measurements were performed as we etched the surface. (Figure 3.2b) We used reactive ion etching (RIE) using CCl_2F_2 plasma with an RF power of 200 W and under 50 μbar pressure. The etch depth was monitored with a profilometer. Figure represents the transmission spectrums of samples of as grown and three subsequent etch depths of 250 nm, 1000 nm and 1250 nm. The sharp cut off at 315 nm of the as grown wafer corresponds to an Al content of 20% which will act as the active layer for the top detector. There remains a slight transmission between 301 and 315 nm which was due to the relatively thin top layer. We observe the shift of the transmission cutoff to 301 nm after the 250 nm etch. This indicates two points: one the top layer is at most 250 nm thick and the Al content of the filter layer is 27%. The transmission cutoff is further shifts to 259 nm when the total etch depth reaches to 1000 nm. We again have about 10% transmission between 259 and 301 nm due to the remaining part of the filter layer on the surface. Finally when we etch down to 1250 nm we observed a sharp cutoff at 259 nm which indicates the Al content of the bottom detector layer is 50%. We further confirm the thickness of the bottom layer by etching 400 nm more. We then have a complete transmission with no cutoff indicating we had reached the sapphire

surface. The structure of the wafer is confirmed after these measurements and is summarized in the Table 3.1.

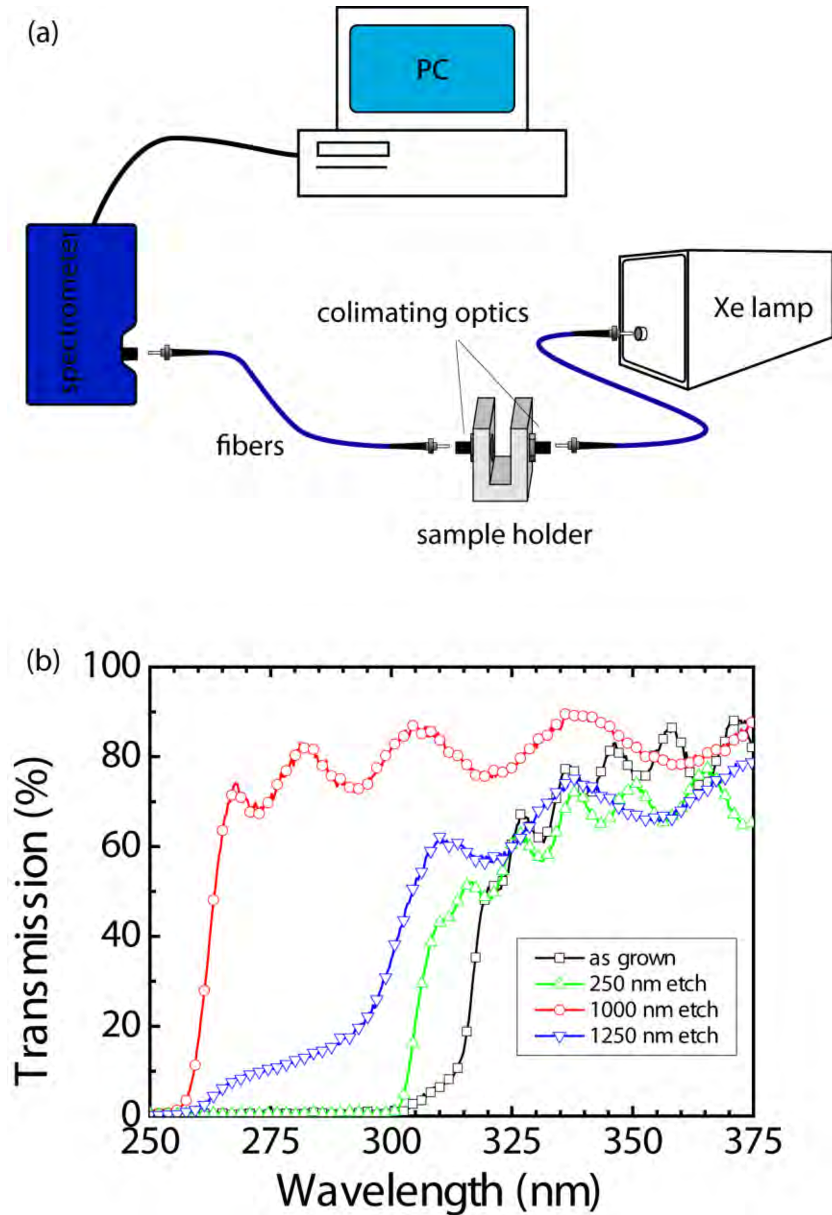

Figure 3.2: Spectral transmission measurements: (a) Schematic diagram of the measurement setup. (b) Spectral transmission measurements of the dual-color photodetector wafer as the recess etch continues.

We cut a 1 × 2 cm^2 piece from the wafer. The fabrication started with the recess etching of the top and the filter layers. Firstly, we cover half of the chip with photoresist. Then several RIE steps were performed while monitoring the transmission spectrum each time. Etching continued until the bottom detector

active layer was reached. Cleaning and photoresist coating was applied a number of times since photoresist is etched several times faster than AlGaN. Secondly, MSM contacts were fabricated in a class 100 clean room environment on both etched and unetched part of the chip using UV photolithography. Interdigitated contact distances and widths were varied between 1.5 to 5 μm. We thermally evaporated Ni/Au metal pair (100 Å / 5000 Å) as Schottky contact material. Thirdly, device mesas of 100 × 100 cm^2 and 200 × 200 cm^2 areas are defined photo-lithographically and etched down to the sapphire via RIE. Finally, the probe pads were fabricated using Ti/Au metal pair (200 Å / 5000 Å). The details of the each fabrication steps are thoroughly covered in appendix A.

Table 3.1: Epitaxial layer content of the dual-color photodetector wafer.

Layer	Thickness
$Al_{0.2}Ga_{0.8}N$	250
$Al_{0.27}Ga_{0.73}N$	1000
AlN	15
$Al_{0.5}Ga_{0.5}N$	400
AlN	15
Sapphire	substrate

Leakage current characterizations of the photodetectors were made in a class 10000 environment using low noise triaxial cables in a Fraday cage by Keitley 6517A model high resistance electrometer (Figure 3.3a). Devices under test were both 100 × 100 cm^2 in area. Contact width and spacing were both 3 μm. Figure 3.3b shows the comparison of measured dark current characteristics of the top and the bottom photodetectors. Both devices exhibited typical characteristics as expected from such wide band gap materials. Dark current at zero bias was 9 fA and 7 fA for top and the bottom photodetectors, respectively. Dark current level does not exceeded 1 pA level for both detectors until such a high bias of 180 V. It is especially better for the bottom detector (more than an order of magnitude lower) which can be attributed to the higher band gap of the bottom layer. There were no sign of breakdown up to 180 V bias. Considering

the aim of this device, having rather wide range of bias voltage is especially an advantage because it is better to operate both of the detectors at about the same responsivity value which is bias dependent. These low levels are a qualitative sign of the low background doping which arises from the dislocations. Therefore it is a clear sign of the high quality of the epitaxial layers. In addition, we may argue that the deep recess etch process did not cause any sort of significant surface damage.

We measured spectral responsivity characteristics of the dual-color photodetectors using a Stanford Research Systems SR830 Lock-in amplifier. The output of the UV enhanced Xe lamp (Spectral Products ASB-XE-175) was monochromated (Spectral Products DK240) then modulated mechanically by a chopper. It is then coupled to a multi-mode non-solarized UV enhances 100 μm diameter fiber which was used to illuminate the photodetector under test (Figure 3.5a) We customized the chuck and the probe holder of the Cascade Probe Station in order to illuminate devices from the back side. (Figure 3.5b and c) We calibrated the spectral output power illumination setup with a NIST-traced calibrated Si photodetector (Newport 818-UV-L). We used 200 × 200 μm^2 area and 3 μm contact width and spacing devices for the responsivity measurements.

Responsivity of both photodetectors increased with the applied bias which is typical for MSM devices. Measured responsivity curves in the spectral range of 200 to 500 nm are compared in Figure 3.4. The top photodetector was biased at 10 V whereas the bottom detector was biased at 25 V in order them to exhibit comparable responsivity values. The responsivity of the top photodetector peaked at 310 nm with 0.12 A/W whereas the responsivity of the bottom photodetector peaked at 254 nm with 0.10 A/W. FWHM of the responsivity values are 11 and 22 nm for top and the bottom photodetectors, respectively.

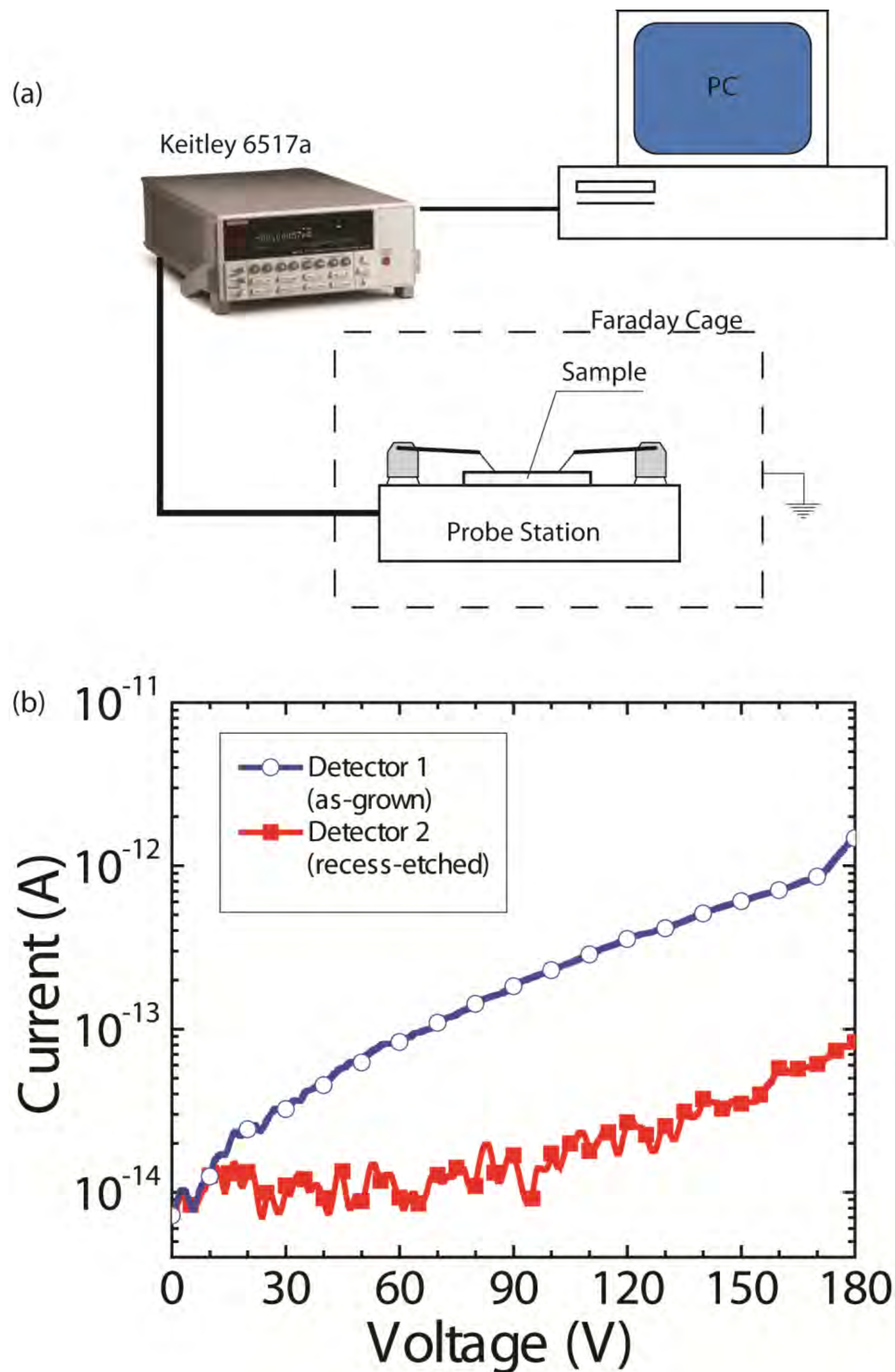

Figure 3.3:IV characterization of the dual color photodetectors (a) Schematic diagram of the leakage current characterization setup. (b) Dark current measurements of the top and bottom photodetectors.

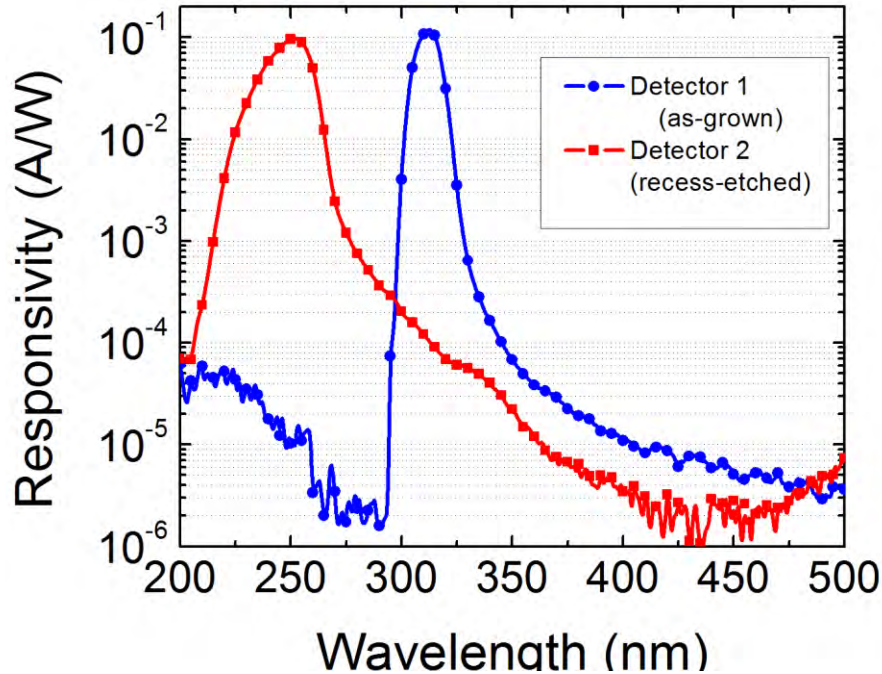

Figure 3.4: Spectral responsivity measurements of the dual-color photodetectors.

There is a quite large rejection (about four orders of magnitude) in terms of responsivity for both bands. The responsivity of the top photodetector drops very sharply below 300 nm which is due to 1 µm thick the $Al_{0.27}Ga_{0.73}N$ filter layer. There is a good agreement if we compare this to the spectral transmission measurements (Figure 3.2b) prior to the fabrication. The filter layer blocks the light with wavelength below 300 nm which explains the sharp drop in the responsivity curve of the top photodetector. The increase towards the shorter wavelengths is not the real increase in the response of the device but the decrease in the dynamic range of our measurement setup. That is, the measured photocurrent remains constant at the lowest possible measurable value whereas the optical power of the illumination decreases. Hence, the responsivity seems increasing as the wavelength decreases. On the other hand, the responsivity of the bottom photodetector drops fairly sharp above 260 nm which is due to the band gap of the active bottom layer. Slight response between 300 to 400 nm of the bottom photodetector is due to the low energy (compared to band gap) trap

states originated from the imperfections such as dislocation and impurities which are much like the phenomenon so called yellow luminescence in GaN The minor increase towards the 500 nm is because of higher order leakage of the monochromator. As a result, top photodetector rejects to bottom band more than four orders of magnitude while the bottom photodetector rejects the top band more than three orders of magnitude. In addition, both photodetectors rejects visible by more than four orders of magnitude at 500 nm.

3.2.3 Conclusion

We fabricated and characterized dual-color back illuminated UV MSM photodetectors with separate spectral bands monolithically on the same chip. This was achieved by growth of three different Al content epitaxial layers. Top and the bottom layers were used as an active absorption layer while the middle layer was used as passive absorptive filter layer. The bottom layer was reached via recess etching of the top and the middle layers. The peak response of the top photodetector was 0.12 A/W at 310 nm with 10 V bias whereas the peak response of the bottom photodetector was 0.10 A/W at 254 nm with 25 V bias. FWHM of the top and bottom photodetectors were 11 and 22 nm respectively. Top photodetector rejected the light in the bottom photodetector operation band with more than four orders of magnitude, and bottom photodetector rejected light in the top photodetector operation band with more than three orders of magnitude. Both photodetectors exhibit superior dark current characteristics with no more than 1 pA up to 180 V bias. Given the ozone layer absorption at 280 nm, we can conclude that bottom photodetector is solar blind while the top photodetector is visible blind. This property gives a unique ability to monitor UV radiation differently by day and night to the overall device.

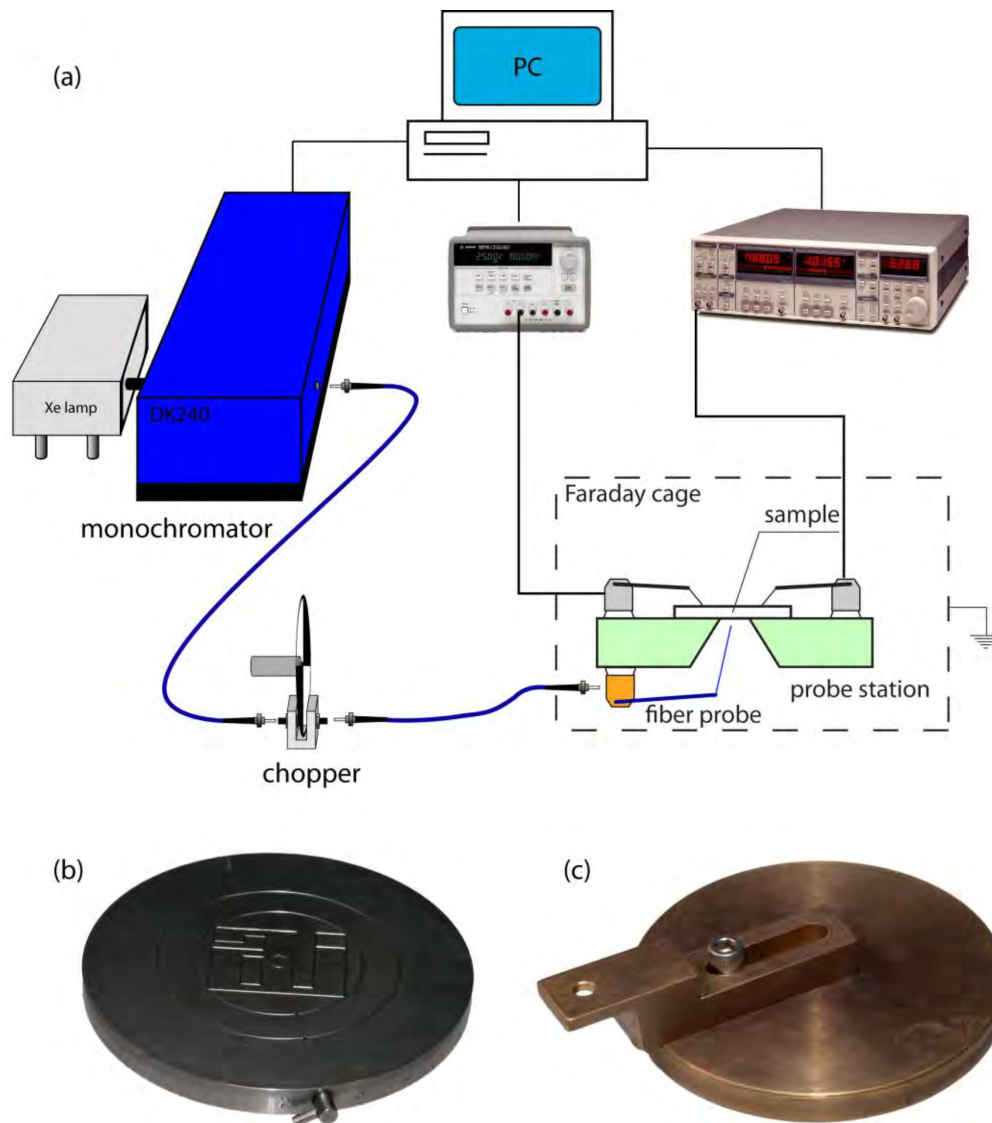

Figure 3.5: Schematic diagram of the spectral photoconductivity setup (a). The original (b) and the custom made brass (c) chucks are presented in the photographs. Sample is placed over the hole on the bracket. The fiber probe is then aligned from the bottom.

3.3 Four-Color sensing UV photodetectors

This section along with the section 3.4 was submitted as "Four-color ultraviolet metal-semiconductor-metal AlGaN photodetectors" Mutlu Gokkavas, Serkan Bütün, Wlodek Strupinski and Ekmel Özbay, Semicond. Sci. Tech. October, 2011.

Ultraviolet (UV) light sensitive devices are fabricated on AlGaN templates grown on c-plane sapphire by metal-organic chemical vapor deposition. We fabricated back illuminated metal-semiconductor-metal (MSM) photodiodes with multiple color sensitivity on single epitaxial structure. Our devices consist of several active layers which are sensitive to different portions of the UV spectrum. We incorporated the self filtering effect of the epitaxially thick (around 1 um) active layers in order to suppress the other part of the spectrum. We fabricated 4 separate MSM diodes on 4 different active layers by recess etching of the surface. The resultant device showed well separated four peaks at 267, 290, 309 and 328 nm with FWHM of 9, 22, 17 and 18 nm respectively. The leakage current of the devices were on the order of 10 pA.

3.3.1 Concept

Four-color AlGaN photodetectors consists of four active layers with different Al content. We include a fifth passive filter layer down at the bottom as well in order to make fourth band further narrower after our first attempt. A conceptual drawing of a four color sensing device is shown in Figure 3.6. Different epitaxial AlGaN layers with different Al concentrations are represented with different colors. Each epitaxial layer has a separate MSM photodetector structure fabricated on. The thicknesses of each active epitaxial layer are sufficient enough to absorb all the light below its band gap. Therefore each acts as a filter layer for the photodetector on the layer above it.

3.3.2 Fabrication and Results

The epitaxial growth of $Al_xGa_{x-1}N$ layers with different Al content on one another is the main challenge in this work. We designed our structure such that the Al concentration of the epitaxial layers is decreasing along the growth direction because it is nearly impossible to grow otherwise. Hence, the back illumination is used.

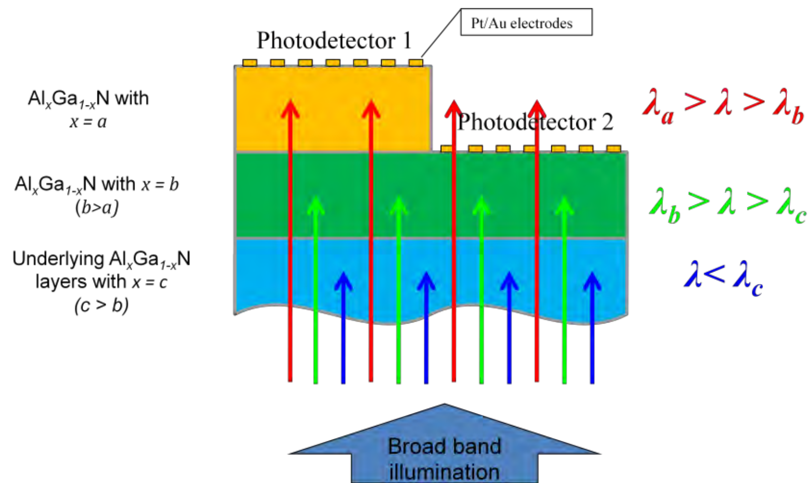

Figure 3.6: Schematic illustration of how a four-band photodetector works. Here a, b and c represents the mole fraction of the Al in the AlGaN crystal. λ_a, λ_b, and λ_c are corresponding cut-off wavelength of individual epitaxial layers. Just top two detectors are shown for the sake of simplicity.

Two samples were grown for the fabrication of the four-color UV photodetectors. First sample was consisting of four AlGaN layers with different Al content as 10%, 20%, 30% and 40% from top to bottom. Each of the AlGaN layers had the thickness of 500 nm. The AlN buffer layer was about 100 nm thick.

The growth of this sample was done in a very similar manner like the dual-color sample. (on page 23) The Al concentration was varied by changing the precursor flow rates. A 15 nm AlN nucleation layer was utilized between each of the layers.

We performed sequential etching of the wafer with Resonant Ion Etching in CCl_2F_2 environment and measure the transmission spectra in order to analyze the Al content of the layers in the same transmission setup as the dual-color photodetectors (Figure 3.2a). Spectral transmission measurements of the wafer 1 are represented on Figure 3.8. We determined Al content and thickness of each according to the transmission measurements. The results are summarized in the Table 3.2. We did not quite achieve the targeted Al contents. In addition, the transmission curve suggested that the thicknesses of the epitaxial layers are not enough to suppress all the light with energy higher than the band-gap of the

specified layer. The transmission curve of the top and one layer below (black and red curves) showed some amount of the transmission below the band edge.

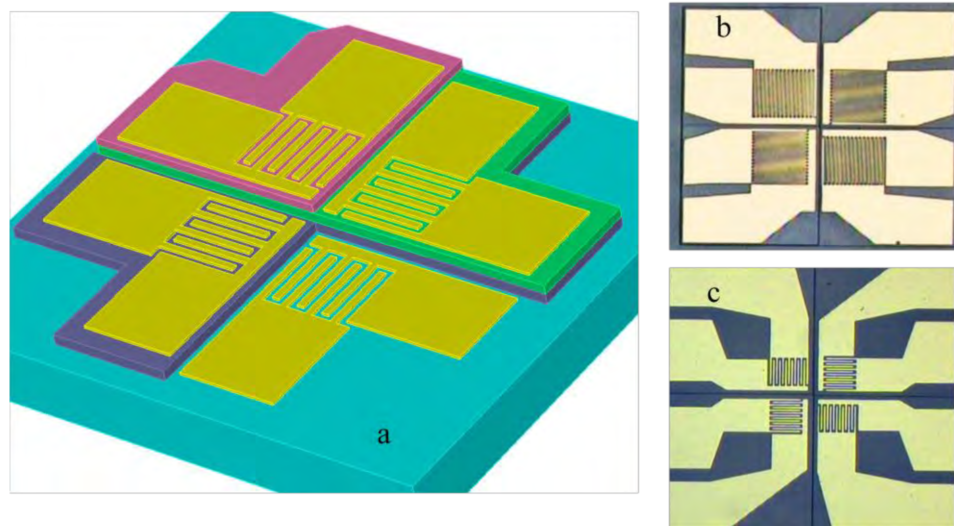

Figure 3.7: Fabrication of the four-band photodetectors. (a) Conceptual drawing of a finalized device, (b, c) optical micrographs of fabricated devices with different device areas and finger widths.

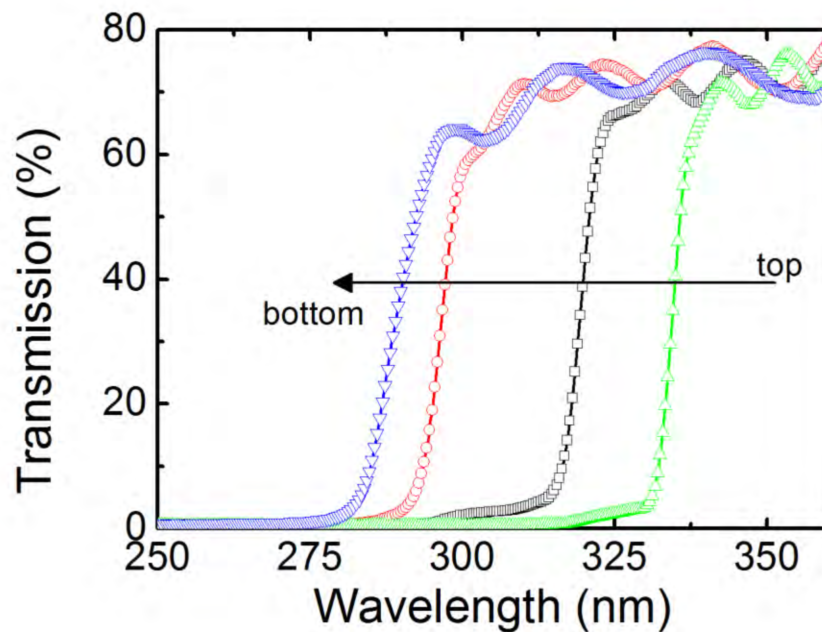

Figure 3.8: Spectral transmission measurements of the wafer 1.

These results suggested that we have to increase the layer thicknesses and a further optimization of the growth conditions was required. Nevertheless, we carried on the fabrication of the photodetectors on this sample to have an idea on the effect of Al content on the device performance.

Table 3.2: The summary of the epitaxial structure of the sample 1 for the four color photodetector.

Layer	Thickness (nm)
$Al_{0.12}Ga_{0.88}N$	500
$Al_{0.18}Ga_{0.82}N$	500
$Al_{0.29}Ga_{0.71}N$	500
$Al_{0.34}Ga_{0.66}N$	500
AlN	100
Sapphire	Substrate

We have designed a simpler photomask for the fabrication of the four-color photodetectors. The total device area is 400 × 400 μm^2. Each quadrant where an individual photodetector is fabricated has 200 × 200 μm^2 area. Fabrication starts with the recess etch of the top layers. We first covered the on quadrant of the detector area with photoresist, and then performed the etching. Next, we covered the fist and the second quadrants. This sequence continued when until we finish etching of all four quadrants. We performed a mesa isolation etch next when the recess etch finished. In the final step we fabricated interdigitated Schottky contacts with varying contact distances. The fabricated devices are shown on Figure 3.7b and c. We performed spectral quantum efficiency and current-voltage (IV) measurements on the fabricated devices.

Spectral quantum efficiency measurements measured with the photoconductivity setup (Figure 3.5a) represented on Figure 3.9. First of all, there are undesired cross-talks between the adjacent bands. The inadequate thickness of the epitaxial layers was the main reason for this problem. Because

the layers cannot absorb all of the light as transmission measurements suggested. The second problem was the unevenly distribution of the Al content throughout the layers. When we compare the response of the third and the fourth devices (green and red), the peak response is too close to each other which is consistent with the close cutoff wavelengths of the two layers. The third problem is that the second device has a very wide FWHM (27 nm). This can be attributed to the large gap in the transmission spectra of second and the third device. Final disturbing aspect of this measurement is that the response of the fourth device does not decay fast enough as the wavelength decreases. Overall the quantum efficiency curves are not as narrow and as separated as desired.

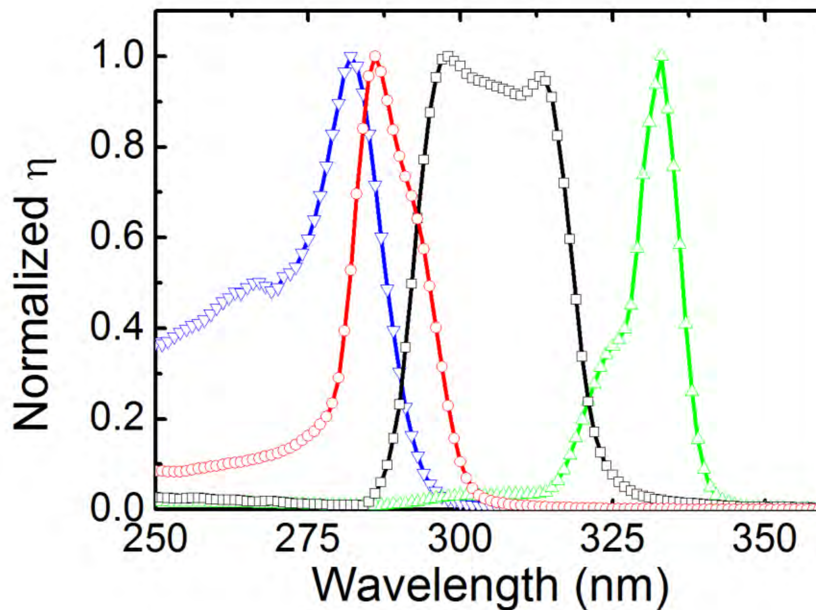

Figure 3.9: Normalized Quantum efficiency of the photodetector with 5 µm finger width and pitch. Each color represents the response from a separate quadrant of the device.

IV measurements of the fabricated photodetectors were performed on our leakage current characterization setup (Figure 3.3a) and are shown in Figure 3.10. Device exhibited typical current voltage characteristics for such a high band gap material.

We changed the design of the first structure after evaluating the results. In the second sample, we double the thickness of each AlGaN layer and we add one additional layer at the bottom so that the long shoulder in the red curve of Figure 3.8 towards the short wavelengths is suppressed. The growth of the second four-color wafer was done as described above with further optimized conditions.

We performed a compositional analysis via recess etching the surface through spectral transmission measurements, again using our spectral transmission setup (Figure 3.2a). The results are shown in figure 3.11a. These measurements indicated that we have well separated band edges with better suppression of light with higher energy then the band-gap of each layer which confirms the necessity of thicker layers. We also confirmed the high thickness of the each epitaxial layer while etching. Layer compositions are summarized in iv measurements of the fabricated photodetectors are shown in figure 3.12. devices again exhibited expected current voltage characteristics for such a high band gap material except the device 2. we believe that the structural deformities in $al_{0.14}ga_{0.86}n$ are the main reason for this relatively high dark current which is consistent with the spectral responsivity measurements. no sign of breakdown was observed up to 100 v bias.

.

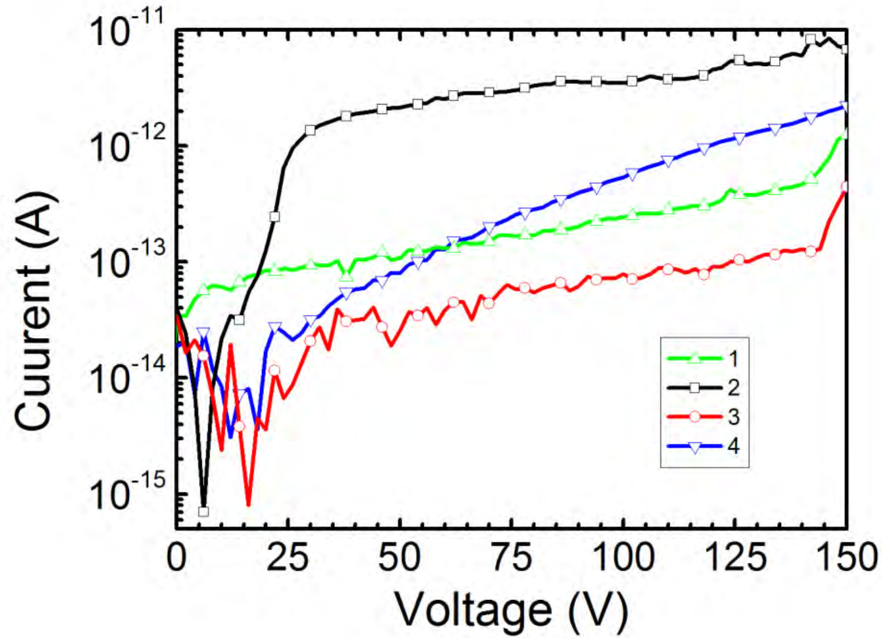

Figure 3.10: IV Measurements of the four band photodetector of each quadrant from a 5 µm finger width and pitch device in log scale. The numbers denote the quadrants from top to bottom.

The fabricated photodetectors have shown much better spectral response than the previous one. As you can see on the Figure 3.11b, we have well separated four responses with narrow bands. The only undesired situation is the slight shoulder of the top (green) device. This was the result of poor quality of the epitaxial layer underlying the top layer (red). Even at very low bias voltages like 0.1 V we have that response, because of high photoconductive gain originated to the defects in the $Al_{0.14}Ga_{0.86}N$ layer.

Table 3.3: The summary of the epitaxial structure of the sample 2 for the four color photodetector.

Layer	Thickness (nm)

$Al_{0.07}Ga_{0.93}N$	1000
$Al_{0.14}Ga_{0.86}N$	1000
$Al_{0.25}Ga_{0.75}N$	1000
$Al_{0.40}Ga_{0.60}N$	1000
$Al_{0.45}Ga_{0.50}N$[4]	1000
AlN	150
Sapphire	substrate

[4] The Al content of the fifth layer was not determined from the transmission measurements per se but from the width of the spectral quantum efficiency measurements.

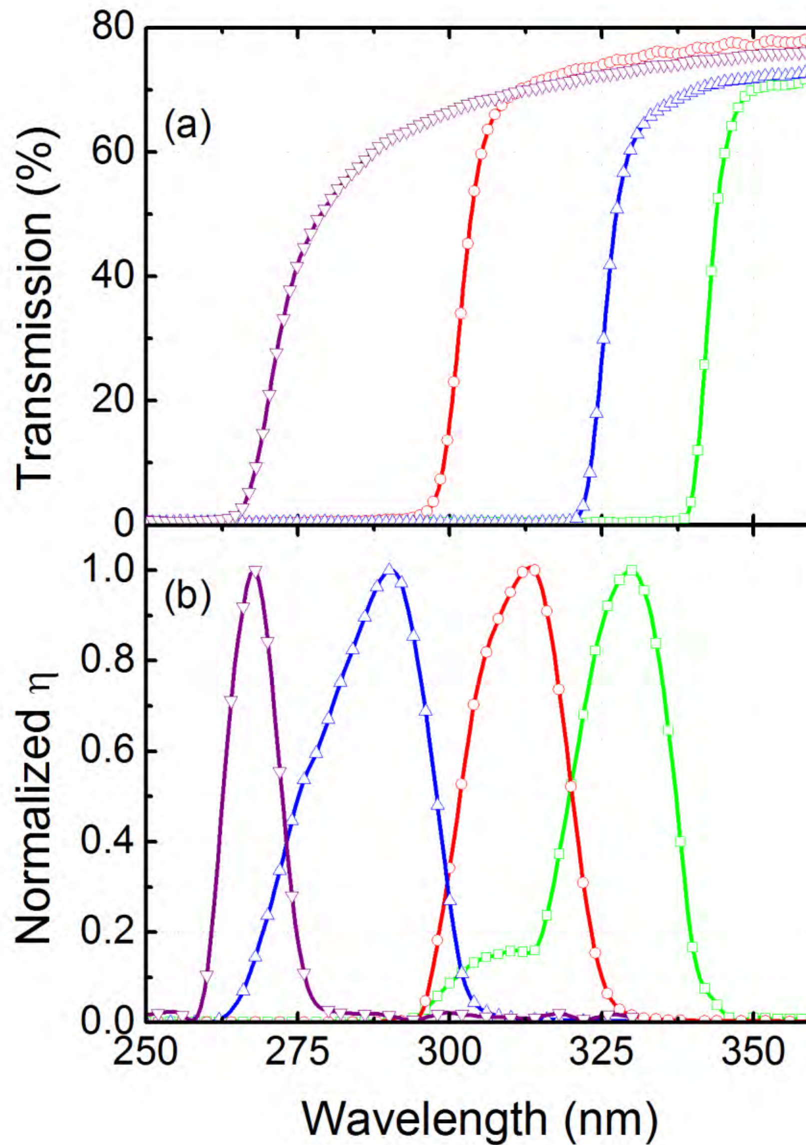

Figure 3.11: Comparison of the spectral response and the transmission measurements. (a) Spectral transmission measurements of the recess etched layers. (b) Normalized spectral quantum efficiency of a final device.

IV measurements of the fabricated photodetectors are shown in Figure 3.12. Devices again exhibited expected current voltage characteristics for such a high band gap material except the device 2. We believe that the structural deformities in $Al_{0.14}Ga_{0.86}N$ are the main reason for this relatively high dark current which is consistent with the spectral responsivity measurements. No sign of breakdown was observed up to 100 V bias.

Table 3.4: Bias conditions and the measured peak responsivity, quantum efficiency with corresponding FWHM values of the four-color UV photodetector of sample 2.

Device	Bias Voltage (V)	Peak Responsivity (A/W)	Peak Quantum Efficiency	Wavelength (nm)	FWHM (nm)
1	0.2	1.00×10^{-1}	0.40	328	18.3
2	5	1.60×10^{-1}	0.65	309	17
3	5	7.60×10^{-2}	0.60	290	21.6
4	20	3.40×10^{-2}	0.16	267	8.7

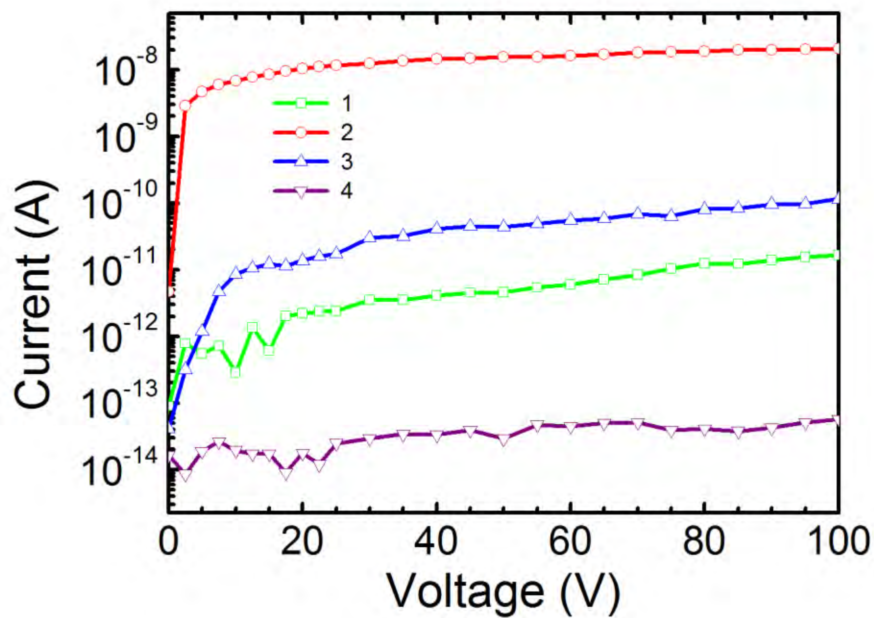

Figure 3.12: IV measurements of the fabricated photodetectors on sample 2. The numbers denote the quadrants from top to bottom.

3.3.3 Conclusion

We successfully demonstrated the concept of a four-color back-illuminated UV MSM photodetector on a single chip in the wavelength range from 255 nm to 350 nm. This was achieved by epitaxially growing of four distinct AlGaN layers with one extra filter layer in the bottom on double side polished sapphire substrate by MOCVD. Each layer acted as both active absorber and a band blocking filter. The layers were reached by recess etching of the top layers. Four distinct peaks observed in the quantum efficiency spectra with some overlap. Peak wavelengths were at 328, 309, 290 and 267 nm and the FWHMs were 18, 17, 22 and 9 nm, respectively from top to bottom. Dark current was remained below 10 pA for all devices except the device 2.

3.4 Four-Color sensing UV photodetectors with extra filter layers

This section along with the section 3.3 was submitted as "Four-color ultraviolet metal-semiconductor-metal AlGaN photodetectors" Mutlu Gokkavas, Serkan Bütün, Wlodek Strupinski and Ekmel Özbay, Semicond. Sci. Tech. October, 2011.

Ultraviolet (UV) light sensitive devices are fabricated on AlGaN templates grown on c-plane sapphire by metal-organic chemical vapor deposition. We fabricated back illuminated metal-semiconductor-metal (MSM) photodiodes with multiple color sensitivity on single epitaxial structure. Our devices consist of four active layers which are sensitive to different portions of the UV spectrum. We incorporated the extra filter layers of the epitaxially thick (around 0.5 μm) in between active layers of 0.5 μm in order to suppress the other part of the spectrum. We fabricated 4 separate MSM diodes on 4 different active layers by recess etching of the surface. The resultant device showed well

separated four peaks at 267, 295, 316 and 335 nm with FWHM of 9, 11, 13 and 10 nm respectively.

3.4.1 Concept

In this work, we tried to improve the previous idea of four-color sensing device with extra intermediate filters. Eight layer of AlGaN with changing Al content is utilized for fabrication of the four-color UV photodetector. The basic mechanism of this device is quite similar to the ones described above (on page 22 and 32). The photodetectors are fabricated on every other layer, leaving one extra layer for further suppression of the band in between the adjacent photodetector bands.

3.4.2 Fabrication and Results

Similar technique was used for the epitaxial growth of nine $Al_xGa_{x-1}N$ layers with different Al content on C-plane double side polished sapphire substrate as described in section 3.2.2 above. The epitaxial growth started with a 15 nm AlN nucleation layer, and then followed by a 150 nm thick AlN buffer layer. After that the growth of nine $Al_xGa_{x-1}N$ layers with decreasing Al content was completed. No extra nucleation layers were grown in between the active and passive layers.

We performed spectral transmission measurements in order to measure the band edges of each layer as described in the section 3.2.2. The resulting transmission curves as a function of etch depth is compared in Figure 3.13.

We calculated the Al contents of each layer by the band edges. The final composition of the wafer is presented in Table 3.5. We conclude that, eight distinct layers of different Al content with abrupt junctions were successfully grown on sapphire by MOCVD. Sample was suitable for four-color monolithic photodetector application with filter layers judging by the positions of the band edges.

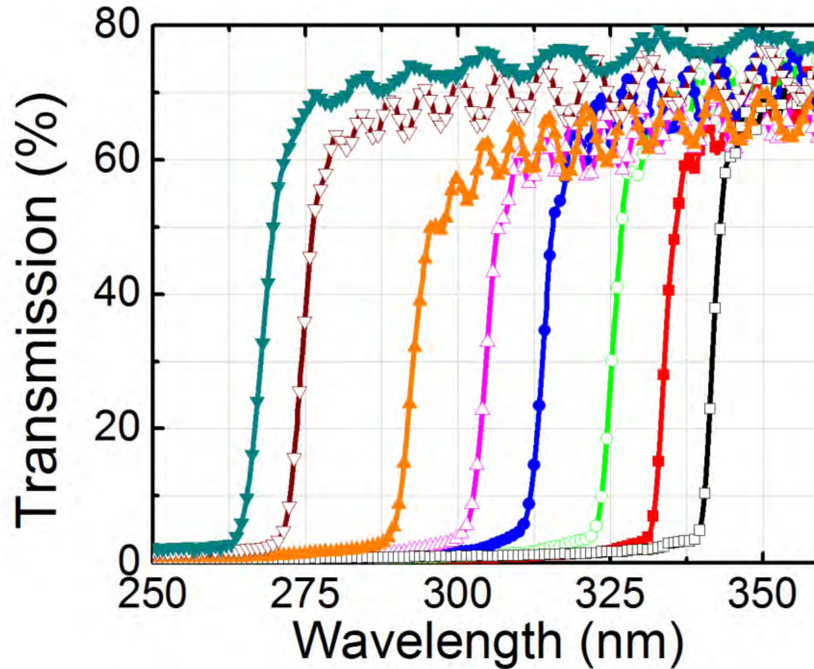

Figure 3.13: Spectral transmission measurements of the recess etched 8 layered sample. Each photodetector was fabricated on layers with open symbols whereas the full symbols represent the corresponding filter layers.

We fabricated four-color photodetectors on this eight layered wafer using the multi-color photomask as described in chapter 3.3.2. We performed leakage current and spectral responsivity characterizations on these devices, as well.

Spectral responsivity measurements were performed as described in chapter 3.2.2. The corresponding normalized quantum efficiency results are represented in Figure 3.14. Here the different bias conditions are selected for better visualization of the figure. The actual biasing conditions are represented in Table 3.6. The device has four distinct bands with almost 2 orders of magnitude rejection to the neighboring bands (see Figure 3.15). In addition, the FWHM values are reduced by almost half in comparison with the device without the filter layers for the top three peaks. The fourth photodetector in both devices has similar characteristics in terms of FWHM which is because the bottom filter layer has same Al content in of both of the devices.

Table 3.5: The summary of the epitaxial structure of the eight layer for the four color photodetector with extra filter layers.

Layer	Thickness (nm)
$Al_{0.08}Ga_{0.92}N$	500
$Al_{0.16}Ga_{0.84}N$	500
$Al_{0.20}Ga_{0.80}N$	500
$Al_{0.25}Ga_{0.75}N$	500
$Al_{0.31}Ga_{0.69}N$	500
$Al_{0.40}Ga_{0.60}N$	500
$Al_{0.45}Ga_{0.55}N$	500
AlN	150
Sapphire	substrate

Table 3.6: Bias conditions and the measured peak responsivity, quantum efficiency with corresponding FWHM values of the four-color UV photodetector with filter layers.

Device	Bias Voltage (V)	Peak Responsivity (A/W)	Peak Quantum Efficiency	Wavelength (nm)	FWHM (nm)
1	2	6.70×10^{-2}	0.25	336	8.3
2	1	1.20×10^{-1}	0.47	316	12.1
3	2	3.40×10^{-2}	0.14	295	11.4
4	20	5.90×10^{-3}	0.03	268	8.1

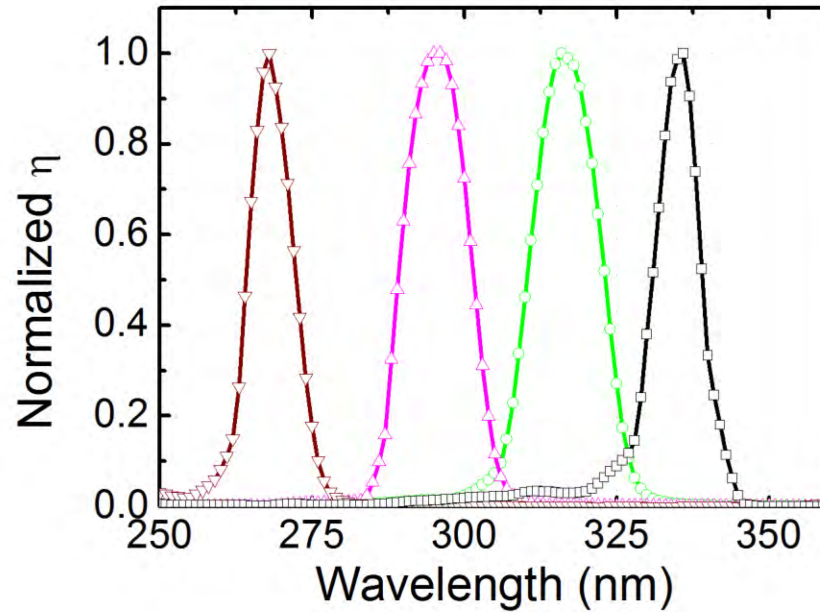

Figure 3.14: Spectral normalized quantum efficiency measurements of the four-color sample with extra filter layers. Colors of the curves are matched to that of layers represented in figure 3.13 on which each photodetector was fabricated.

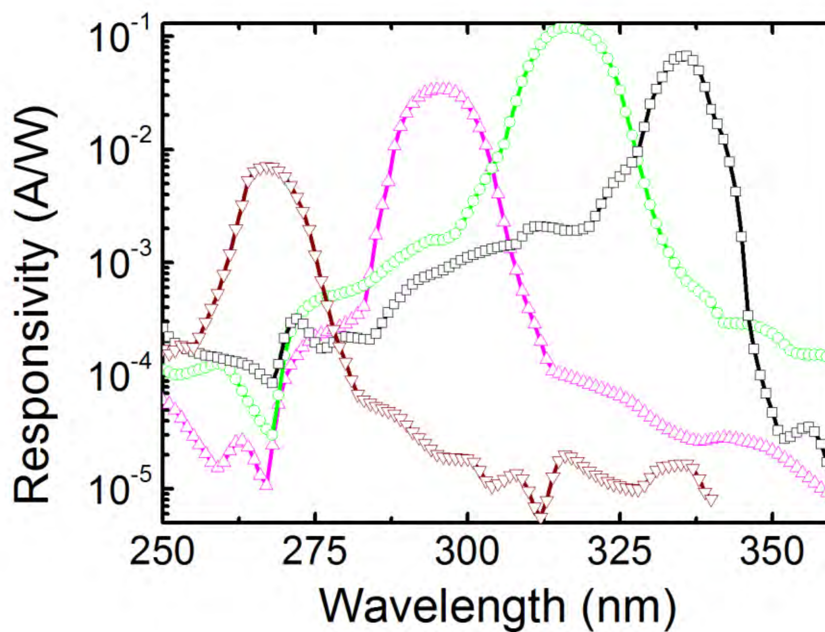

Figure 3.15: Spectral responsivity measurements of the four-color photodetector with extra filter layers in log scale. The bias conditions of the each quadrant are given in table 3.6.

The leakage current measurements were performed as described in chapter 3.2.2. The results were illustrated in figure 3.16. The photodetectors 1 and 2 exhibited excellent dark current behavior. Dark current was below 100 fA up to 100 V bias. On the other hand, the photodetectors 3 and for showed fairly good results. Dark currents in this case remain below 10 pA and 100 pA for photodetectors 3 and 4, respectively. This can be attributed to the surface damage caused by the prolonged RIE process.

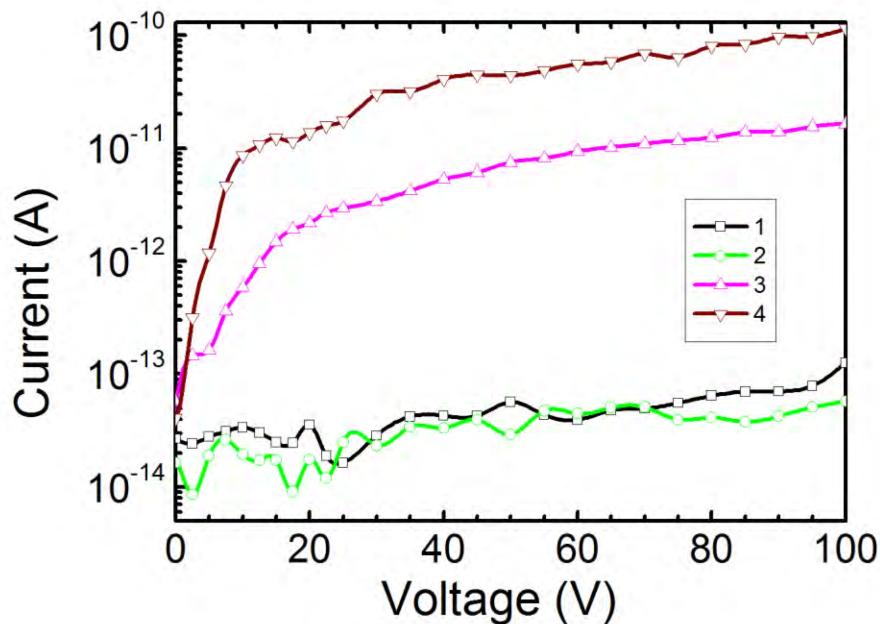

Figure 3.16: Leakage current characteristics of the four-color photodetector with filter layers. The numbers denote the quadrants from top to bottom.

3.4.3 Conclusion

We improved the concept of a four-color back-illuminated UV MSM photodetector on a single chip in the wavelength range from 255 nm to 350 nm. This was achieved by epitaxially growing of eight distinct AlGaN layers with on double side polished sapphire substrate by MOCVD. Every first layer of two acted as active absorber and the second acted as a band blocking filter. The layers were reached by recess etching of the top layers. Four distinct peaks observed in the quantum efficiency spectra with reduced overlap. The rejection

ration was about two orders of magnitude for each band. Peak wavelengths were at 336, 316, 295 and 268 nm and the FWHMs were 8, 12, 11 and 8 nm, respectively from top to bottom. Dark current was remained below 10 pA for all devices except the device 4.

Chapter 4

UV Sensitive Nano-structured Photodetectors

4.1 Introduction

Light detection garners a great deal of interest for many applications such as, solar cells, communication, imaging etc. They all share one common component that somehow absorbs the electromagnetic energy i.e. photon, and converts it to some other form of quasi-particle (electron-hole pairs, or phonons) to be measured. Technological advancements have led to the miniaturization of all the components in electro-optic circuits in order to overcome space and sensitivity issues. The reduction of the absorption cross section is the main setback for the miniaturization of the volume of a photodetector. The integration of plasmonic nano-structures with solid-state devices has opened a new way to incorporate light into integrated circuits [32]. A properly designed plasmonic structure can focus the light in small spaces beyond the diffraction limit [35, 104]. Therefore, a carefully designed plasmonic antenna positioned on top of a photodetector, which is smaller in size than the wavelength of the incident light, can be used to collect more photons. There are many experimental and computational examples reported for such devices from the near-IR to visible spectrum [40, 41, 43, 45, 46, 105, 106]. However, there are not many research reported on plasmonic structures in the UV region. The commonly used metals silver and gold cannot be used in the UV region, simply because they do not support surface plasmons in this spectral region, whereas aluminum has a much higher bulk plasma frequency (approx. 15 eV) and supports surface plasmons in UV. Therefore, a correct metal would be aluminum for UV plasmonics. An optically small UV photodetector has many potential applications such as data storage, all optical integrated circuits, and focal plane arrays. Extraordinary UV

transmission through aluminum gratings [107], nanoholes [108] and enhanced light emission from AlGaN/GaN quantum wells by surface plasmon resonance [109] has been reported. However, no plasmonic structure integrated photodetector working in the UV is reported up to now.

In this chapter, we present our work on enhancement of the detectivity performance of GaN based MSM UV photodetectors using plasmonic structures. We applied two different techniques. First one is by exciting localized surface plasmon resonance (LSPR) on Al nano-dots fabricated on GaN surface. In the second structure we decorated the surface of the Schottky contacts with plasmonic gratings to excite the surface plasmon polaritons (SPP) to focus the incident light in a sub-wavelength volume.

4.2 LSPR enhanced MSM UV photodetectors

This chapter was submitted as "UV-LSPR enhanced GaN MSM photodetectors using Al nano-particles" Serkan Bütün, Neval Ayşegül Cinel and Ekmel Özbay, Nanotechnology. December, 2011.

We fabricated LSPR enhanced UV photodetectors on MOCVD grown semi-insulating GaN. Plasmonic resonance in UV region was attained using 30 nm diameter Al nano-particles. Extinction spectra of the nano-particles were measured through spectral transmission measurements. Spectral responsivity measurements revealed an enhancement factor of 1.5.

4.2.1 Introduction

LSPR enhanced UV photodetector consists of Al nano-particles fabricated between the Schottky contacts of an MSM photodetector on semi-insulating GaN active layer. A schematic drawing of the fabricated device is shown in figure 4.1. We fabricated Al nano-dots of 30 nm diameter and 100 nm of period with e-beam lithography. We used Al because, plasma frequency of widely used metals such as Ag and Au is not sufficient to create a plasmonic response at UV regime which is required for GaN platform. Bias voltage was kept low in order to collect the photo-generated carriers near the vicinity of the

Schottky contacts. We were able to compare the effect of plasmonic particles on the quantum efficiency of the device.

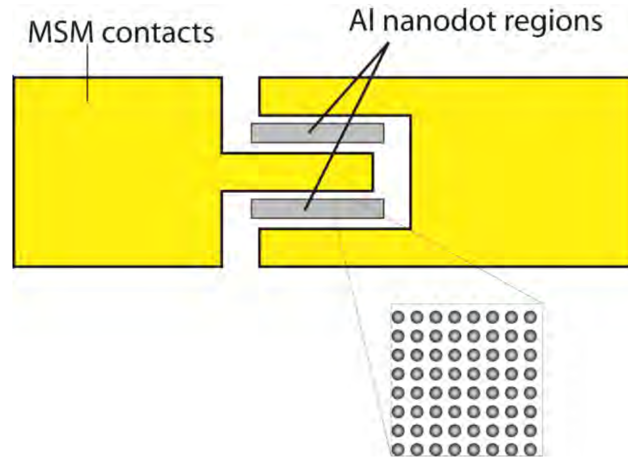

Figure 4.1: Conceptual drawing of an LSPR enhanced MSM photodetector. (viewed from the top)

4.2.2 Fabrication and Results

The Al nano-particles were fabricated using Raith E-line e-beam lithography system. Single dot exposure was used and the diameter of the particles was varied by changing the dose of the exposure. Sapphire and GaN was used as a substrate for the fabrication. We later used samples on sapphire for transmission measurements whereas GaN samples were fabricated for photodetectors. We fabricated several samples with different particle diameters and periods. Diameters of the particles were varied between 20 to 60 nm in 5 nm step while period was varied from 100 to 200 nm in 25 nm steps. The total area covered with nano-particles was 50 × 50 μm^2.The details of the e-beam lithography steps are covered thoroughly in appendix B.

We have designed and assembled a custom spectral micro-transmission setup for the extinction measurements of the fabricated Al nano-particles (Figure 4.2). The light from a broad spectrum Xe lamp (1) is carried to a collimating f-number matched UV lens (2) through a non-solarized UV multimode fiber. Then light is focused on the sample with the secondary lens (3). Sample is mounted on a special pcb board (x) and is placed on a micro-

positioner for translation. After passing through the sample, the light is collected with the imaging lens (4). Image is projected on to a plane where there is placed a variable aperture (5). This aperture allows us to select the area where a transmission measurement is desired. Light is then folded by an easy mount mirror (6) towards camera focusing optics (7). We monitor the position of the samples with a CCD camera (8). We remove the folding mirror after the individual nano-particle area is aligned and selected with the aperture. Another focusing (9) lens couples the light to the collection fiber. The spectrum is then measured by Oceanoptics USB4000 model spectrometer (10).

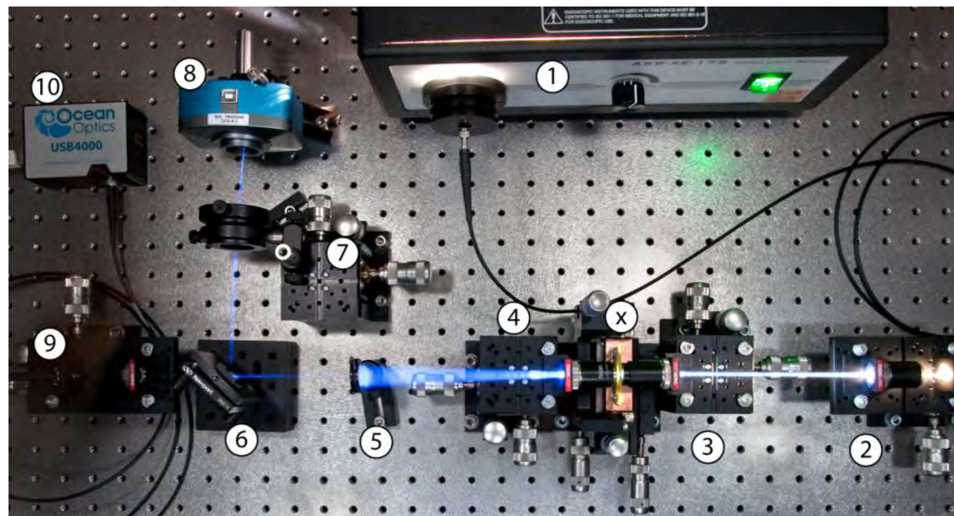

Figure 4.2: A photograph of the micro-transmission setup.

Figure 4.3 illustrates the fabricated Al nano-particles and the spectral transmission response of the structure. The size distribution suggests a very uniform fabrication. Here we present two selected extinction spectra of Al nano-particles with two different wavelengths. The resonance shifts towards red as the diameter of the particle increases. This is expected. In addition resonance gets stronger as the diameter increases because particles become more closely packed which increases the inter-coupling between the particles. We performed Finite difference time domain (FDTD) simulations for further justification of the measurements using a commercial software package by Lumerical Inc. Our simulations are in excellent agreement with the measured values. It should be

noted that these are fabricated on sapphire which has a refractive index of 1.8. Actual devices are fabricated on GaN nitride which has a much higher refractive index (~2.5). This will cause a red-shift in the resonant wavelength. We expect the peak resonance will be at 339 nm for 36 nm diameter particles when they are fabricated on sapphire. Here we assumed the effect of substrate on effective refractive index of the surrounding is limited by the bottom area of the nano-particle.

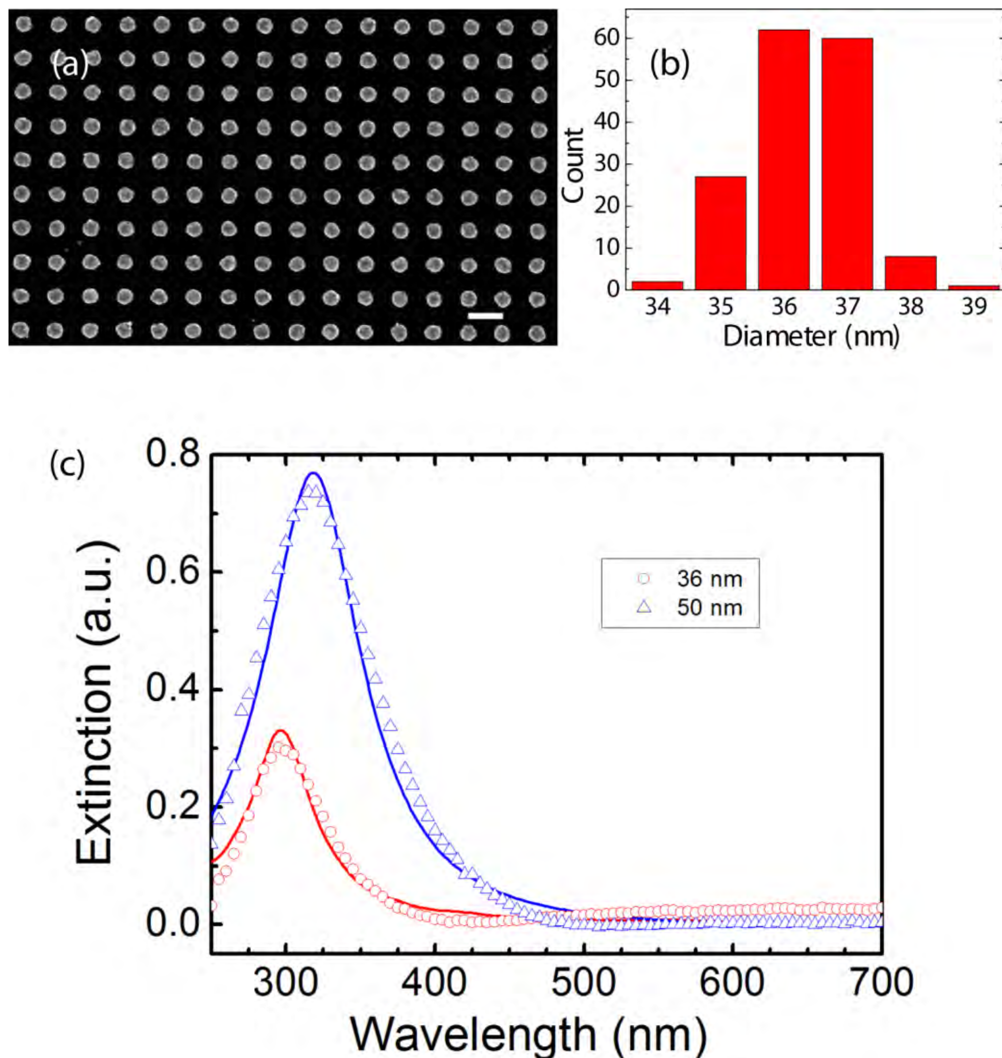

Figure 4.3: Fabricated Al nano-particles: (a) A scanning electron microscopy image of the particles. Scale bar is 100 nm. (b) Size distribution of the particles in the image in (a). (c) The extinction spectra of the Al nano-particles with two different diameters fabricated on sapphire. Dots represent the measurements whereas lines correspond to FDTD simulations.

The fabrication of the MSM photodetectors started with Schottky contact metallization with optical lithography. The contact distance was 20 μm. We used Ni/Au as contact metal. The design includes large probing pads. Therefore this was a single step process. The we fabricate Al nano-particles with 36 nm diameter and 100 nm in period with e-beam lithography. The size and the period of the particles are then confirmed with scanning electron microscopy (SEM).

Responsivity measurements were performed as decried in chapter 3.2.2 and figure 3.5. We used top illumination. Therefore the fiber probe is places on the top side of the probe station. Results are illustrated in figure 4.4 in a comparative manner. Results revealed a significant increase in the quantum efficiency around 340 nm. We analyzed these results further in order to calculate the enhancement. Figure 4.5 shows that we have almost 50% enhancement in the quantum efficiency which is due to the localization of the incident electromagnetic field on the surface where the most of the light is collected in an MSM photodetector. Here we cut the curve at 360 nm simply because the data at longer wavelengths has no meaning since GaN is completely transparent in that region.

4.2.3 Conclusion

In conclusion, we examined the effects of plasmonic scattering on absorption and photocurrent collection in the prototype visible blind GaN photodetector with size-optimized Al nano-particles. At wavelengths of surface plasmon resonance, scattered incident light by the nano-particles yields enhanced absorption in the active layer of the photodetector. Al nano-particles were first investigated separately via spectral transmission measurements. An enhancement of 50% at 339 nm is measured in the fabricated photodetector. Results showed that scattering with nano-particles enhances the absorption in the UV region. This enhancement can increase the detectivity performance of a photodetector.

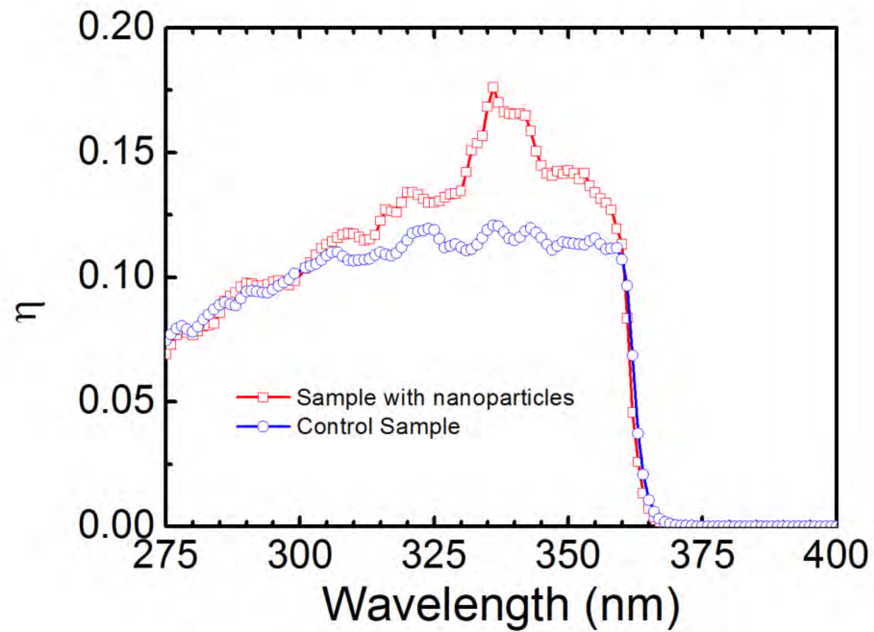

Figure 4.4: Spectral quantum efficiency measurement of LSPR enhanced photodetector along with the control sample.

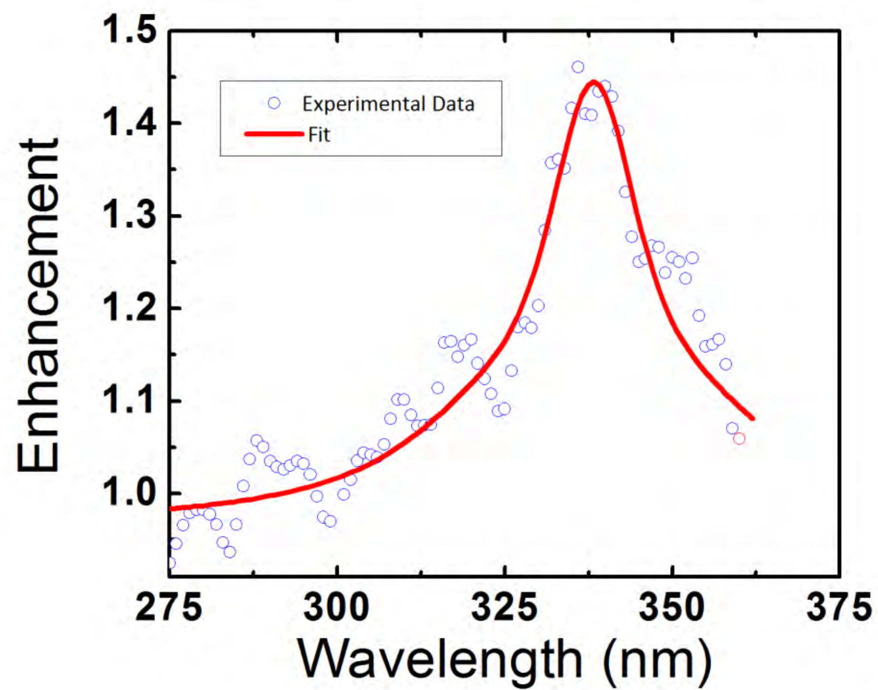

Figure 4.5: Enhancement of the quantum efficiency with Al nano-particles.

4.3 Sub-wavelength UV photodetector with integration of a nanoantenna

This chapter was submitted as "Nanoantenna coupled UV subwavelength photodetectors based on GaN" Serkan Bütün, Neval Ayşegül Cinel and Ekmel Özbay, Optics Express. December, 2011.

The integration of plasmonic structures with solid state devices has many potential applications. It allows the coupling of more light into or out of the device while decreasing the size of the device itself. Such devices are reported in the VIS and NIR regions. However, making plasmonic structures for the UV region is still a challenge. Here, we report on a UV plasmonic antenna integrated metal semiconductor metal (MSM) photodetector based on GaN. We designed and fabricated Al grating structures. Well defined plasmonic resonances were measured in the reflectance spectra. Optimized grating structure integrated photodetectors exhibited more than sevenfold photocurrent enhancement.

4.3.1 Introduction

In this work, we designed and fabricated a plasmonic antenna on top of an optically small UV photodetector based on GaN. We measured the photocurrent enhancement due to the nano antenna.

The physical mechanism behind the enhanced detection is similar to that in extraordinary light transmission (EOT) through sub-wavelength holes. There are reports suggesting that EOT is in fact due to the coupling of leaky surface waves [47] which is a similar concept demonstrated in microwaves [34, 110-114]. It is as well suggested that SPPs shifts the resonance and contribute to the EOT especially in long ranges where sub-wavelength slits are not coupled. It is known that the effect of the leaky surface waves are no more than a couple of wavelength in range where as SPP can propagate more than 10 times the wavelength of the incident light. In this work, we designed sub-wavelength detectors arrays of 10 times the operation wavelength apart. We further

investigated the mechanism behind the enhanced detection with FDTD simulations by comparing the enhancement Al and perfect electric conductor gratings.

The grating structure is one of the possible ways to excite SPP on the metal-dielectric interface. The dispersion relation of the SPP is given as follows [33]:

$$k_x = k_0 \sin\theta \mp \frac{2\pi l}{\Lambda} = k_0\sqrt{\frac{\varepsilon \cdot \varepsilon_d}{\varepsilon + \varepsilon_d}} \qquad l = 1,2,\ldots \tag{4.1}$$

where k_x, θ, Λ, ε and ε_d are the horizontal component of the momentum of incident light with momentum k_0, incidence angle, grating period, the dielectric function of the metal and dielectric function of the surrounding medium (air), respectively. Here, an in-plane momentum component $2\pi l/\Lambda$ of the grating is required to match the momentum conservation condition. Note that incident light should be in TM mode in order to excite SPP. In addition, the propagation length of the surface plasmons on metal dielectric interface is given as [33]

$$L_i = \frac{1}{2k_x''} \tag{4.2}$$

where k_x'' is the imaginary part of the surface plasmon wavenumber. Given the dielectric permittivity of the Al, we calculated the propagation length as 4.2 µm at 320 nm UV excitation. MSM contact width was chosen as 3 µm in order to be below this value.

4.3.2 Fabrication of the Plasmonic Photodetectors

We used the so-called semi-insulating GaN template for this work. Our previous research proved the superior quality of SI-GaN over the regular one [19, 115]. Especially the low dark current was needed for the current work since the separation between the contact electrodes was very small. Therefore, the growth conditions were kept very similar to that reported in our previous work. The GaN epitaxial sample used in this study was grown on c-plane sapphire in a cold wall low pressure MOCVD reactor. The Ga, Al, and N sources were

Trimethylgallium (TMGa), trimethylaluminum (TMAl), and ammonia (NH3), respectively, which were carried by hydrogen gas. The sapphire substrate was annealed at 1100ºC for 10 min for surface decontamination and cleaning, in the beginning. An essential 15 nm-thick AlN nucleation layer to compensate for the sapphire-AlN lattice mismatch was deposited at 840°C. Consequently, the reactor temperature was gradually increased to 1,150°C and an AlN buffer layer was grown. The growth was interrupted here to ensure the formation of abrupt AlN-GaN interface, meanwhile the growth conditions for GaN was achieved. An approximately 1 µm thick GaN layer was grown under the following conditions: reactor pressure 200 mbar, growth temperature 1070 ºC, and a growth rate of approx. 2 µm/h.

All the steps required for the fabrication of the plasmonic photodetectors were performed by electron beam lithography. We used polymethyl methacrylate (PMMA) as the e-beam resist and a two step lift-off process for the fabrication. The MSM contacts and the access pads were defined in the first step. The slit width between the contacts was optimized by varying the dose of e-beam exposure. The width of the contacts was 3 µm and the side size of each square in the photodetector was 150 µm. Then, the Ni/Al (10 nm/100 nm) metal pair was evaporated by e-beam evaporation. Ni was selected for its good Schottky contact characteristics on GaN, whereas Al was selected to maintain surface plasmon polaritons in the UV region because of its high plasma edge (15.2 eV). In the second step, gratings were written on a single part of the photodetector structure (see figure 4.6). The actual sample grating period was 314 nm and duty cycle was 1/3. We evaporated 40 nm Al as grating metal.

Optimization samples for reflection measurements were fabricated in the same manner on bare sapphire substrates. We prepared 300 × 300 μm^2 squares with the same slit spacing as on the device but various grating periods using the same metal type and thickness as described above (see Figure 4.7b and c). We also prepared slit samples without gratings for the reference measurements.

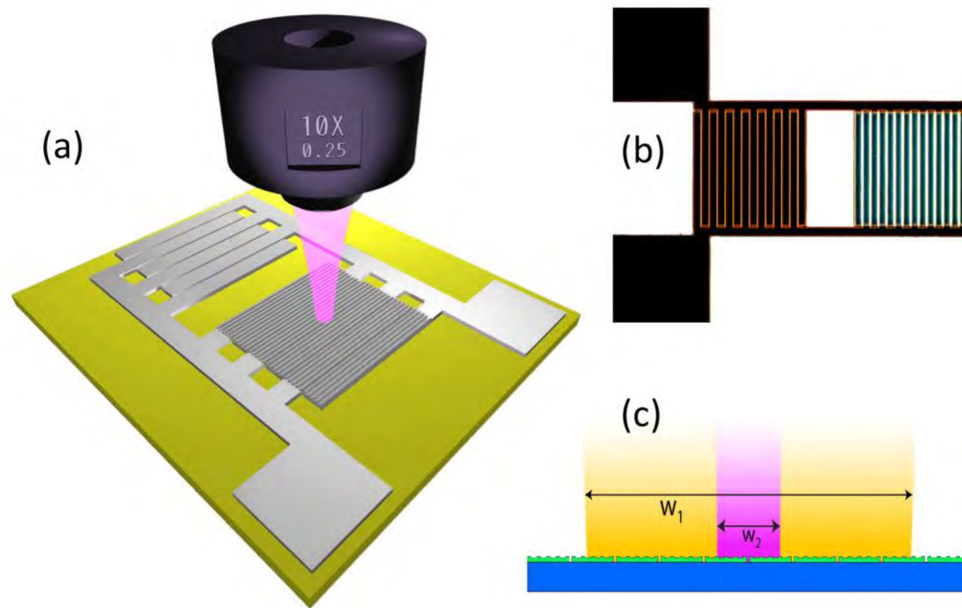

Figure 4.6: Conceptual drawing of the nano-structured MSM photodetector (a). A UV objective of numerical aperture 0.25 is used to illuminate a selected portion of the device. (b) Dark-field microscopy image of a fabricated MSM photodetector with (bluish part) and without (dark part) grating is shown. (c) illustration of the beam size over the MSM fingers for spectral measurement setup (w_1) and for laser setup (w_2)

The reflection characteristics of the samples with various grating periods were carried out by ellipsometric measurements with Sentec 850 model ellipsometer equipped with a micro-spot adaptor. The measurement angle was 70°. Gratings were aligned such that they lie perpendicular to the plane of incidence. The reflected light collected from both samples with grating and reference samples, separately. Figure 4.7a presents the relative (wrt reference) spectral reflection data from three samples with different grating periods. There are resonant dips due to coupling to SPPs, which are red shifted as the grating period increases. We numerically calculated the dispersion relation of the grating ($\Lambda = 300$ nm) as a function of both the wavelength and angle of incidence (Figure 4.7b). The resonance for an incidence angle of 70° is around 585 nm, which is in good agreement with the measured value (red curve in figure 4.7a). Figure 4.7b also shows that as the incidence angle decreases, the

resonance wavelength shifts towards the UV region where the GaN material has

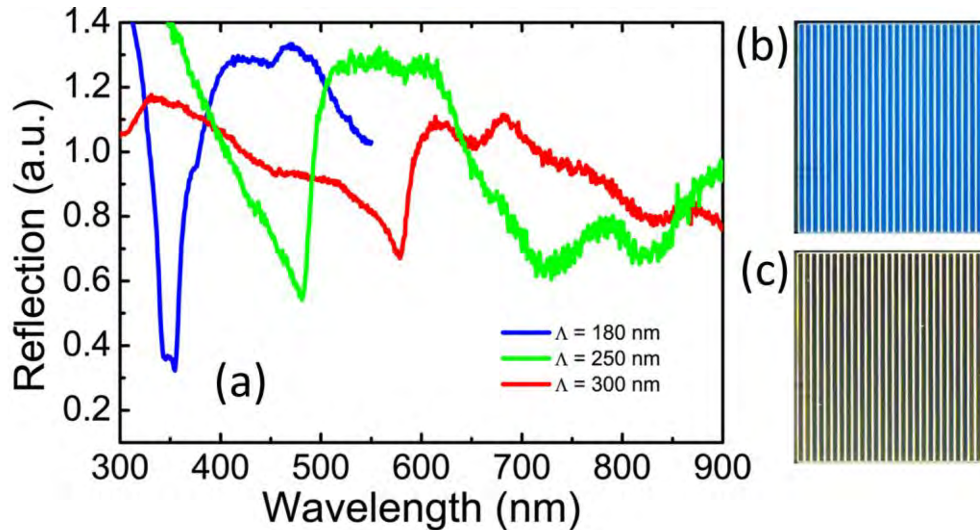

Figure 4.7: Characterization and the optimization of the plasmonic gratings. (a) Reflectance measurements of fabricated gratings with a different grating period as a function of wavelength. Dark field optical microscopy images of the slit structures with a grating of period 300 nm (b) and without grating (c). The subwavelength slits can be seen as white lines in both of the images.

high absorption. Dark field microscopy images of the samples are shown in figure 4.7c with the grating (Λ = 300 nm), and in figure 4.7d without the grating. A bluish color was reflected from the grating sample since the reflection from the red portion of the spectrum is suppressed due to SPP excitation (see red curve on figure 4.7a). The reference sample, on the other hand, appears dark because there no specific wavelength dependence in the reflectance spectra.

4.3.3 Characterization of Nano-Photodetectors

We measured the current-voltage (IV) characteristics (Figure 4.8c) of these devices in order to be sure that very closely separated MSM contacts are in fact working properly. The results indicated that, even if MSM contacts are as close as 150 nm (see figure 4.8a and b), they are well isolated from each other. The device break down voltage is measured around 15 V. That means, the active GaN layer stands for an electric field strength of over 1.0×10^6 V/cm. These values prove the good epitaxial and surface quality of our GaN material.

Spectral device performance was characterized by a synchronous detection scheme. We illuminate the devices using a 10X UV objective with a numerical aperture of 0.25. The output of the Xe light source was monochromated and polarized, then coupled to the illumination objective. The incoming UV light is focused to a specific site on the photodetector with a spot size of 20 um. Light was mechanically chopped and the photocurrent was recorded with a lock-in amplifier. We measured the optical power at the end of the optical path using a calibrated Si photodetector, as well. First, one side of the device where there is no grating on the contacts was illuminated and then the spectral photocurrent was recorded. After that, other side of the device where there is grating on the contacts was illuminated again the spectral photocurrent was recorded. The measured spectral photocurrent data is compared in figure 4.8d. The peak photocurrent value for illumination over the grating site is 24.5 pA, whereas it is 3.4 pA for illumination over the no grating site at zero volt bias. These values correspond to the responsivities of 1.7 mA/W and 0.2 mA/W, respectively. There is an enhancement factor of about 8 at 322 nm in terms of responsivity.

There is a quite good agreement when we compare the width of the absorption band from 300 to 360 nm (Figure 4.8e) to the reflectance measurements (Figure 4.7a red curve). This further proves the enhancement is in fact due to the surface plasmon resonance. We further measured photocurrent under linearly polarized 325 nm wavelength He-Cd laser source, which has an optical over 3 orders of magnitude higher than our spectral setup. The spot size in this case was about 3 μm in diameter. It was safe to argue that we illuminate at most two slits at ones. Measured photocurrent in TM mode was 60 nA at the grating site, where as it was 9 nA at the reference site. The photocurrent in TE mode was 9 nA and 8 nA for grating site and the reference site, respectively. These numbers also supports our spectral measurements

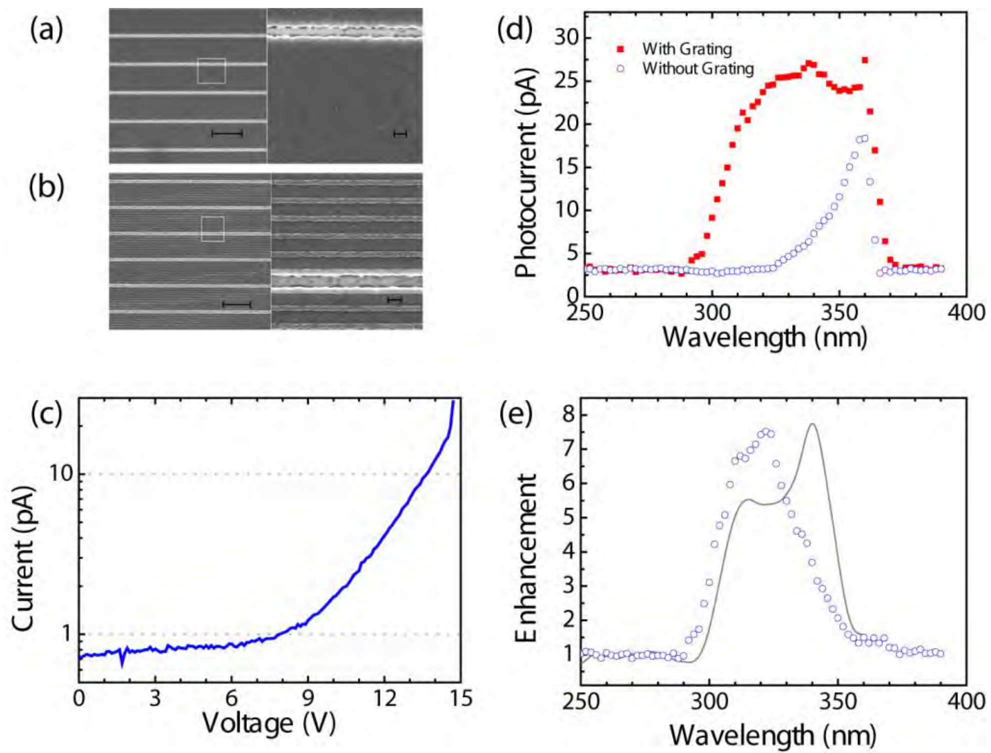

Figure 4.8: The fabrication and the measurements of the subwavelengt photodetectors. Scanning electron microscopy images of the interdigitated MSM contacts (a) without the grating and (b) with the grating fabricated on top are shown. The longer and the shorter scale bars indicate 3 *μm* and 200 *nm* respectively. The measured dark current-voltage characteristics and the measured spectral photocurrent comparison are displayed in (c) and (d) respectively. The corresponding spectral enhancement is shown in (e). The dots are measurements and the solid line is the FDTD simulations of the fabricated device.

4.3.4 FDTD Simulations

The optical measurements were justified by simulations done using a finite-difference time-domain (FDTD) algorithm based commercial software package developed by Lumerical Inc. The material data of Al and GaN were taken from Palik [116] and Brunner *et.al.* [76] respectively. The mesh sizes were set to values less than or equal to $\lambda/14$, where λ is source wavelength divided by the refractive index of material of interest. The boundary conditions were set as perfectly matched layer (PML) in order to eliminate undesired reflections from boundaries. The simulation software ensures numerical stability by setting the time step less than 0.02 fs based on the chosen mesh sizes. The total absorbed light intensity is calculated by the integration of the E-field intensity over time

and space. The enhancement in absorption is then determined by comparing the structure with and without the metal gratings for the TM mode. Figure 4.9a compares the abortion enhancement for the same grating/slit combination for various grating materials. We included a hypothetical perfect electrical conductor (PEC) by setting the imaginary part of the material to an exceptionally high value to evaluate the effect of geometrically excited ESWs. Figure 4.9c and d compares the total amount of absorbed light at a resonant (340 nm) and an off-resonant (280mn) wavelengths, respectively.

The numerical simulations revealed that neither Au nor Ag could be used for photocurrent enhancement in UV photodetectors (Figure 4.9a). The first reason is that they do not support SPPs in this region due to their permittivity. If we refer to the dispersion curves (Figure 4.9b) of these metals there are no available modes in the region (shaded area) where GaN has absorption. On the other hand, the sub-wavelength groves are effectively invisible to the incident wave. Therefore, they cannot excite evanescent waves on the surface. On the other hand the PEC curve proves that the geometrical excitation of the evanescent waves plays an important role in the enhancement. However, when we compare this to the Aluminum we conclude that the spectral behavior of the absorption changes significantly. This proves the role of SPPs in the process. However, the dominant mechanism behind the enhanced absorption is still unclear which is beyond the scope of this work. In addition, the E-filed intensity profiles of the Al gratings on GaN are provided in Figure 4.9c and d for further visualization of the enhanced transmission at different wavelengths. We have a clear enhancement in the intensity where the wavelength is close to the resonance whereas there is not much transmission at an off resonant wavelength.

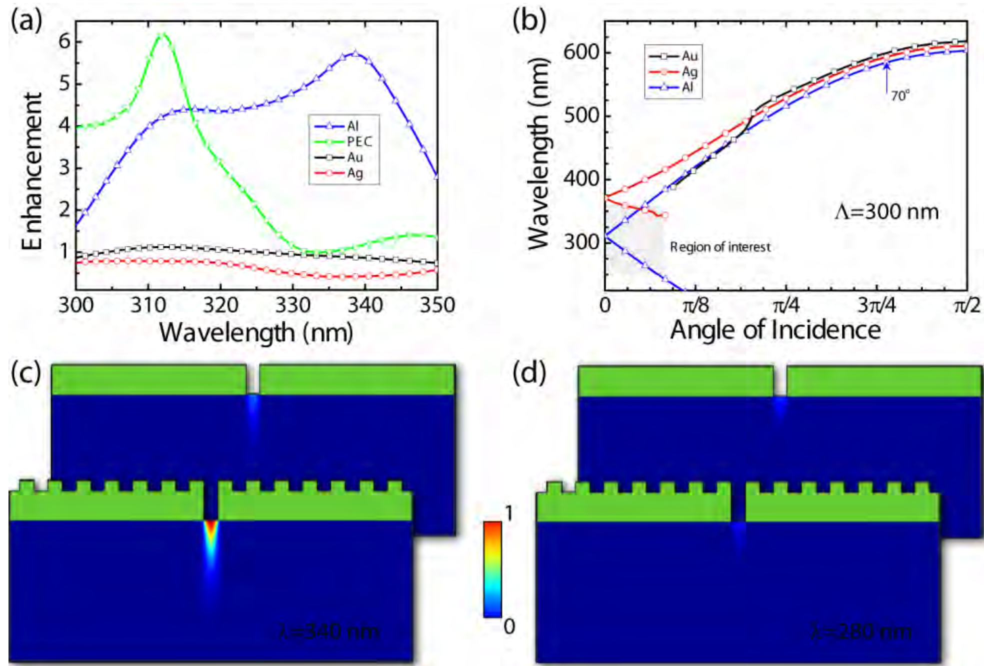

Figure 4.9: Numerical simulations of the designed grating structures. (a) The spectral absorption enhancement results for different gating materials calculated by FDTD simulations. Simulation parameters were as follows; Slit width:100 *nm*, base height: 75 *nm* and grove height: 35 *nm*. (b) Calculated SPP dispersion relation of a grating/air interface for different metals. Here the grating period is 300 *nm*. The shaded region represents the absorption of GaN in vertical and the illumination cone of the lens in our setup in horizontal. (c) and (d) are comparing the overall normalized E-field intensity under the slits with and without the gratings at a resonant and an off-resonant excitation. (The color bar applies to all)

4.3.5 Conclusion

We successfully demonstrated an UV photodetector with a nano antenna. Plasmonic resonance of the designed antenna was determined from spectral reflectivity measurements. Then, we integrated this structure with a GaN UV photodetector. The electrical characterization indicated that the devices break down voltage was 15 *V*. The leakage current remained below 1 *pA* up to 7 *V* bias, even though the MSM contacts were placed 150 *nm* apart. The responsivity values were 1.7 *mA/W* and 0.2 *mA/W* at 322 *nm* UV illumination. The measured enhancement in photocurrent was more than sevenfold. Numerical simulations revealed that this enhancement is both due to the geometrically excited

evanescent waves as well as the SPPs. The experimental measurements and the numerical calculations were in good agreement..

Chapter 5
Current Transport Mechanism Investigations of AlGaN Based Heterostructures

5.1 Current transport mechanisms and trap state investigations in (Ni/Au)-AlN/GaN Schottky barrier diodes

This section was published as "*Current transport mechanisms and trap state investigations in (Ni/Au)-AlN/GaN Schottky barrier diodes*" Engin Arslan, Serkan Bütün, Yasemin Safak, Huseyin Çakmak, HongBo Yu and Ekmel Özbay Microelectronics Reliability, volume 51, page 586 (2011) Reproduced (or 'Reproduced in part') with permission from Elsevier Ltd. © 2011 Elsevier Ltd.

The current transport mechanisms in (Ni/Au)–AlN/GaN Schottky barrier diodes (SBDs) were investigated by the use of current–voltage characteristics in the temperature range of 80–380 K. In order to determine the true current transport mechanisms for (Ni/Au)–AlN/GaN SBDs, by taking the $J_{s(\mathrm{tunnel})}$, E_0, and R_s as adjustable fit parameters, the experimental J–V data were fitted to the analytical expressions given for the current transport mechanisms in a wide range of applied biases and at different temperatures. Fitting results show the weak temperature dependent behavior in the saturation current and the temperature independent behavior of the tunneling parameters in this temperature range. Therefore, it has been concluded that the mechanism of charge transport in (Ni/Au)–AlN/GaN SBDs, along the dislocations intersecting the space charge region, is performed by tunneling. In addition, in order to

analyze the trapping effects in (Ni/Au)–AlN/GaN SBDs, the capacitance–voltage (C–V) and conductance–voltage (G/ω–V) characteristics were measured in the frequency range 0.7–50 kHz. A detailed analysis of the frequency-dependent capacitance and conductance data was performed, assuming the models in which traps are located at the heterojunction interface. The density (D_t) and time constants (η_t) of the trap states have been determined as a function of energy separation from the conduction-band edge (E_c - E_t) as $D_t \approx (5\text{-}8)\times 10^{12}$ eV^{-1} cm^{-2} and $\eta_t \approx (43\text{-}102)$ µs, respectively.

5.1.1 Introduction

AlGaN/GaN heterostructures have attracted special interest due to their potential applications in high electron mobility transistors (HEMT) operating at high power and high temperature levels [9, 117]. However, room temperature two-dimensional electron gas (2DEG) density and mobility in turn limit the sheet resistance of the channel and maximum HEMT current (1–1.5 A/mm) for AlGaN/GaN heterostructures[9]. Recently, the AlInN/GaN material system has attracted major interest for electronic applications due to its promising electronic properties, polarization effects, and high thermal stability [118]. AlInN/GaN heterostructures can further enhance the 2DEG density and lead to high HEMT current [118]. It was shown that the DC current levels in turn lead to 2.3 A/mm by using AlInN/AlN/GaN heterojunctions[119]. On the other hand, ultrathin all-binary AlN/GaN HEMTs with ultrathin AlN (2–5 nm) barriers offer higher sheet carrier density and a higher mobility 2DEG channel, which show much promise for high power, high temperature applications in telecommunications, power flow control, and remote sensing [120].

Both molecular-beam epitaxy (MBE) and metal organic chemical-vapor deposition (MOCVD) are currently used to grow high quality AlGaN/GaN and AlInN/GaN heterostructures with excellent transport characteristics [9, 117-121]. However, it is difficult to grow AlN/GaN HEMTs with high transport characteristics by an MOCVD reactor [122]. Alekseev et al. [123] reported on a low-pressure MOCVD technique for GaN/AlN heterojunction field-effect

transistor growth. Room temperature electron mobility in an optimized structure with an 11 nm barrier was 320 cm^2/Vs and the associated 2DEG density was 2.3 $\times 10^{13}$ cm^{-2}.

Because of the large mismatches in lattice constants and thermal expansion constants between GaN and all the available foreign substrates (Al_2O_3, SiC, ZnO, etc.) causes very high dislocation density ($10^8 – 10^{10}$ cm^{-2}) in a hetero epitaxially grown crystalline GaN layer [117]. The high dislocation density constitutes a serious limitation for the efficiency of radiative recombination, and also for device performance and lifetime. Evstropov *et al*. [124] and Belyaev *et al*. [125] showed that the current flow in the III–V heterojunctions, with a high dislocation density, is commonly governed by multistep tunneling with the involvement of dislocations even at room temperature.

In this study, we grow AlN/GaN HEMT structures in an MOCVD reactor and investigate the current transport mechanisms in a wide temperature range (80–380 K) in (Ni/Au)–AlN/GaN SBDs. Another purpose of this article is to characterize the density distribution and relaxation time of the interface states in AlN/GaN HEMT structures by using an admittance technique at room temperature.

5.1.2 Fabrication and Results

The AlN/GaN heterostructures were grown on c-plane (0001) Al_2O_3 substrate in a low-pressure metalorganic chemical-vapor deposition (MOCVD) reactor by using trimethylgallium (TMGa), trimethylaluminum (TMAl), and ammonia for Ga, Al, and N precursors, respectively. The buffer structures consisted of high temperature (1150 °C) 840 nm AlN templates. A 1.6 μm nominally undoped GaN layer was grown on an AlN template layer at 1050 °C, which was followed by the growth of a 4 nm thick high temperature AlN (1150 °C) barrier layer. The ohmic and Schottky/rectifier contacts were made on top of the sample at approx. 10^{-7} Torr pressure, within an electron beam (e-beam) evaporation system. The ohmic contacts were formed as a square Van Der Pauw

shape and the Schottky contacts were formed as 0.8 mm radius circular disks. After cleaning the samples, Ti/Al/Ni/Au (20/180/40/80 nm) metals were e-beam evaporated on the sample and were annealed at 850 °C for 30 s in N_2 ambient in order to form the ohmic contact. Schottky contacts were formed by Ni/Au (50/80 nm) evaporation. Room temperature 2DEG density and mobility were found to be 2×10^{13} cm^{-2} and 485 cm^2/Vs, respectively. The current–voltage (I–V) measurements were performed by use of a Keithley 2400 Source Meter. The frequency dependence of the C–V and G/ω–V measurements was obtained by using an HP 4192 A LF impedance analyzer. The measurements were performed under the sweep of bias voltage from (-6 V) to (+6 V) and a test signal of 40 mV peak to peak.

The reverse and forward bias I–V characteristics of an (Ni/Au)–AlN/GaN SBDs were measured in a wide temperature range (80–380 K). In figure 5.1 the measured reverse and forward bias J–V characteristics of an (Ni/Au)–AlN/GaN SBDs for the temperatures of 80, 200, 300, and 380 K are given. In order to correctly interpret the current transport mechanisms in the (Ni/Au)–AlN/GaN SBDs, we considered the contribution of thermionic emission (TE) current and tunneling current transport mechanisms (see Figure 5.2). The forward bias J–V characteristics, due to thermionic emission (TE), of SBDs with the series resistance (R_s) is given by [72, 126],

$$J_{Therm} = J_{s_Therm} \cdot \left(e^{\frac{q(V-IR_S)}{nkT}} - 1\right) \tag{5.1}$$

where J_{s_Therm} is the reverse saturation current derived from the straight line region of the forward bias current intercept at a zero bias. T is the absolute temperature in K, q is the electron charge, n is the ideality factor, k is the Boltzmann constant, V is the applied bias voltage, and IR_s term is the voltage drop across the R_s of structure [72, 117, 127]. The values of ideality factor n were obtained from the slope of the linear region of the J–V plots [117, 127]. The change in n with temperature is shown in table 5.1.

Table 5.1: Temperature dependent values of the tunneling saturation current density (J_{s_tunnel}), series resistance (R_s) determined by fitting expression as given in equation (5.2) to the measured forward bias J–V characteristics and the ideality factor (n) was determined from the semilog-forward J–V data set of (Ni/Au)–AlN/GaN SBDs.

T (K)	$J_{s_tunnel} \times 10^{-5}$ ($A/cm2$)	n	R_s (Ω)
80	5.7	18.9	5362
110	5.9	13.6	5090
140	6.1	10.7	5290
170	6.4	8.8	4960
200	6.7	7.6	5340
230	7.1	6.8	5890
260	7.2	6.1	6782
290	7.6	5.7	8298
300	7.6	5.6	9015
320	7.8	5.4	10,274
340	8.4	5.2	11,020
360	8.7	4.9	11,241
380	9.1	4.7	11,923

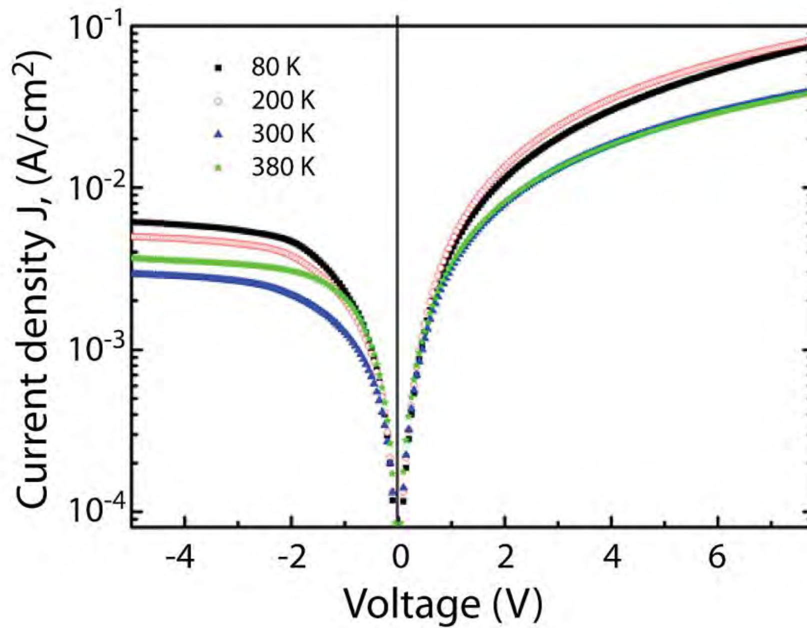

Figure 5.1: The J–V characteristics of (Ni/Au)–AlN/GaN SBDs.

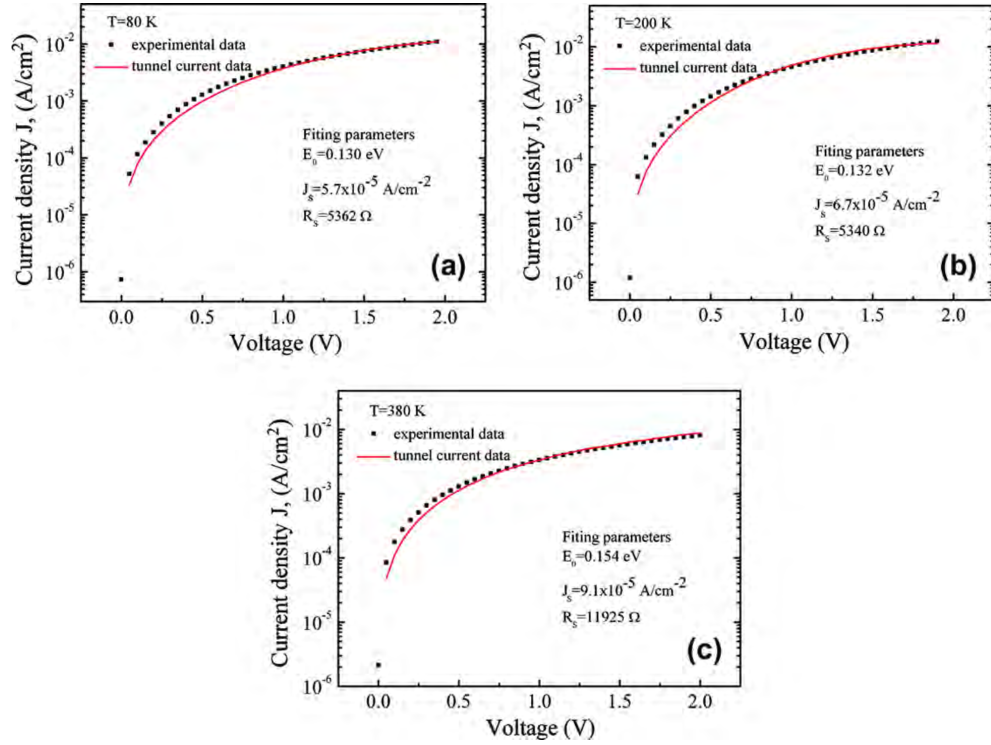

Figure 5.2: The fitting of the tunneling current expression (Equation. (5.2)) to the experimental J–V characteristics of (Ni/Au)–AlN/GaN SBDs measured at 80, 200, and 380 K.

As shown in Table 5.1, the *n* determined from semilog forward J–V plots were found to be a strong function of temperature. The ideality factor was found to increase with decreasing temperature (n = 18.9 at 80 K, n = 4.7 at 380 K). It is obvious that the ideality factors of the structures are considerably larger than unity. The tunneling current density through SBDs is given by [72, 117, 125, 127],

$$J_{tunnel} = J_{s_tunnel} \cdot \left(e^{\frac{q(V-IR_S)}{E_0}} - 1 \right) \tag{5.2}$$

where J_{s_tunnel} is the tunneling saturation current density and E_0 is the tunneling parameter. E_0 can be defined as [72, 117, 125, 127],

$$E_0 = E_{00} \coth\left(\frac{E_{00}}{kT}\right) \tag{5.3}$$

where E_{00} is the characteristic tunneling energy that is related to the tunnel effect transmission probability. In order to determine the true current transport

mechanisms for (Ni/Au)–AlN/GaN Schottky diodes, by taking the J_{s_tunnel} , E_0, and R_s as adjustable fit parameters, we fit the experimental J–V data to the analytical expressions given for the current transport mechanisms in a wide range of applied biases and at different temperatures. A standard software package was utilized for the curve fitting [117, 127]. The fit parameters were determined from the fits of the tunneling current density expression as given in equation (5.2) to the measured J–V data set. The temperature dependences of J_{s_tunnel} and E_{00} are shown in figure 5.3 and both J_{s_tunnel} and R_s values in table 5.1.

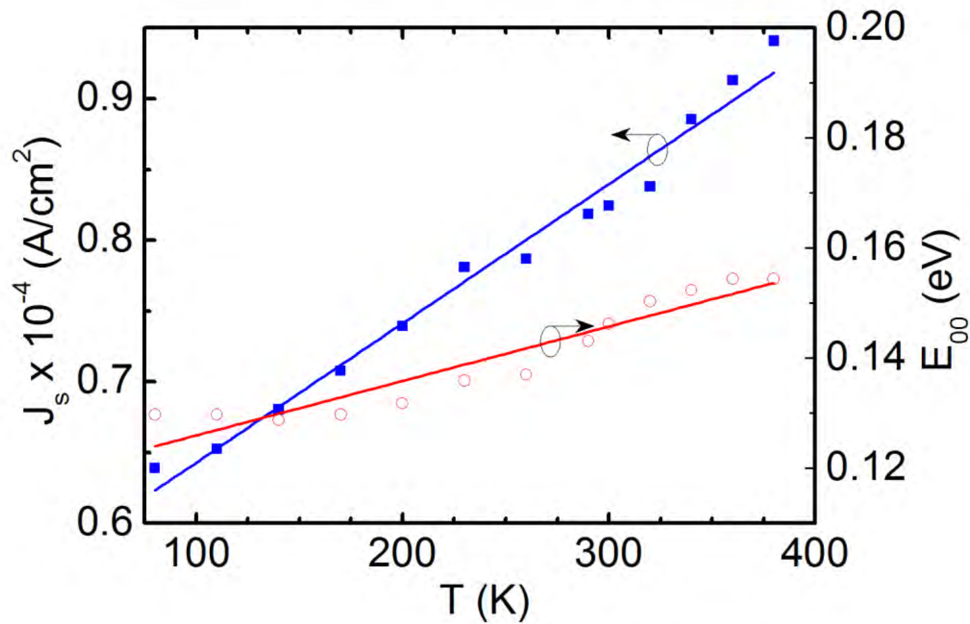

Figure 5.3: The temperature dependences of the tunneling saturation current density (J_{s_tunnel}) and the characteristic energy of tunneling (E_{00}) for (Ni/Au)-AlN/GaN SBDs.

It is evident that the saturation current shows weak temperature dependent behavior and the characteristic energy of tunneling shows temperature independent behavior in the temperature range 80– 380 K. The results indicate that in this temperature range, the mechanism of the charge transport is performed by tunneling along dislocations intersecting the space charge region in the (Ni/Au)– AlN/GaN Schottky barrier diode [117, 124, 125, 127].

The frequency-dependent capacitance and conductance were measured in a frequency range from 0.1 to 50 kHz in order to investigate the trapping effects in (Ni/Au)–AlN/GaN SBDs. The capacitance and conductance of the Schottky diode were measured simultaneously assuming a parallel combination of C and G. Figure 5.4a and b shows the typical C_m–V and G_m/ω–V characteristics of (Ni/Au)–AlN/GaN SBDs measured at 0.7, 1, 2, and 3 kHz, respectively. The measured C–V and G/ω–V plots shows both voltage and frequency dependent behaviors. In the accumulation regions for a given bias voltage, the C and G/ω decrease with increase in frequencies due to the frequency dependent response of interface states. At lower frequencies the interface states can follow the ac signal and yield a frequency dependent excess capacitance. In the high-frequency limit, however, the interface states cannot follow the alternating current (ac) signal. This makes the contribution of interface state capacitance to the total capacitance ignorable small [128, 129].

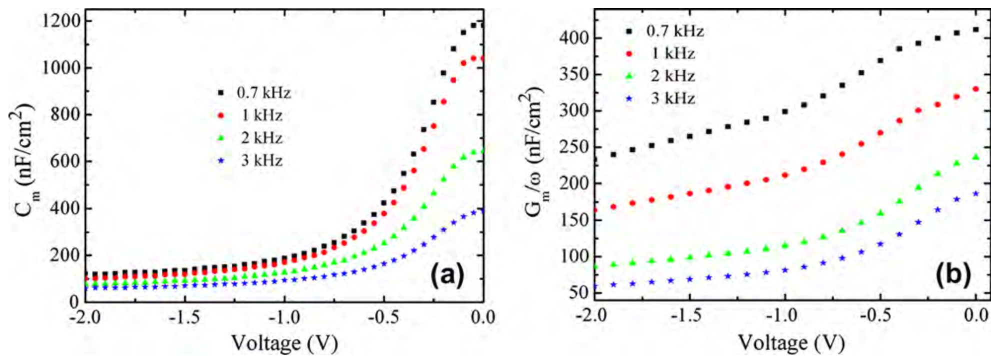

Figure 5.4: (a) Typical measured capacitance and (b) conductance data as a function of voltage for (Ni/Au)–AlN/GaN SBDs measured at 0.7, 1, 2, and 3 kHz.

The method described by Schroder for MOS capacitor analysis, which was adapted for the interface trap characterization of $Al_{0.15}Ga_{0.85}N$/GaN HFET structures by Miller *et al*. [130], was used in the interface trap investigation in (Ni/Au)–AlN/GaN SBDs [128-135]. There are four main possibilities to consider for the spatial location of traps in (Ni/Au)–AlN/GaN SBDs: (1) the metal–semiconductor interface of the Schottky contact, (2) the bulk of the barrier layer, (3) the interface between the barrier layer and the channel, and (4) the bulk of the channel layer [128, 130, 132, 134]. It is impossible to know

where the traps are located a priori; all four locations must be considered. Miller et al. used the various models that account for the presence of the traps that are located at the heterojunction, in the bulk of the barrier layer and at the metal–semiconductor interface [130]. They measured the density and time constant of the trap states, but they could not determine the location of the traps unambiguously. In this study, the analysis of the frequency dependent capacitance and conductance data was performed assuming models in which traps are present at the heterojunction-interface traps in our study.

The full circuit model in our analysis is shown in Fig. 5a, where Cb is the barrier capacitance (AlN layer), CGaN is the capacitance of the GaN depletion region capacitor, Rs is the series resistance of the ohmic contact, and Cit and Rit are the interface trap capacitance and associated loss term for the traps. The full circuit in Fig. 5a can be shown by the simplified circuit of Fig. 5b. The capacitance and conductance of the Schottky barrier diode were measured simultaneously assuming a parallel combination of C and G, as shown in Fig. 5c.

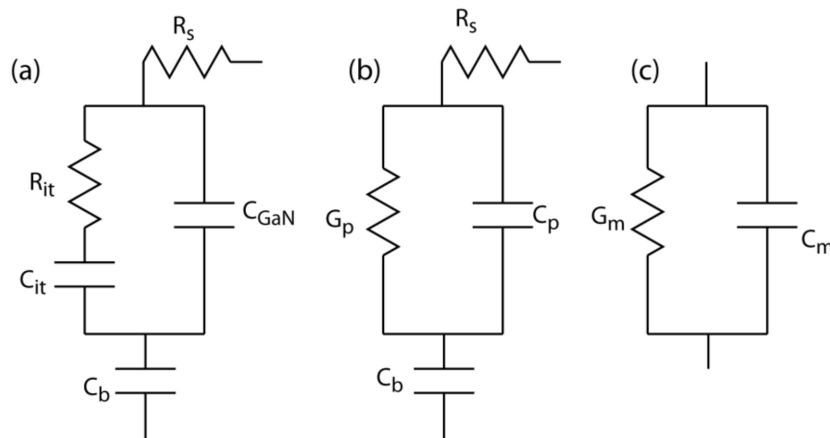

Figure 5.5: Equivalent circuit model of (Ni/Au)–AlN/GaN SBDs used to extract trap parameters from the experimental measurements. (a) The measurement circuit, (b) the assumed model with interface traps states and (c) converted to the simplified circuit.

The parallel conductance G_p/ω can be obtained from the measured C_m and G_m/ω curves by using the relation [129-131, 133],

$$\frac{G_p}{\omega} = \frac{-\omega C_b^2(R_s C_m^2 \omega^2 + R_s G_m^2 - G_m)}{\omega^4 C_m^2 C_b^2 R_s^2 + \omega^2(C_b^2 R_s^2 G_m^2 + C_m^2 + C_b^2 - 2C_b^2 R_s G_m - 2C_m C_b) + G_m^2} \quad (5.4)$$

In the equation, the barrier capacitance C_b was taken as the C_{AlN} capacitance values. In addition, R_s is the series resistance. The C_b value was determined from the plateau in the C–V curves that are associated with the accumulation of electrons in the two dimensional electron gas channel. The C_b values used as 1600 nF/cm^2 were measured at 0.1 kHz. R_s and were calculated from the forward bias I–V characteristics in room temperature by fitting the tunneling current expression (Equation (5.2)) to the experimental data (Table 5.1). The G_p/ω as functions of frequency, by assuming a continuum of trap levels, can be expressed as [130, 134],

$$\frac{G_p}{\omega} = \frac{qD_t}{2\omega\tau_t} ln(1 + \omega^2\tau_t^2) \quad (5.5)$$

Fig. 6 shows the calculated Gp/ω–$ln(\omega)$ curves of the AlN/GaN heterostructures for a different bias voltage. G_p/ω versus $ln(\omega)$ gives a peak for each bias voltage value due to the D_t contribution.

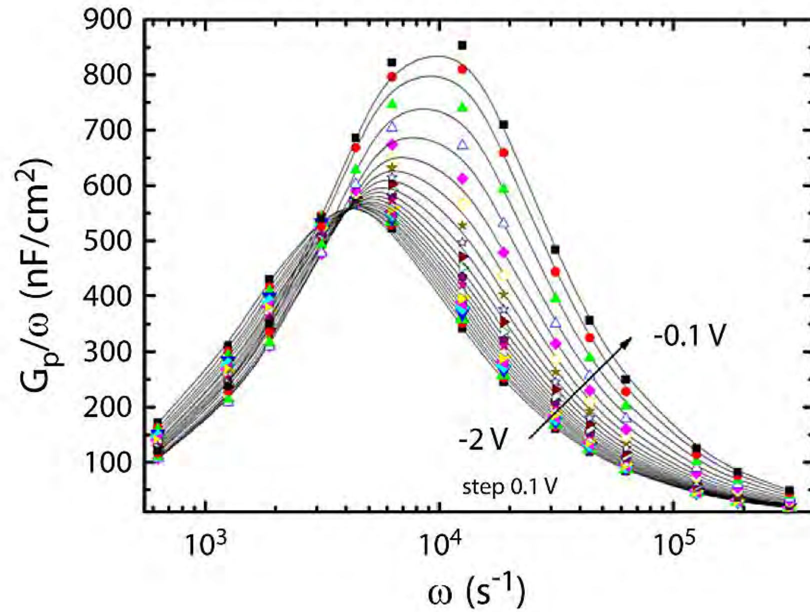

Figure 5.6: Parallel conductance as a function of frequency for (Ni/Au)–AlN/GaN SBDs at different bias voltage values. The solid curves are the best fit of equation (5.5) to the experimental data.

The D_t and η_t were calculated by fitting equation (5.5) to the experimental G_p/ω versus $ln(\omega)$ curves. By use of the appropriate technique, each value of applied bias voltage is converted into a surface potential corresponding to the Fermi level position within the band gap that we are probing [129, 136]. This procedure was applied for several values of bias voltage.

Fig. 7 shows the extracted D_t and η_t as a function of energy separation from the conduction-band edge (E_c - E_t). The resulting calculated parameters of the AlN/GaN HEMTs were D_t≈(5-8)×10^{12} eV^{-1} cm^{-2} and η_t≈(43-102) µs for the interface trap states, respectively.

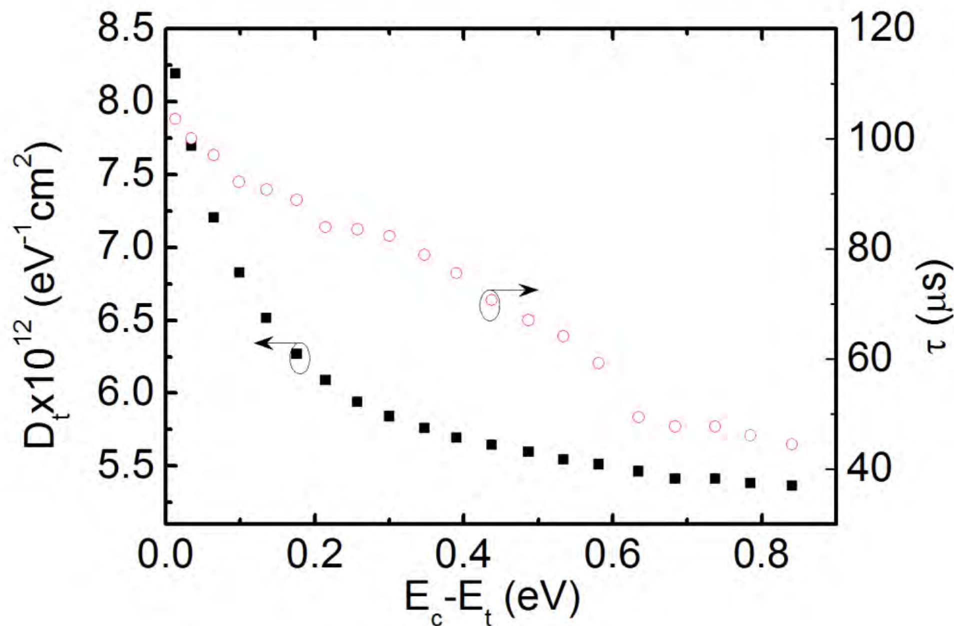

Figure 5.7: Experimentally derived density (D_t) and time constants (τ_t) of the trap statesas a function of energy separation from the conduction-band edge (E_c - E_t). for (Ni/Au)–AlN/GaN SBDs.

Kordoš *et al.* [20] investigated the trapping effects in an Al_2O_3/AlGaN/GaN metal–oxide–semiconductor heterostructure field effect transistor by temperature dependent conductance measurements. They identified two dominant trap states time constant as 1 µs and 10 ms and trap state density of the order of 10^{12} eV^{-1} cm^{-2}. On the other hand, Wu et al. [135] published a study on the electrical characterization of Al_2O_3/GaN interfaces by photo-

assisted capacitance–voltage characterization. They report the average interface trap density D_{it} of (1–2) × 10^{12} eV^{-1} cm^{-2}. In this study, our measured trap state density and time constant (D_t≈(5-8)×$10^{12}$$eV^{-1}$ cm^{-2} and η_t≈(43-102) µs are consistent with the reported results for the GaN based structures.

5.1.3 Conclusions

The mechanism of charge transport in the (Ni/Au)–AlN/GaN Schottky barrier diodes were investigated by the use of current– voltage characteristics in the temperature range of 80–380 K. The true current transport mechanisms for (Ni/Au)–AlN/GaN SBDs were determined by fitting the analytical expressions given for the current transport mechanisms to the experimental J–V data in a wide range of applied biases and at different temperatures, by taking the J_{s_tunnel}, E_0, and R_s as adjustable fit parameters. Fitting results show the weak temperature dependent behavior in the saturation current and the temperature independent behavior of the tunneling parameters in this temperature range. Therefore, it has been concluded that the mechanism of charge transport in (Ni/Au)–AlN/GaN SBDs, along the dislocations intersecting the space charge region, is performed by tunneling. Furthermore, in order to investigate the trapping effects in AlN/GaN heterostructures, the frequency dependent (C–V) and (G/ω–V) measurements were done in the frequency range 0.7–50 kHz. A detailed analysis of the frequency-dependent capacitance and conductance data was performed, assuming the models in which traps are located at the heterojunction interface. The density (D_t) and time constants (η_t) of the trap states have been determined as a function of energy separation from the conduction-band edge (E_c - E_t) as D_t≈(5-8)×$10^{12}$$eV^{-1}$ cm^{-2} and η_t≈(43-102) µs, respectively.

5.2 Electrical characterization of MS and MIS structures on AlGaN/AlN/GaN heterostructures

This section was published as "*Electrical characterization of MS and MIS structures on AlGaN/AlN/GaN heterostructures*" Engin Arslan, Serkan Bütün, Yasemin Safak, Habibe Uslu, Ilke Tasçıoglu, Semsettin Altındal and Ekmel Özbay Microelectronics Reliability, volume 51, page 370 (2011) Reproduced (or 'Reproduced in part') with permission from Elsevier Ltd. © 2011 Elsevier Ltd.

The forward and reverse bias I–V, C–V, and G/ω–V characteristics of (Ni/Au) Schottky barrier diodes (SBDs) on the $Al_{0.22}Ga_{0.78}N$/AlN/GaN high-electron-mobility-transistor (HEMTs) without and with SiN_x insulator layer were measured at room temperature in order to investigate the effects of the insulator layer (SiN_x) on the main electrical parameters such as the ideality factor (n), zero-bias barrier height (ϕ_{B0}), series resistance (R_s), interface-state density (N_{ss}). The energy density distribution profile of the N_{ss} were obtained from the forward bias I–V characteristics by taking into account the voltage dependence of the effective barrier height (ϕ_e) and ideality factor (n_V) of devices. In addition, the N_{ss} as a function of E_c–E_{ss} was determined from the low-high frequency capacitance methods. It was found that the values of N_{ss} and R_s in SBD HEMTs decreases with increasing insulator layer thickness.

5.2.1 Introduction

$Al_xGa_{1-x}N$/GaN heterostructures have attracted much regard for their important applications for high-speed, high-power, and high- temperature electronic devices [9, 137, 138]. One of the important problems of the nitride-based high-power microwave electronics is the presence of trapping centers resulting from deep defects and/or impurities in the materials. This trapping centers leads to high leakage current. The relatively slow charging and

discharging of these defect states, with time constants in the microseconds range, cause $Al_xGa_{1-x}N$/GaN HEMTs to experience RF dispersion and leakage current [1–5]. In order to reduce RF dispersion and leakage current the AlGaN surface can be passivated with dielectric materials. The most commonly reported one is the SiN_x deposited by PECVD [139, 140]. Various passivation materials have been reported to control surface states and decrease a leakage current of AlGaN/GaN HEMTs [141, 142]. The fundamental requirements for the materials are high dielectric constant [137, 139-151]. The interface quality between the deposited metal and the semiconductor surface decides the performance and reliability of these devices. Therefore, in order to reduce the leakage current and interface-state density, a variety of gate oxides/insulators such as Al_2O_3 [137, 141, 142], ZrO_2 [144], SiN_x [139, 140, 148], $SrTiO_3$ [150], $Bi_3Ti_4O_{12}$ [151], HfO_2 [149], and SiO_xN_y [147] materials have been proposed for application as an insulator layer at the metal/semiconductor (M/S) interface in semiconductor devices such as a metal–insulator–semiconductor (MIS) or metal–oxide–semi-conductor (MOS), metal–ferroelectric–semiconductor (MFS) or metal - ferroelectric - insulator - semiconductor (MFIS), metal – oxide – semiconductor field effect transistor (MOSFET), MFISFET structures and high-electron-mobility-transistors (HEMTs) [137, 139-151].

The performance and reliability of Schottky gate AlGaN/GaN HEMTs are largely impaired by high gate leakage current [141] and the poor long-term reliability of the Schottky gate. Using a thin film between the metal and semiconductor, such as Si_3N_4, can not only prevent the reaction and inter-diffusion between the metal and AlGaN barrier layer, but can also further improve the retention properties [145, 148]. In addition, the various non-idealities, such as the formation of an insulator layer at the M/S interface, the energy distribution profile of N_{ss} at the semiconductor/insulator (S/I) interface, R_s and inhomogeneous Schottky barrier heights (SBHs) all affect the electrical characteristics of MIS and HEMT structures.

The quality and the thickness of the insulator layer between metal and semiconductor are important parameters that affect the main electrical parameters [143, 144, 152-154]. In general, the forward bias I–V characteristics are linear in the semi-logarithmic scale at intermediate bias voltages (~0.1–0.8 V), but deviate from the linearity due to the effect of R_s when the applied-bias voltage is sufficiently large (V > 0.8 V) [72, 140, 148, 152-154]. Since a bias voltage is applied across these structures, the combination of the insulator layer, depletion layer, and series resistance of the device will share the applied bias voltage. Therefore, the high values of the ideality factor of these structures can be explained by means of the effects of the bias voltage drop across the insulator layer, surface states, bias dependence of the barrier height (BH), and barrier inhomogeneity at the M/S interface. The first studies on the insulator layer at the M/S interface were conducted by Cowley and Sze [155], who obtained their estimations from an analysis of the Schottky barrier heights (SBHs) with different metallization as a function of the metal work function. Already, some studies [72, 144, 148, 156] inspected the effect of existence of an insulator/oxide layer and the N_{ss} on the behavior of SBDs, and extracted the density distribution of N_{ss} in the semiconductor band gap from the forward bias I–V characteristics.

The aim of the present study is to compare some of the main electrical parameters of SBD HEMTs and MIS HEMTs by using I– V, C–V, and G/ω–V measurements at room temperature. In order to determine the energy density distribution of the N_{ss} was obtained from the forward bias I–V characteristics by taking into account the bias dependence of the effective BH (ϕ_e) and n_V, as well as low–high frequency C–V characteristics. In addition, the values of Rs of these structures were determined from forward bias I–V by using Cheung's functions.

5.2.2 Fabrication an Results

The $Al_{0.22}Ga_{0.78}N$/AlN/GaN heterostructures on c-plane (0001) double side polished 2-in. diameter sapphire substrate in a low-pressure metalorganic chemical-vapor deposition (MOCVD) reactor (Aixtron 200/4 HT-S) by using

trimethylgallium (TMGa), trimethylaluminum (TMAl), and ammonia as Ga, Al, and N precursors, respectively. Prior to the epitaxial growth, substrate was annealed at 1100 °C for 10 min in order to remove surface contam- ination. The buffer structures consisted of a 15 nm thick, low-temperature (650 °C) AlN nucleation layer along with high temperature (1150 °C) 420 nm AlN templates. A 1.6 µm nominally undoped (ud) GaN layer was grown on an AlN template layer at 1050 °C, which was followed by a 2 nm thick high temperature undoped AlN (1150 °C) barrier layer. After the deposition of these layers, a 23 nm thick undoped $Al_{0.22}Ga_{0.78}N$ layer was grown at 1050 °C. Finally, a 5 nm thick undoped GaN cap layer growth was carried out at a temperature of 1085 °C. Epitaxial structure of the wafer used in this study is summarized on table 5.4.

The grown wafer was cut into several pieces and the ohmic and Schottky/rectifier contacts were made atop the sample in the high vacuum coating system at approx. 10^{-7} Torr. For the Hall effect measurements by the Van Der Pauw method, square shaped (5 x 5 mm^2) samples were prepared with four evaporated triangular in the corners and the Schottky contacts were formed as 1 mm diameter circular dots The details of the fabrication steps and methods were described in appendix A. Ti/Al/Ni/Au (16/180/50/150 nm) metals were evaporated on the sample by e-beam and were annealed at 850 °C for 30 s in N_2 ambient in order to form the ohmic contact.

Table 5.2: The summary of the epitaxial structure of the $Al_{0.22}Ga_{0.78}N$ wafer.

Layer	Thickness (nm)
GaN	5
$Al_{0.22}Ga_{0.78}N$	23
AlN	2
GaN	1600
AlN	420
AlN	15
Sapphire	Substrate

After the formation of the ohmic contact, the SiN_x layer was deposited by plasma enhanced chemical vapor deposition (PECVD) on $Al_{0.22}Ga_{0.78}N/AlN/GaN$ heterostructures at 300 °C. The SiN_x growth was optimized to have a low growth rate without changing the refractive index by a series of growth and ellipsometric measurements. After growth rate optimization, we achieved growth rate of about 10 nm/min with an index of refraction of 2.02. Thereafter SiN_x layers of thickness 5.5 nm and 11 nm were deposited on samples B and C, respectively. We were able to measure the SiN_x thickness exactly with ellipsometer. Sample A, however, did not have any passivation layer. Finally, 1 mm diameter Schottky contact areas were defined by Ni/Au (50/80 nm) evaporation using a hard mask.

The current–voltage (I–V) measurements were performed by the use of a Keithley 2400 Source Meter. The capacitance voltage (C–V) and conductance voltage (G/ω–V) measurements were performed at 1 MHz by using HP 4192A LF impedance analyzer (5 Hz–13 MHz). All measurements were carried out at room temperature in the Janes vpf-475 cryostat and with the help of a micro-computer through an IEEE-488 AC/DC converter card. The surface morphology was characterized by atomic force microscope (AFM).

Figure 5.8 shows AFM image of the surface of the SBD HEMTs and MIS HEMTs. The AFM image (5×5 μm^2) of the surface shows wavy surface with root mean square (rms) roughness of 0.33, 1.27 and 1.33 nm for sample A, sample B and sample C, respectively. The rms value of the surface roughness was increased with increasing SiN_x layer thickness. The forward and reverse bias current–voltage (I–V) characteristics of the (Ni/Au) Schottky barrier diodes on the $Al_{0.22}Ga_{0.78}N/AlN/$ GaN heterostructures without and with SiN_x insulator layer were investigated at room temperature. Figure 5.9 compares the forward and reverse bias semi-logarithmic I–V characteristics of two MIS HEMTs with 5.5 nm and 11 nm SiN_x insulator layer and SBD HEMTs samples. The results confirm a significant reduction in leakage current of about four orders of magnitude for the MIS HEMTs, with 11 nm SiN_x insulator layer, in comparison

to the SBD HEMTs. It is noted that in the positive bias region is also considerably reduced by SiN_x insulator layers. Also the SiN_x insulator is effective in suppressing not only the leakage current but also in enhancing the forward turn-on voltage. Therefore growing a high quality SiN_x layer as the insulator will suppress the leakage current to a large extent and possibly shift the device threshold voltage [148].

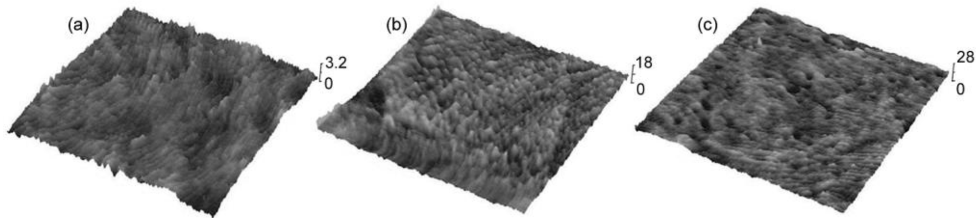

Figure 5.8: AFM surface topography images of the SBD HEMTs (a) without, (b) with 5.5 nm and (c) 11 nm SiN_x. (Scan area was 5 × 5 µm^2 and z-scale is in nm)

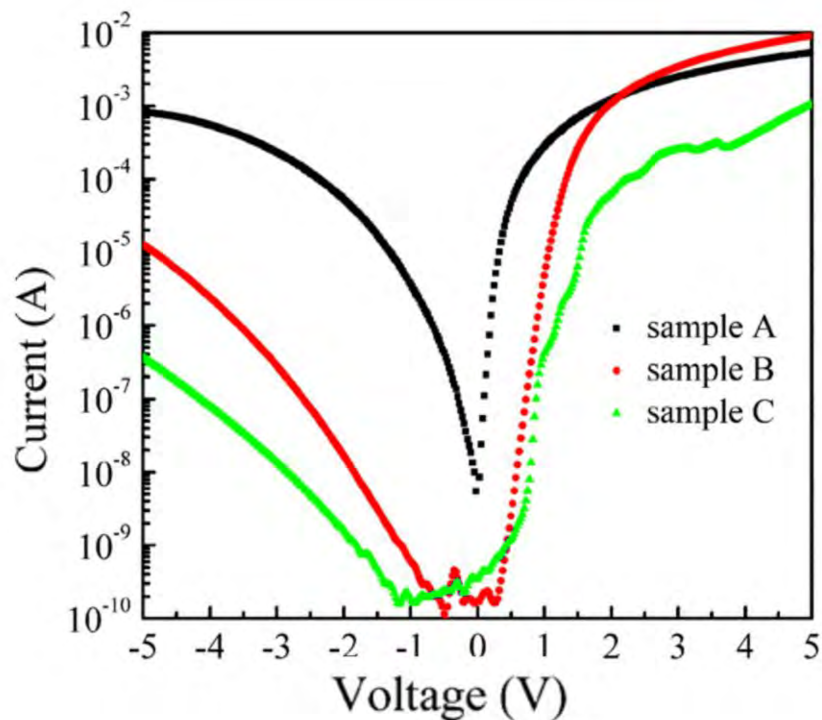

Figure 5.9: Forward and reverse bias semi-logarithmic I-V characteristics of SBD HEMT and MIS HEMTs.

In general, the relationship between the applied-bias voltage ($V \geq 3$ kT/q) and the current through a barrier between the metal and semiconductor of the MS, MIS, and solar cells, with series resistance, is given by [72]

$$I = \left\{AA^{*}T^{2}e^{-\frac{q\phi_{B0}}{kT}}\right\}.e^{\frac{q(V-IR_{S})}{nkT}-1} \tag{5.6}$$

where ϕ_{B0} is the zero-bias barrier height, A is the rectifier contact area, A^{*} is the effective Richardson constant and is equal to 32.09 A/cm^{2}K^2 for undoped $Al_{0.22}Ga_{0.78}N$ [143], in which I_0 (the term in curly brackets) is the reverse saturation current derived from the straight line intercept of *ln* I at zero bias voltage [72]. The term IR_s is the voltage drop across the series resistance of the diode. The voltage $V_d = V–IR_s$ across the diode can be expressed in terms of the total voltage drop, V, across the series combination of the diode and the series resistance. In equation (5.6), n is the ideality factor, T is the absolute temperature in Kelvin, k is the Boltzmann constant, V is the applied voltage across the structure. The value of n can be derived from the slope of *ln I* vs V plot [72, 153, 156]. Each *ln I–V* curve consists of a linear range with different slopes. The n values for SBD HEMTs (sample A) and MIS HEMTs (sample B and sample C) were obtained as 1.5, 2.5 and 4.0, respectively. It is clear that the n values of the heterostructure are larger than unity and its values increases with increasing insulator layer thickness (Table 5.3). These values of the ideality factors show that the structures follow an MIS configuration rather than MS SBDs [146, 153, 154, 156, 157]. Such behavior of n can especially be attributed to the existence of an insulator layer, a wide distribution of low BH patches, a tunneling mechanism, and the particular distribution of N_{ss} at the M/S interface [72, 129, 143, 144, 152-158]. In general, the semiconductor surface is inevitably covered with a native thin insulator layer if the semiconductor surface is prepared by the usual polishing and chemical etching, in which the evaporation of metal is carried out in a conventional vacuum system [156, 159-161]. For a sufficiently thick interface insulator layer, the interface states are in equilibrium

with the semiconductor, and they cannot interact with the metal [72, 153, 156, 160, 161].

Table 5.3: The passivation layer thickness dependent values of parameters determined from I-V characteristics of SBD HEMTs and MIS HEMTs.

Sample	n	I_0 (A)	Φ_{B0} (eV)	R_s ($dV/dln(I)$) (Ω)	R_s ($H(I)$) (Ω)
A	1.52	6.86×10^{-9}	0.73	665	653
B	2.54	1.03×10^{-12}	0.95	310	290
C	4.05	1.06×10^{-11}	0.89	383	352

The value of the saturation current I_0 was obtained by extrapolating the linear intermediate bias voltage region of the curve to zero applied-bias voltage, in which the zero bias BH (ϕ_{B0}) value was calculated from equation (5.6) for each sample and is shown in table 5.4. The downward curvature at sufficiently high bias voltages was caused by the effect of R_s, apart from the existence of the interface states [72, 153, 158]. While the R_s, is significant especially in the downward curvature of the forward bias I–V characteristics, the N_{ss} is effective in the inversion and depletion regions, and their distribution profile changes from region to region in the band gap. For these reason, in this small linear region, the accuracy of the determination of the barrier height and n becomes poorer. Therefore, n, BH, and R_s were evaluated by using a method that was developed by Cheung and Cheung functions [158] in the high current range.

Equation (5.6) can be rearranged as the following expressions [158].

$$V = IR_s + n\phi_{B0} + \frac{nkT}{q} \ln \frac{I}{AA^*T^2} \tag{5.7}$$

$$\frac{dV}{d(lnI)} = n\frac{kT}{q} + IR_s \tag{5.8}$$

defining a new function $H(I)$ to evaluate ϕ_{B0},

$$H(I) = V - \frac{nkT}{q} ln \frac{I}{AA^{*}T^{2}} = IR_{s} + n\phi_{B0} \quad (5.9)$$

where ϕ_{B0} is the barrier height obtained from the data of the downward curvature region in the forward bias I–V characteristics. Figure 5.10a and b show the experimental *dV/d(ln I)* vs. *I* and *H(I)* vs. *I* plots for all the samples obtained from the forward bias I–V data, respectively. *dV/d(ln I)* vs. *I* gives a straight line for the data of the downward curvature region in the forward bias I–V. Thus, the slope in figure 5.10a will give R_s and *nkT/q* as the y-axis intercept. Furthermore, from the Cheung and Cheung functions plot the *n* and R_s values that were obtained for all the samples at room temperature. In addition, the slope of *H(I)* (Figure 5.10b) along with the *n* found from figure 5.10a gives a second R_s which will be used to check the consistency of the approach whereas the intercept gives ϕ_{B0}. Thus, for all the samples and by performing different plots (Equation (5.7)) of the I–V data, the values of R_s were obtained and shown in table 5.3. As shown in Table 1, the *n* values obtained from equation (5.6) and the average R_s obtained from both equation (5.7) values by different techniques are in good agreement with each other. The series resistance differences between the samples can arise from some different sources: (1) the contact made by the probe wire to the gate (2) the ohmic to the AlGaN/AlN/GaN HEMT surface (3) difference in the thickness of SiN_x layer [129].

The voltage dependent ideality factor nV can be written from equation (5.6) as:

$$n_{V} = \frac{qV}{kTln(I/I_{0})} \quad (5.10)$$

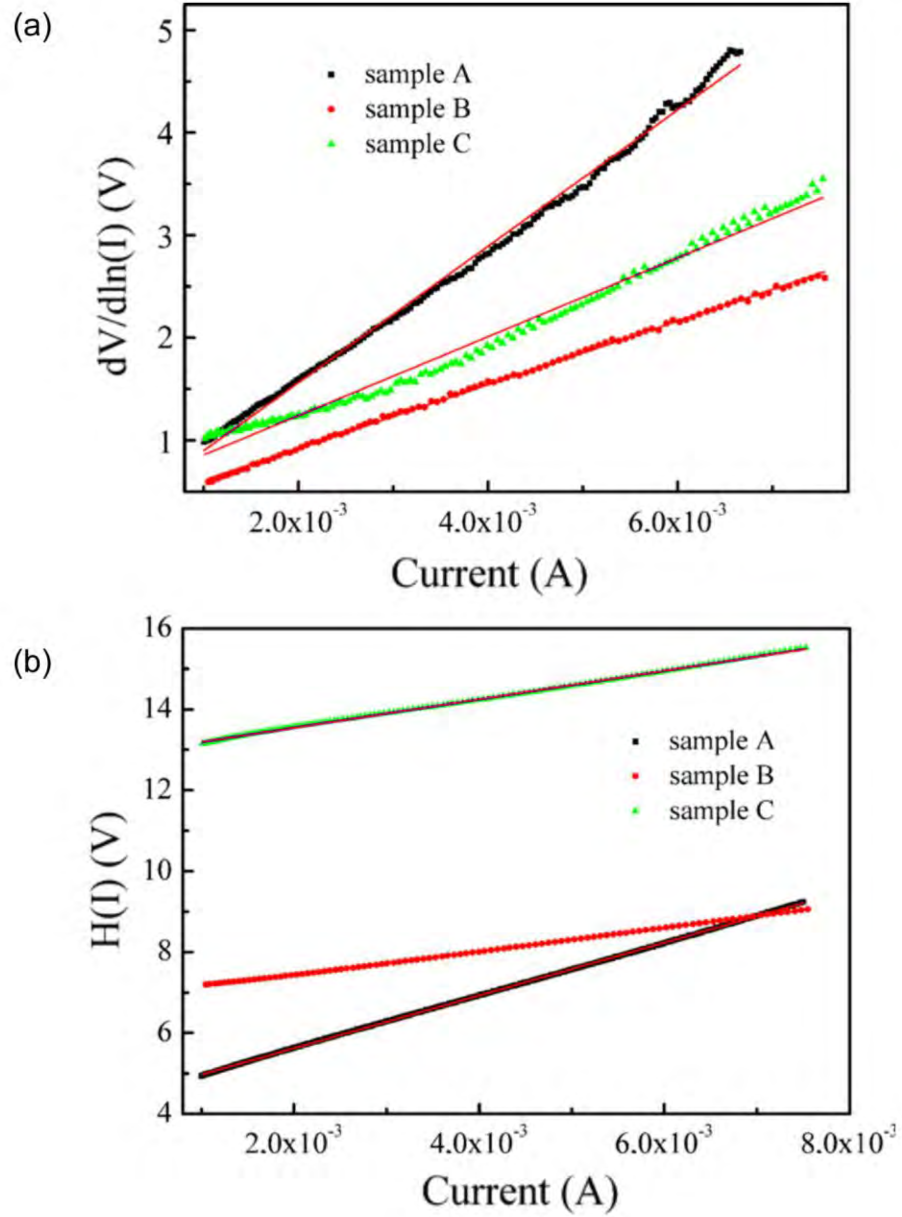

Figure 5.10: The I-V analysis of the SBDs. (a) *dV/d(lnI)* vs. *I* and (b) *H(I)* vs. *I* obtained from the equations (5.6) through (5.9).

In addition, the voltage dependence of the effective barrier height, ϕ_e is contained in the ideality factor, n, through the relation [156, 157, 160-162] as

$$\phi_e = \phi_{B0} + \frac{qV}{kT} = \phi_{B0} + V\frac{d\phi_e}{dV} \quad (5.11)$$

where $d\phi_e/dV$ is the change in the barrier with bias voltage. For the metal–insulator–semiconductor (MIS) diode having interface states that are in equilibrium with the semiconductor, the ideality factor n becomes greater than unity. As proposed by Card and Rhoderick [156], it is given by

$$n = \frac{q}{kT}\frac{dV}{d\ln I} = \frac{1}{1 - {d\phi_{B0}}/{dV}} \quad (5.12)$$

Equation (5.6) is often used to evaluate the I–V characteristics. However, this does not include the effects of the applied voltage on the barrier height. If $d\phi_e/dV$ is constant, the ideality factor n should be constant, but the ideality factor n obtained in equation (5.11) deviates from the experimental results. Furthermore, the following expression can be used for the ideality factor [153],

$$n = 1 + \frac{\frac{\delta}{\varepsilon_i}\left(\frac{\varepsilon_s}{W} + qN_{sb}\right)}{1 + \frac{\delta}{\varepsilon_i} q^2 N_{sa}} \quad (5.13)$$

where N_{sb}, N_{sa} are the densities of the interface states that are in equilibrium with the metal and semiconductor, respectively. ε_s and ε_i are the permittivity of semiconductor and insulator layer, respectively. For the MIS type Schottky diodes, the interface states that are entirely governed by the semiconductor, the expression for the density of the interface states as deduced by Card and Rhoderick [156] can be reduced as

$$N_{ss} = \frac{1}{q}\left(\frac{\varepsilon_i}{\delta}(n-1) - \frac{\delta}{W}\right) \quad (5.14)$$

where δ is the thickness of the insulator layer, and W is the depletion layer width that is being determined from the experimental C–V measurements at a sufficiently high frequency ($f > 1$ MHz). Here, the values of ε_i and ε_s used as 7.5 ε_0 and 8.9 ε_0 for SiN_x layer and AlGaN, respectively [163].

The energy of interface states E_{ss} with respect to the conductance band edge is given by [129, 143, 152-158, 160]

$$E_C - E_{ss} = q(\phi_e - V) \quad (5.15)$$

The energy density distribution profile of the interface states N_{ss} for (Ni/Au) SBDs on AlGaN/AlN/GaN heterostructures without and with SiN_x insulator layer were obtained from the experimental forward bias I–V and are shown in figure 5.11. For all samples there was a slight exponential increase in N_{ss} from the nearly mid-gap towards the bottom of the conductance band. In this case, while the donor type N_{ss} is in effect near the conductance band, the acceptor type N_{ss} is in effect near the valance band. It is obvious that the values of N_{ss} decrease with the increase of the insulator layer thickness.

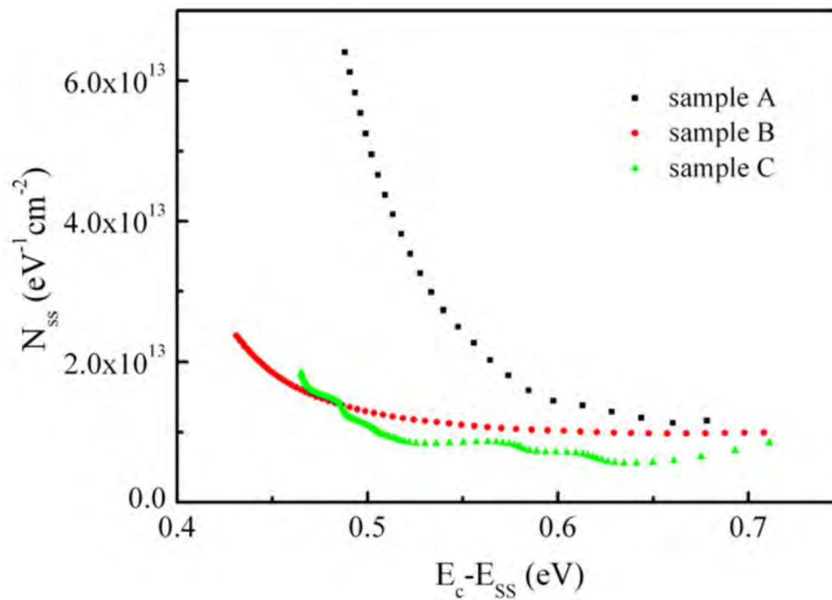

Figure 5.11: Density of interface states N_{ss} as a function of E_c-E_{ss} deduced from the I-V measurements of the SBD HEMT and MIS HEMTs.

Moreover, the densities of the interface states for sample A are in equilibrium with the metal, and the other samples (sample B and sample C) are in equilibrium with the semi-conductor due to a sufficiently large insulator layer thickness.

Figure 5.12a and b show the C–V and G/ω–V measurements at 1 MHz and at room temperature for the (Ni/Au) SBDs on $Al_{0.22}Ga_{0.78}N$/ AlN/GaN heterostructures without and with SiN_x insulator layer. At sufficiently high frequencies (f > 1 MHz), the N_{ss} cannot follow the (ac) signal, because at high

frequencies the carrier life time (η) is larger than the measured period [129]. Therefore, the C–V and G/ω–V measurements were performed at 1 MHz. As can be seen in figure 5.12a, the C–V characteristics of the sample A, sample B and sample C exhibit inversion, depletion and accumulation regions. However, the behavior of the C–V curves is different for each region for each sample. The C–V characteristic of sample A shows two peaks in the inversion and accumulation region at about -8.3 V and -0.6 V, respectively. The first peak can be attributed to the interface states localized at M/S interface. However, the second peak can be explained with the effect of the R_s [129, 164, 165] It is well known; the interface states are effective for the inversion and depletion region. On the other hand, series resistance of device is effective only in accumulation region or at sufficiently forward bias region [129, 164, 165]. In the recent studies, the existence of capacitance peak in the C–V plot is confirmed by the number of experimental results on MIS-Schottky barrier devices [164, 165]. It has been shown that, in the presence of series resistance, the capacitance–voltage should exhibit a peak. The peak value of the capacitance depends on a number of parameters such as doping concentration, interface-state density and the thickness of the insulator layer [164-166].Werner et al. [166], on the other hand, made a systematic investigation on several Schottky barrier devices with both ohmic and non-ohmic back contacts an correlated this anomalous variation in capacitance to non-ohmic back contact.

The density distribution profile of N_{ss} was also obtained from the low–high frequency capacitance measurements, as seen in the following equation [129]

$$N_{SS} = \frac{1}{qA}\left[\left(\frac{1}{C_{LF}} - \frac{1}{C_i}\right)^{-1} - \left(\frac{1}{C_{HF}} - \frac{1}{C_i}\right)^{-1}\right] \quad (5.16)$$

where C_{LF} and C_{HF} are the measurement low frequency capacitance (5 kHz) and high frequency capacitance (1 MHz), respectively, and C_i is the insulator layer capacitance. The capacitance of insulator layer (C_i) is calculated, from the accumulation capacitance, to be 327 nF/cm^2, 283 nF/cm^2 and 194 nF/cm^2 for

samples A, B and C, respectively. For sample A native oxide layer taken as insulator layer. It is well known that, unless specially fabricated, a Schottky barrier diode possesses a thin interfacial native oxide layer between the metal and semiconductor. The existence of such an insulating layer can have a strong influence on the diode characteristics. Consequently, there are several possible reasons of errors that cause deviation of the ideal behavior of with and without an insulator layer Schottky diodes and must be taken into account. These include the effects of insulator layer between metal and semiconductor, interface states (N_{ss}), series resistance (R_s), and formation of barrier height at MS interface. Also, in the presence of a series resistance, the C–V characteristics should exhibit a peak. The peak value of capacitance is found to vary with series resistance, interface-state density, and frequency of the ac signal [164, 165]. The series resistance is an important parameter, which causes the electrical characteristics of MS and MIS-Schottky diodes to be non-ideal [72, 146, 147, 149-151]

The advantage of this method comes from the fact that it enables the determination of the many properties of the insulator layer. In this method [129], the N_{ss} is extracted from its capacitance contribution to the measured experimental C–V curve. In the equivalent circuit of MIS type diodes, the C_i is in series with the parallel combination of the interface state capacitance and the space charge capacitance. At sufficiently high frequencies (f > 1 MHz), the interface states cannot respond to the ac excitation, so that they do not contribute to the total capacitance directly. Figure 5.13 shows the density distribution profile of N_{ss}, which was obtained for all the samples. As can be seen in figure 5.13, the values of Nss decrease with the increase of the insulator layer thickness.

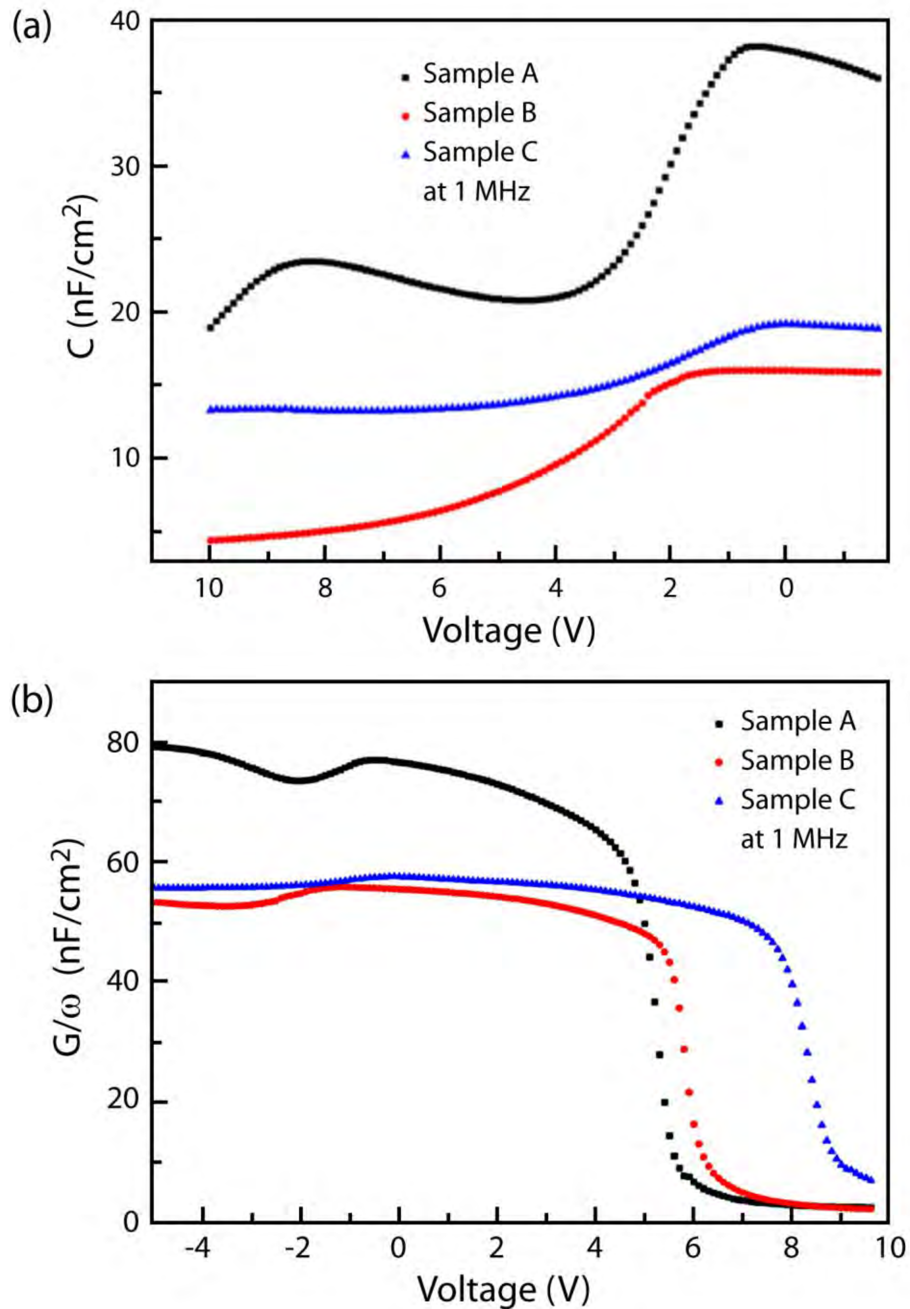

Figure 5.12: The measured (a) C–V and (b) G/ω–V characteristics of SBD HEMTs and MIS HEMTs measured at 1 MHz

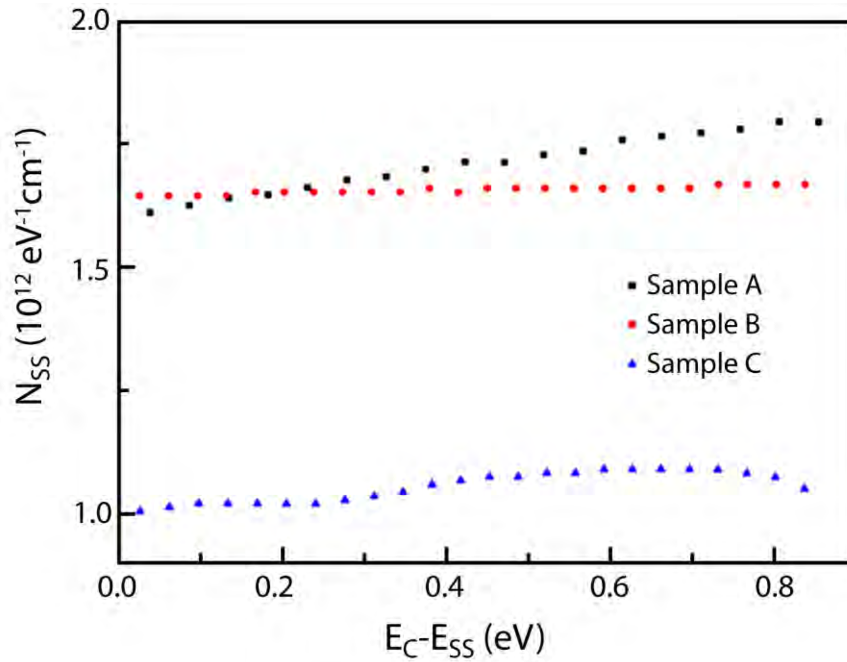

Figure 5.13: Density of interface states N_{ss} as a function of E_c–E_{ss} deduced from the low–high frequency C–V data for SBD HEMTs and MIS HEMTs

5.2.3 Conclusions

In summary, the forward and reverse bias I–V, C–V, and G/ω–V characteristics of the SBDs on $Al_{0.22}Ga_{0.78}N$/AlN/GaN heterostructures without and with SiN_x insulator layer were measured in order to investigate the effects of the insulator layer on the main electrical parameters such as the ideality factor (n), zero-bias barrier height (ϕ_{B0}), series resistance (R_s) and interface-state density (N_{ss}) at room temperature. The experimental results show that the values of the insulator layer thickness and R_s were found to strongly affect the function of the main electrical parameters. The values of R_s of these structures were obtained from Cheung's and conductance methods by using forward bias I–V characteristics. The energy distribution profile of N_{ss} was obtained from the forward bias I–V characteristics, by taking into account the bias dependence of the ϕ_e and n_V, as well as the low–high frequency C–V characteristics. It is obvious that the determined values of N_{ss} from I–V and low–high frequency capacitance methods decrease with the increase of the insulator layer thickness.

5.3 Leakage current investigation of Ni/Au Schottky contacts on GaN based heterostructures

This section was published as "Leakage current by Frenkel–Poole emission in Ni/Au Schottky contacts on $Al_{0.83}In_{0.17}N$/AlN/GaN heterostructures" Engin Arslan, Serkan Bütün, and Ekmel Özbay Applied Physics Letters, volume 94, 142106 (2009) Reproduced (or 'Reproduced in part') with permission from American Institute of Physics. © 2009 American Institute of Physics.

We performed the temperature-dependent IV characterization of Schottky contacts on $Al_{0.83}In_{0.17}N$/AlN/GaN heterostructures in order to determine the reverse-bias leakage current mechanisms in the temperature range of 250–375 K. The leakage current was found to be in agreement with the Frenkel–Poole emission model in this temperature range. The analysis of the reverse current-voltage characteristics is clearly stated that the main process in leakage current is the emission of electrons from a trapped state near the metal-semiconductor interface into a continuum of states which associated with each conductive dislocation.

5.3.1 Introduction

The AlInN/GaN material system has gained major interest for its electronic applications [167, 168] in the last decade because of its promising electronic properties, polarization effects, and high thermal stability. The main advantage of $Al_{1-x}In_xN$ alloy is that; it is lattice matched to GaN at an indium content of approximately 17%. This minimizes strain, and thereby it also minimizes cracking and/or dislocation formation at the lattice-matched $Al_{0.83}In_{0.17}N$/GaN interface. Hence, AlInN materials have a great potential for GaN-based optoelectronics. However, a high excess leakage current of the reverse-biased Schottky contact is reported as the most crutial problem for realization of high quality devices [168]. A number of investigations have been

carried out for the basic mechanisms of gate leakage current, [169-175] and leakage current reduction [176]. Zhang et al. [175] analyzed the leakage current mechanisms in the Schottky contacts of both n-GaN and AlGaN/GaN at different temperatures and concluded that tunneling current dominates at temperatures below 150 K, whereas the Frenkel–Poole emission dominates at temperatures higher than 250 K. Miller et al. [173] have shown that the reverse-bias leakage in AlGaN/GaN can be analyzed in a conventional tunneling model. The effects of the dislocations and defects states, in the reverse-bias leakage, have been suggested by several studies for GaN and $Al_xGa_{1-x}N$ heterostructures [169, 170, 175] wherein defects, in particular dislocations, might play an important role in reverse-bias leakage. [169, 173, 175] However, to date, no investigation has been made to analyze the leakage current of the mechanisms of Schottky contacts on $Al_{1-x}In_xN$/AlN/GaN heterostructures.

In this chapter we show the results of our investigation on reverse leakage current through Ni/Au Schottky contacts on $Al_{1-x}In_xN$/AlN/GaN heterostructures over a temperature range of 250 to 375 K.

5.3.2 Fabrication and Results

The $Al_{0.83}In_{0.17}N$/AlN/GaN heterostructure was grown on a c-plane sapphire substrate in a MOCVD reactor. The growth was started with 15 nm thick nucleation layer of AlN at 840 °C after the cleaning process. An AlN buffer layer (BL) was grown at 1150 °C following the nucleation. The thickness of the BL was 520 nm. Another BL of about 2 µm thick undoped GaN was grown at 1070 °C. A second nucleation layer with 2 nm thickness was grown prior the AlInN layer at 1040 °C. The growth was finalized by deposition of 20 nm thick AlInN layer at 800 °C. The layer structure of the wafer is summarized in table 5.4. The composition of the AlInN layer was quantified by high resolution x-ray diffraction [127].

Table 5.4 The summary of the epitaxial structure of the $Al_{0.83}In_{0.17}N$ wafer.

Layer	Thickness (nm)
$Al_{0.83}In_{0.17}N$	20
AlN	2
GaN	2000
AlN	520
AlN	15
Sapphire	substrate

The wafer was cut in 7 × 7 mm^2 pieces. We fabricated ohmic contact in a Van Der Pauw (VDP) geometry by evaporating Ti/Al/Ni/Au (35/200/50/150 nm) using a hard mask. Then samples were annealed at 850˚C in N_2 ambient in order the make alloying. Subsequently, 1 mm diameter Ni/Au (40/50 nm) Schottky contacts were evaporated in the middle of the surface. (Figure 5.14)

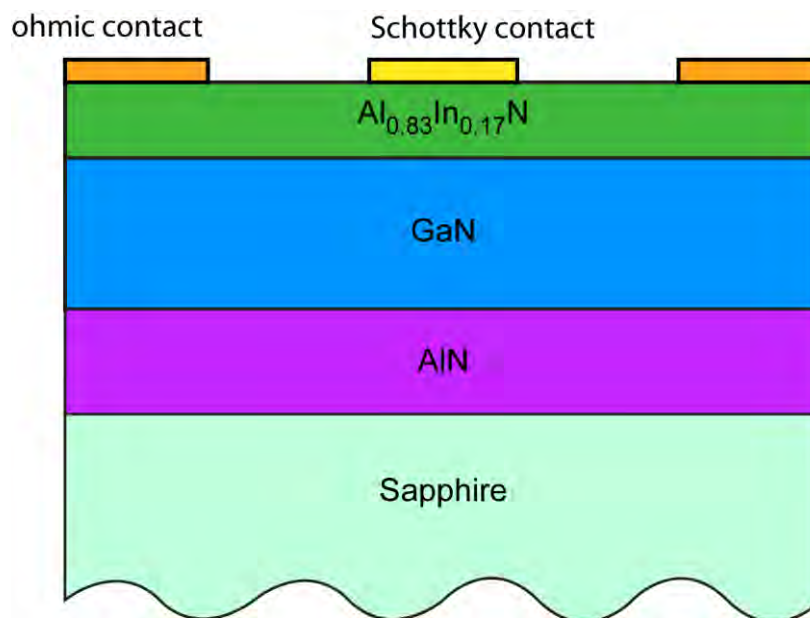

Figure 5.14: Schematic presentation of the fabricated AlInN device used for the leakage current investigation.

The room temperature Hall mobility and the carrier density were measured as 812 cm^2/Vs and 4.2×10^{13} cm^{-2}, respectively by VDP method.

Temperature dependent IV measurements were carried out using HP4145B Semiconductor Parameter Analyser in a closed-cycle He cryostat. The temperature was monitored by Cu-constantan thermocouple with sensitivity of 0.1K. Figure 5.15 represents the IV measurements of the fabricated sample in the range of 250 K to 375 K. The leakage current tends to increase with the increasing temperature as expected mainly because of thermionic effects.

Frenkel–Poole emission refers to electric-field-enhanced thermal emission from a trapped state into a continuum of electronic states, in which usually, but not necessarily, the conduction band in an insulator. The current density associated with Frenkel–Poole emission is given by [169, 170, 172-177]

$$J = C \cdot E_b \cdot e^{-\frac{q\cdot(\phi_b - \sqrt{q\cdot E_b/\pi\cdot\varepsilon_0\cdot\varepsilon_s})}{k_B\cdot T}} \qquad (5.17)$$

where E_b is the electric field in the semiconductor barrier at the metal-semiconductor interface and is calculated assuming that it is constant within the $Al_{1-x}In_xN$ barrier layer, ϕ_b is the barrier height for electron emission from the trapped state, ε_s is the relative dielectric permittivity at high frequency, T is the temperature, ε_0 is the permittivity of free space, k_B is Boltzmann's constant and C is a constant.

Equation (5.17) can be rewritten as

$$\ln\left(\frac{J}{E_b}\right) = f_1(T)\cdot\sqrt{E_b} + f_2(T) \qquad (5.18)$$

$$f_1(T) = \frac{q}{kT}\sqrt{\frac{q}{\pi\varepsilon_0\varepsilon_s}} \qquad (5.19)$$

$$f_2(T) = -\frac{q\phi_b}{kT} + logC \qquad (5.20)$$

That is, in the current transport by Frenkel–Poole emission, $ln(J/E_b)$ should be a linear function of $(E_b)^{0.5}$ for a given temperature. The actual Current-Electric field dependence is well described with equation (5.18) indeed (Figure 5.16).

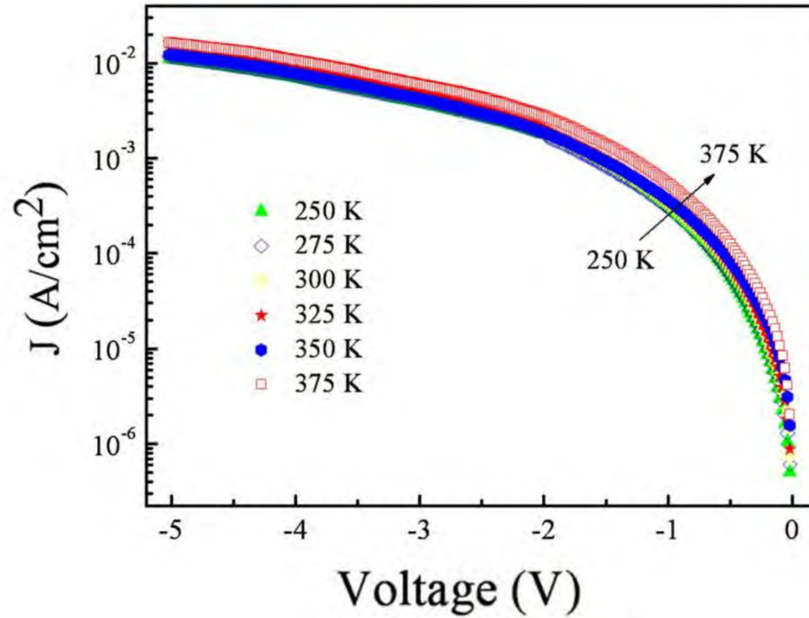

Figure 5.15: Temperature dependent IV characteristics of Ni/Au Schottky contacts on AlInN.

The temperature dependence of the slope and intercept functions f_1 and f_2 as a function of $1/T$ are given in figure 5.17. We have calculated the relative dielectric permittivity (ε_s) and the barrier height (ϕ_b) as 5.8 and 0.12 eV, respectively form the slopes of the linear fits. Given that the dielectric permittivity of GaN and InN as 5.35 and 5.8 respectively [163] ; our calculated value is in good agreement with the reported values. This further supports the validity of the Frankel-Poole emission model for describing the current transport mechanism in AlInN Schottky contacts.

5.3.3 Conclusion

The leakage current transport mechanism across the Schottky contacts on $Al_{0.83}In_{0.17}N$/AlN/GaN heterostructures was determined by using temperature dependent reverse-bias current-voltage characteristics in the temperature range of 250 to 375 K. In this temperature range, reverse-bias leakage current is dominated by Frenkel–Poole emission

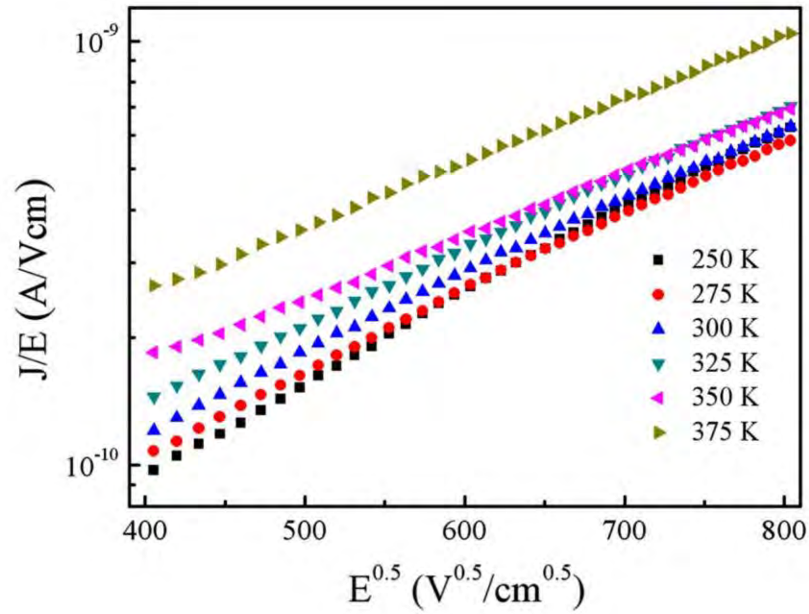

Figure 5.16: Measured reverse-bias current density divided by electric field vs. square root of electric field.

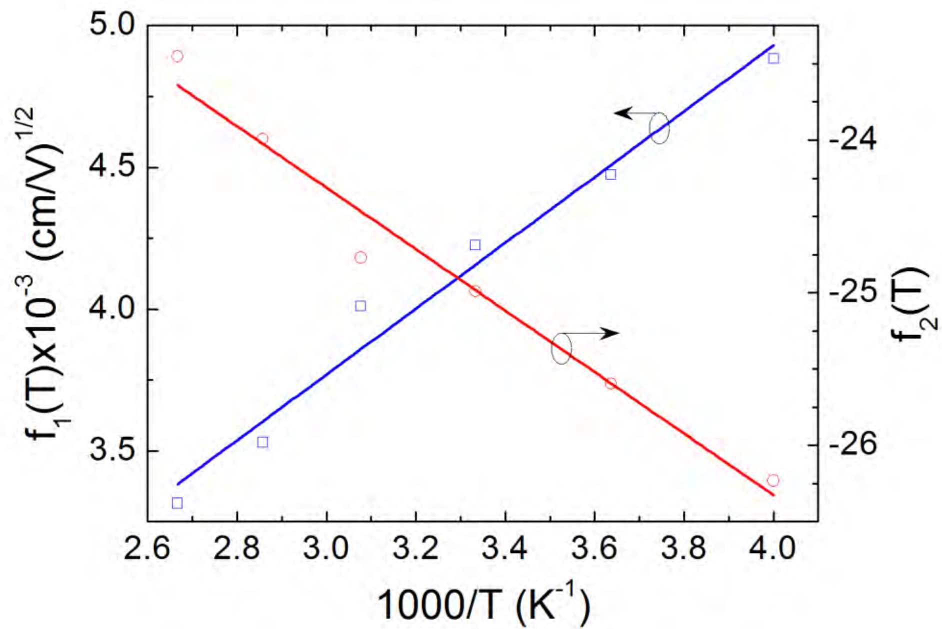

Figure 5.17: Temperature dependence of the slope and intercept functions f_1 and f_2 as a function of $1/T$.

.

Chapter 6
Conclusion

We have presented our work on AlGaN/GaN based heterostructures in this thesis. All of the epitaxial materials were grown in a metalorganic chemical vapor deposition technique. We grow eight different structures in total. We have fabricated photodetectors on five of them and the rest was used for leakage current investigations.

We have developed a novel architecture for multicolor sensing photodetectors in UV. We have successfully demonstrated dual and four color sensing on monolithically integrated photodetectors. Color separation was accomplished by epitaxially grown AlGaN layers with changing Al content on a single structure. Devices were back illuminated.

Dual color photodetector exhibited two distinct bands with peak responses 0.12 A/W at 310 nm with 10 V bias and 0.10 A/W at 254 nm with 25 V bias. The FWHM of the longer and shorter bands were 11 and 22 nm respectively. Both band rejected each other by more than 3 orders of magnitude. Device exhibited superior dark current characteristics with no more than 1 pA up to 180.

We have fabricated two four-color sensing photodetector with different epitaxial structure. The first structure had four distinct 1 μm thick AlGaN layers. Each layer acted as both active absorber for its own band and a passive filter for longer bands. Peak responsivity wavelengths were at 328, 309, 290 and 267 nm and the FWHMs were 18, 17, 22 and 9 nm, from longer to shorter bands. The second structure had eight distinct 1/2 μm thick AlGaN layers. Four of them were active layers whereas the remaining four were the filter layers. Peak responsivity wavelengths were at 336, 316, 295 and 268 nm and the FWHMs

were 8, 12, 11 and 8 nm, from longer to shorter bands. Both of the devices have shown reasonable IV characteristics with less than 10 pA at 100 V bias. As a result, extra filter layers improved the separation of the bands.

The suggested and demonstrated multicolor sensitive devices in this thesis significantly increase the functionality of photodetectors in UV. They can be used as wavelength sensors without any dispersive optics like gratings or prisms. The idea is expandable to visible region with epitaxial growth of InGaN films with changing In content. This way the entire spectrum from 200 nm to 1300 nm can be covered which will open enormous possibilities from solar cells to sensing technologies.

We have expanded our work to the plasmonics. Al nano-particles were fabricated on sapphire for measurements of the extinction spectrum by e-beam lithography. We have confirmed the resonance in the UV region. For a particle diameter of 36 nm the resonance was obtained around 300 nm. We confirmed measurements with FDTD simulations. We have fabricated these Al nano-particles on top of the GaN photodetectors. The compared spectral responsivity measurements revealed 1.5 fold enhancement around 339 nm. This was the first ever utilization of LSPR in UV to date. It had rather high importance because this experimentally demonstrated the plasmonic enhancement in UV which completes the picture from IR to UV through visible.

As a second approach towards to the sub-wavelength photodetectors we have worked on nano-structure decorated MSM contacts separated by sub-wavelength slits. This approach reduces the device size dramatically. We have fabricated linear gratings with 300 nm period on each side of the MSM contacts. Optimization of the gratings was done with ellipsometric measurements and both analytical and computational calculations. Grating coupled sub-wavelength photodetectors exhibited eight-fold enhancement in the photocurrent. These measurements were confirmed with a laser excitation. We have performed FDTD simulations to understand the physical mechanism behind this enhancement. We have found that surface bound leaky waves and SPPs are

definitely playing a role in this picture. We have also concluded that SPPs are enhancing and shifting the peak resonance.

We have investigated the leakage current mechanism in Schottky barriers on various AlGaN/GaN based devices. It was clear that dominant mechanism is the tunneling current in these structures. This can be attributed to the high background doping level of as grown structures. In addition we have showed that by inserting a thin layer of insulator under the Schottky metal; the surface state density can be reduced, thereby increasing the device performance.

Bibliography

1. Needham, J. and L.U. GWEI-DJEN, *Science and civilisation in china: Physics and physical technology*. 1962: Cambridge University Press.
2. Hett, W.S., *Aristotle: Problems. Books i-xxi*. 1936: Heinemann.
3. Daniel, M. *Daguerre (1787–1851) and the invention of photography*. 2000 October 2004; Available from: http://www.metmuseum.org/toah/hd/dagu/hd_dagu.htm.
4. Hertz, H., Wied. Ann., 1887. **xxxi** p. 983.
5. Iams, H. and B. Salzberg, *The secondary emission phototube.* Proceedings of the Institute of Radio Engineers, 1935. **23**(1) p. 55-64.
6. Diffey, B.L., *Sources and measurement of ultraviolet radiation.* Methods, 2002. **28**(1) p. 4-13.
7. Monroy, E., F. Omnes, and F. Calle, *Wide-bandgap semiconductor ultraviolet photodetectors.* Semiconductor Science and Technology, 2003. **18**(4) p. R33-R51.
8. Morkoc, H., et al., *Large-band-gap sic, iii-v nitride, and ii-vi znsn-based semiconductor-device technologies.* Journal of Applied Physics, 1994. **76**(3) p. 1363-1398.
9. Mohammad, S.N., A.A. Salvador, and H. Morkoc, *Emerging gallium nitride based devices.* Proceedings of the Ieee, 1995. **83**(10) p. 1306-1355.
10. Razeghi, M. and A. Rogalski, *Semiconductor ultraviolet detectors.* Journal of Applied Physics, 1996. **79**(10) p. 7433-7473.
11. Shur, M. and A. Žukauskas, *Uv solid-state light emitters and detectors*. 2004: Kluwer Academic Publishers.
12. Lim, B.W., et al., *High responsitivity intrinsic photoconductors based on al[sub x]ga[sub 1 - x]n.* Applied Physics Letters, 1996. **68**(26) p. 3761-3762.
13. Walker, D., et al., *Algan ultraviolet photoconductors grown on sapphire.* Applied Physics Letters, 1996. **68**(15) p. 2100-2101.
14. Osinsky, A., et al., *Schottky barrier photodetectors based on algan.* Applied Physics Letters, 1998. **72**(6) p. 742-744.
15. Tut, T., et al., *High bandwidth-efficiency solar-blind algan schottky photodiodes with low dark current.* Solid-State Electronics, 2005. **49**(1) p. 117-122.

16. Chowdhury, U., et al., *High-performance solar-blind photodetector using an al0.6ga0.4n n-type window layer.* Journal of Crystal Growth, 2003. **248**(0) p. 552-555.

17. Collins, C.J., et al., *Improved solar-blind detectivity using an al[sub x]ga[sub 1 - x]n heterojunction p--i--n photodiode.* Applied Physics Letters, 2002. **80**(20) p. 3754-3756.

18. Wong, M.M., et al., *High quantum efficiency algan/gan solar-blind photodetectors grown by metalorganic chemical vapor deposition.* physica status solidi (a), 2001. **188**(1) p. 333-336.

19. Butun, S., et al., *Low dark current metal-semiconductor-metal photodiodes based on semi-insulating gan.* Applied Physics Letters, 2006. **89**(7) p. 073503.

20. Butun, S., et al., *Deep-ultraviolet al0.75ga0.25n photodiodes with low cutoff wavelength.* Applied Physics Letters, 2006. **88**(12) p. 123503.

21. Chen, C.H., et al., *Gan metal-semiconductor-metal ultraviolet photodetectors with transparent indium-tin-oxide schottky contacts.* Ieee Photonics Technology Letters, 2001. **13**(8) p. 848-850.

22. Li, J., et al., *200 nm deep ultraviolet photodetectors based on aln.* Applied Physics Letters, 2006. **89**(21) p. 213510.

23. Ozbay, E., et al., *High-performance solar-blind photodectors based on al(x)ga(1-x)n heterostructures.* Ieee Journal of Selected Topics in Quantum Electronics, 2004. **10**(4) p. 742-751.

24. Pau, J.L., et al., *Algan ultraviolet photodetectors grown by molecular beam epitaxy on si(111) substrates.* Materials Science and Engineering B-Solid State Materials for Advanced Technology, 2002. **93**(1-3) p. 159-162.

25. Razeghi, M., *Short-wavelength solar-blind detectors - status, prospects, and markets.* Proceedings of the Ieee, 2002. **90**(6) p. 1006-1014.

26. Su, Y.K., et al., *Nitride-based msm uv photodetectors with photo-chemical annealing schottky contacts.* Solid-State Electronics, 2005. **49**(3) p. 459-463.

27. Walker, D., et al., *High-speed, low-noise metal-semiconductor-metal ultraviolet photodetectors based on gan.* Applied Physics Letters, 1999. **74**(5) p. 762-764.

28. Goodman, J.W., et al., *Optical interconnections for vlsi systems.* Proceedings of the Ieee, 1984. **72**(7) p. 850-866.

29. Krishnamoorthy, A.V. and D.A.B. Miller, *Scaling optoelectronic-vlsi circuits into the 21st century: A technology roadmap.* Ieee Journal of Selected Topics in Quantum Electronics, 1996. **2**(1) p. 55-76.

30. Meindl, J.D., et al., *Interconnect opportunities for gigascale integration.* Ibm Journal of Research and Development, 2002. **46**(2-3) p. 245-263.

31. Miller, D.A.B., *Rationale and challenges for optical interconnects to electronic chips.* Proceedings of the Ieee, 2000. **88**(6) p. 728-749.

32. Ozbay, E., *Plasmonics: Merging photonics and electronics at nanoscale dimensions.* Science, 2006. **311**(5758) p. 189-193.

33. Raether, H., *Surface plasmons on smooth and rough surfaces and on gratings*. 1988: Springer.

34. Garcia-Vidal, F.J., et al., *Light passing through subwavelength apertures.* Reviews of Modern Physics, 2010. **82**(1) p. 729-787.

35. Genet, C. and T.W. Ebbesen, *Light in tiny holes.* Nature, 2007. **445**(7123) p. 39-46.

36. Lopez-Tejeira, F., et al., *Efficient unidirectional nanoslit couplers for surface plasmons.* Nature Physics, 2007. **3**(5) p. 324-328.

37. Pang, Y., C. Genet, and T.W. Ebbesen, *Optical transmission through subwavelength slit apertures in metallic films.* Optics Communications, 2007. **280**(1) p. 10-15.

38. Popov, E., et al., *Field enhancement in single subwavelength apertures.* Journal of the Optical Society of America a-Optics Image Science and Vision, 2006. **23**(9) p. 2342-2348.

39. Przybilla, F., C. Genet, and T.W. Ebbesen, *Enhanced transmission through penrose subwavelength hole arrays.* Applied Physics Letters, 2006. **89**(12) p. 121115.

40. Akbari, A. and P. Berini, *Schottky contact surface-plasmon detector integrated with an asymmetric metal stripe waveguide.* Applied Physics Letters, 2009. **95**(2) p. 021104.

41. Akbari, A., R.N. Tait, and P. Berini, *Surface plasmon waveguide schottky detector.* Opt. Express, 2010. **18**(8) p. 8505-8514.

42. Cao, L.Y., et al., *Resonant germanium nanoantenna photodetectors.* Nano Letters, 2010. **10**(4) p. 1229-1233.

43. Collin, S., et al., *Efficient light absorption in metal--semiconductor--metal nanostructures.* Applied Physics Letters, 2004. **85**(2) p. 194-196.

44. Hetterich, J., et al., *Optimized design of plasmonic msm photodetector.* Quantum Electronics, IEEE Journal of, 2007. **43**(10) p. 855-859.

45. Ishi, T., et al., *Si nano-photodiode with a surface plasmon antenna.* Japanese Journal of Applied Physics, 2005. **44**(Copyright (C) 2005 The Japan Society of Applied Physics) p. L364.

46. Shackleford, J.A., et al., *Integrated plasmonic lens photodetector.* Applied Physics Letters, 2009. **94**(8) p. 083501.

47. Weiner, J., *The physics of light transmission through subwavelength apertures and aperture arrays.* Reports on Progress in Physics, 2009. **72**(6) p. 064401.

48. Willets, K.A. and R.P. Van Duyne, *Localized surface plasmon resonance spectroscopy and sensing.* Annual Review of Physical Chemistry, 2007. **58**(1) p. 267-297.

49. Hossain, M.K., et al., *Surface-enhanced raman scattering: Realization of localized surface plasmon resonance using unique substrates and methods.* Analytical and Bioanalytical Chemistry, 2009. **394**(7) p. 1747-1760.

50. Masson, J.F., M.P. Murray-Methot, and L.S. Live, *Nanohole arrays in chemical analysis: Manufacturing methods and applications.* Analyst, 2010. **135**(7) p. 1483-1489.

51. Pieczonka, N.P.W. and R.F. Aroca, *Single molecule analysis by surfaced-enhanced raman scattering.* Chemical Society Reviews, 2008. **37**(5) p. 946-954.

52. Willets, K.A. and R.P. Van Duyne, *Localized surface plasmon resonance spectroscopy and sensing*, in *Annual review of physical chemistry*. 2007. p. 267-297.

53. Anker, J.N., et al., *Biosensing with plasmonic nanosensors.* Nature Materials, 2008. **7**(6) p. 442-453.

54. Haes, A.J., et al., *Using solution-phase nanoparticles, surface-confined nanoparticle arrays and single nanoparticles as biological sensing platforms.* Journal of Fluorescence, 2004. **14**(4) p. 355-367.

55. Haes, A.J. and R.P. Van Duyne, *A unified view of propagating and localized surface plasmon resonance biosensors.* Analytical and Bioanalytical Chemistry, 2004. **379**(7-8) p. 920-930.

56. Hutter, E. and J.H. Fendler, *Exploitation of localized surface plasmon resonance.* Advanced Materials, 2004. **16**(19) p. 1685-1706.

57. Jain, P.K., et al., *Noble metals on the nanoscale: Optical and photothermal properties and some applications in imaging, sensing, biology, and medicine.* Accounts of Chemical Research, 2008. **41**(12) p. 1578-1586.

58. Mannelli, I. and M.P. Marco, *Recent advances in analytical and bioanalysis applications of noble metal nanorods.* Analytical and Bioanalytical Chemistry, 2010. **398**(6) p. 2451-2469.

59. Sepulveda, B., et al., *Lspr-based nanobiosensors.* Nano Today, 2009. **4**(3) p. 244-251.

60. Zhang, X.Y., et al., *Advances in contemporary nanosphere lithographic techniques.* Journal of Nanoscience and Nanotechnology, 2006. **6**(7) p. 1920-1934.

61. Zhao, J., et al., *Localized surface plasmon resonance biosensors.* Nanomedicine, 2006. **1**(2) p. 219-228.

62. Atwater, H.A. and A. Polman, *Plasmonics for improved photovoltaic devices.* Nature Materials, 2010. **9**(3) p. 205-213.

63. Catchpole, K.R. and A. Polman, *Plasmonic solar cells.* Optics Express, 2008. **16**(26) p. 21793-21800.

64. Catchpole, K.R. and A. Polman, *Design principles for particle plasmon enhanced solar cells.* Applied Physics Letters, 2008. **93**(19) p. 191113.

65. Derkacs, D., et al., *Improved performance of amorphous silicon solar cells via scattering from surface plasmon polaritons in nearby metallic nanoparticles.* Applied Physics Letters, 2006. **89**(9) p. 093103.

66. Ferry, V.E., et al., *Plasmonic nanostructure design for efficient light coupling into solar cells.* Nano Letters, 2008. **8**(12) p. 4391-4397.

67. Konstantatos, G. and E.H. Sargent, *Nanostructured materials for photon detection.* Nature Nanotechnology, 2010. **5**(6) p. 391-400.

68. Morfa, A.J., et al., *Plasmon-enhanced solar energy conversion in organic bulk heterojunction photovoltaics.* Applied Physics Letters, 2008. **92**(1) p. 013504.

69. Nakayama, K., K. Tanabe, and H.A. Atwater, *Plasmonic nanoparticle enhanced light absorption in gaas solar cells.* Applied Physics Letters, 2008. **93**(12) p. 121904.

70. Pillai, S., et al., *Surface plasmon enhanced silicon solar cells.* Journal of Applied Physics, 2007. **101**(9) p. 093105.

71. Westphalen, M., et al., *Metal cluster enhanced organic solar cells.* Solar Energy Materials and Solar Cells, 2000. **61**(1) p. 97-105.

72. Sze, S.M., *Physics of semiconductor devices*. 1981: Wiley.

73. Yeo, Y.C., T.C. Chong, and M.F. Li, *Electronic band structures and effective-mass parameters of wurtzite gan and inn.* Journal of Applied Physics, 1998. **83**(3) p. 1429-1436.

74. Lee, S.R., et al., *The band-gap bowing of al[sub x]ga[sub 1 - x]n alloys.* Applied Physics Letters, 1999. **74**(22) p. 3344-3346.

75. Singh, J., *Electronic and optoelectronic properties of semiconductor structures*. 2003: Cambridge University Press.

76. Brunner, D., et al., *Optical constants of epitaxial algan films and their temperature dependence.* Journal of Applied Physics, 1997. **82**(10) p. 5090-5096.

77. Wooten, F., *Optical properties of solids*. 1972: Academic Press.

78. Maier, S.A., *Plasmonics: Fundamentals and applications*. 2007: Springer.

79. Leveque, G. and O.J.F. Martin, *Optimization of finite diffraction gratings for the excitation of surface plasmons.* Journal of Applied Physics, 2006. **100**(12) p. 124301-6.

80. Kuwata, H., et al., *Resonant light scattering from metal nanoparticles: Practical analysis beyond rayleigh approximation.* Applied Physics Letters, 2003. **83**(22) p. 4625-4627.

81. Meier, M. and A. Wokaun, *Enhanced fields on large metal particles: Dynamic depolarization.* Opt. Lett., 1983. **8**(11) p. 581-583.

82. Buniatyan, V.V. and V.M. Aroutiounian, *Wide gap semiconductor microwave devices.* Journal of Physics D-Applied Physics, 2007. **40**(20) p. 6355-6385.

83. Khan, M.A., et al., *Iii-nitride uv devices.* Japanese Journal of Applied Physics Part 1-Regular Papers Brief Communications & Review Papers, 2005. **44**(10) p. 7191-7206.

84. Kung, P. and M. Razeghi, *Iii-nitride wide bandgap semiconductors: A survey of the current status and future trends of the material and device technology.* Opto-Electronics Review, 2000. **8**(3) p. 201-239.

85. Mokkapati, S. and C. Jagadish, *Iii-v compound sc for optoelectronic devices.* Materials Today, 2009. **12**(4) p. 22-32.

86. Morkoc, H., A. Di Carlo, and R. Cingolani, *Gan-based modulation doped fets and uv detectors.* Solid-State Electronics, 2002. **46**(2) p. 157-202.

87. Morkoc, H., et al., *Large-band-gap sic, iii-v nitride, and ii-vi znse-based semiconductor-device technologies.* Journal of Applied Physics, 1994. **76**(3) p. 1363-1398.

88. Biyikli, N., et al., *Solar-blind algan-based schottky photodiodes with low noise and high detectivity.* Applied Physics Letters, 2002. **81**(17) p. 3272-3274.

89. Biyikli, N., et al., *High-speed visible-blind gan-based indium-tin-oxide schottky photodiodes.* Applied Physics Letters, 2001. **79**(17) p. 2838-2840.

90. Biyikli, N., et al., *High-performance solar-blind algan schottky photodiodes.* Mrs Internet Journal of Nitride Semiconductor Research, 2003. **8**(2) p. 2.

91. Biyikli, N., et al., *Solar-blind algan-based p-i-n photodiodes with low dark current and high detectivity.* Ieee Photonics Technology Letters, 2004. **16**(7) p. 1718-1720.

92. Biyikli, N., et al., *Ito-schottky photodiodes for high-performance detection in the uv-ir spectrum.* Ieee Journal of Selected Topics in Quantum Electronics, 2004. **10**(4) p. 759-765.

93. Biyikli, N., et al., *High-speed solar-blind photodetectors with indium-tin-oxide schottky contacts.* Applied Physics Letters, 2003. **82**(14) p. 2344-2346.

94. Biyikli, N., et al., *High-speed characterization of solar-blind alxga1-n-x p-i-n photodiodes.* Semiconductor Science and Technology, 2004. **19**(11) p. 1259-1262.

95. Butun, B., et al., *High-performance visible-blind gan-based p-i-n photodetectors.* Applied Physics Letters, 2008. **92**(3) p. 033507.

96. Gokkavas, M., et al., *Algan-based high-performance metal-semiconductor-metal photodetectors.* Photonics and Nanostructures-Fundamentals and Applications, 2007. **5**(2-3) p. 53-62.

97. Tut, T., et al., *Solar-blind alxga1-xn-based avalanche photodiodes.* Applied Physics Letters, 2005. **87**(22) p. 223502.

98. Tut, T., et al., *Experimental evaluation of impact ionization coefficients in alxga1-xn based avalanche photodiodes.* Applied Physics Letters, 2006. **89**(18) p. 183524.

99. Tut, T., et al., *Solar-blind algan-based p-i-n photodetectors with high breakdown voltage and detectivity.* Applied Physics Letters, 2008. **92**(10) p. 103502.

100. Reine, M., et al., *Independently accessed back-to-back hgcdte photodiodes: A new dual-band infrared detector.* Journal of Electronic Materials, 1995. **24**(5) p. 669-679.

101. Onat, B.M., et al., *100-ghz resonant cavity enhanced schottky photodiodes.* Photonics Technology Letters, IEEE, 1998. **10**(5) p. 707-709.

102. Unlu, M.S., et al., *High bandwidth-efficiency resonant cavity enhanced schottky photodiodes for 800--850 nm wavelength operation.* Applied Physics Letters, 1998. **72**(21) p. 2727-2729.

103. Roy, S., S. Chaudhuri, and C.S. Unnikrishnan, *A simple and inexpensive electronic wavelength-meter using a dual-output photodiode.* American Journal of Physics, 2005. **73**(6) p. 571-573.

104. Degiron, A. and T. Ebbesen, *Analysis of the transmission process through single apertures surrounded by periodic corrugations.* Opt. Express, 2004. **12**(16) p. 3694-3700.

105. Tan, C.L., et al., *Absorption enhancement of 980 nm msm photodetector with a plasmonic grating structure.* Optics Communications, 2010. **283**(9) p. 1763-1767.

106. White, J.S., et al., *Extraordinary optical absorption through subwavelength slits.* Opt. Lett., 2009. **34**(5) p. 686-688.

107. Gan, Q.Q., et al., *Uv extraordinary optical transmission through nanoslits*, in *2009 ieee leos annual meeting conference proceedings, vols 1and 2*. 2009, Ieee: New York. p. 154-155.

108. Ekinci, Y., H.H. Solak, and C. David, *Extraordinary optical transmission in the ultraviolet region through aluminum hole arrays.* Optics Letters, 2007. **32**(2) p. 172-174.

109. Lin, J., et al., *Surface plasmon enhanced uv emission in algan/gan quantum well.* Applied Physics Letters, 2010. **97**(22) p. 221104.

110. Caglayan, H., I. Bulu, and E. Ozbay, *Extraordinary grating-coupled microwave transmission through a subwavelength annular aperture.* Optics Express, 2005. **13**(5) p. 1666-1671.

111. Hibbins, A.P., J.R. Sambles, and C.R. Lawrence, *Gratingless enhanced microwave transmission through a subwavelength aperture in a thick metal plate.* Applied Physics Letters, 2002. **81**(24) p. 4661-4663.

112. Lomakin, V. and E. Michielssen, *Enhanced transmission through metallic plates perforated by arrays of subwavelength holes and sandwiched between dielectric slabs.* Physical Review B, 2005. **71**(23) p. 235117.

113. Went, H.E., et al., *Selective transmission through very deep zero-order metallic gratings at microwave frequencies.* Applied Physics Letters, 2000. **77**(18) p. 2789-2791.

114. Yang, F.Z. and J.R. Sambles, *Resonant transmission of microwaves through a narrow metallic slit.* Physical Review Letters, 2002. **89**(6) p. 063901.

115. Yu, H., et al., *A study of semi-insulating gan grown on aln buffer/sapphire substrate by metalorganic chemical vapor deposition.* Journal of Crystal Growth, 2006. **293**(2) p. 273-277.

116. Palik, E.D., *Handbook of optical constants of solids*. 1985, New York: Academic Press Inc.

117. Arslan, E., et al., *Tunneling current via dislocations in schottky diodes on alinn/aln/gan heterostructures.* Semiconductor Science and Technology, 2009. **24**(7) p. 075003.

118. Kuzmik, J., et al., *Inain/gan hemts: A first insight into technological optimization.* Ieee Transactions on Electron Devices, 2006. **53**(3) p. 422-426.

119. Medjdoub, F., et al., Tech Dig-Int Electron Dev Meet, 2006 p. 1.

120. Cao, Y., et al., *Very low sheet resistance and shubnikov-de-haas oscillations in two-dimensional electron gases at ultrathin binary aln/gan heterojunctions.* Applied Physics Letters, 2008. **92**(15) p. 152112.

121. Elsass, C.R., et al., *High mobility two-dimensional electron gas in algan gan heterostructures grown by plasma-assisted molecular beam epitaxy.* Applied Physics Letters, 1999. **74**(23) p. 3528-3530.

122. Binari, S.C., et al., *Gan fets for microwave and high-temperature applications.* Solid-State Electronics, 1997. **41**(2) p. 177-180.

123. Alekseev, E., A. Eisenbach, and D. Pavlidis, *Low interface state density aln/gan misfets.* Electronics Letters, 1999. **35**(24) p. 2145-2146.

124. Evstropov, V.V., et al., *The dislocation origin and model of excess tunnel current in gap p-n structures.* Semiconductors, 2000. **34**(11) p. 1305-1310.

125. Belyaev, A.E., et al., *Mechanism of dislocation-governed charge transport in schottky diodes based on gallium nitride.* Semiconductors, 2008. **42**(6) p. 689-693.

126. Arslan, E., et al., *The influence of nitridation time on the structural properties of gan grown on si (111) substrate.* Applied Physics A: Materials Science & Processing, 2009. **94**(1) p. 73-82.

127. Arslan, E., et al., *Dislocation-governed current-transport mechanism in (ni/au)-algan/aln/gan heterostructures.* Journal of Applied Physics, 2009. **105**(2) p. 023705.

128. Chu, R.M., et al., *Admittance characterization and analysis of trap states in algan/gan heterostructures.* physica status solidi (c), 2003. **0**(7) p. 2400-2403.

129. Nicollian, E.H. and J.R. Brews, *Mos (metal oxide semiconductor) physics and technology*. 1982: Wiley.

130. Miller, E.J., et al., *Trap characterization by gate-drain conductance and capacitance dispersion studies of an algan/gan heterostructure field-effect transistor.* Journal of Applied Physics, 2000. **87**(11) p. 8070-8073.

131. Kolbesen, B.O., et al., *Analytical techniques for semiconductor materials and process characterization 6 (altech 2009)*. 2009: The Electrochemical Society.

132. Kordos, P., et al., *Trapping effects in al(2)o(3)/algan/gan metal-oxide-semiconductor heterostructure field-effect transistor investigated by temperature dependent conductance measurements.* Applied Physics Letters, 2010. **96**(1) p. 013505.

133. Nicollian, E.H.G., A., *The si-sio2 interface - electrical properties as determined by the metal-insulator-silicon conductance technique.* Bell System Technical Journal, 1967. **46** p. 1055.

134. Stoklas, R., et al., *Investigation of trapping effects in algan/gan/si field-effect transistors by frequency dependent capacitance and conductance analysis.* Applied Physics Letters, 2008. **93**(12) p. 124103.

135. Wu, Y.Q., et al., *Photo-assisted capacitance-voltage characterization of high-quality atomic-layer-deposited al2o3/gan metal-oxide-semiconductor structures.* Applied Physics Letters, 2007. **90**(14) p. 143504.

136. Shenoy, J.N., et al., *Characterization and optimization of the sio2/sic metal-oxide-semiconductor interface.* Journal of Electronic Materials, 1995. **24**(4) p. 303-309.

137. Hashizume, T., S. Ootomo, and H. Hasegawa, *Al2o3-based surface passivation and insulated gate structure for algan/gan hfets.* Phys. Stat. Sol. (C), 2003 p. 2380-2384.

138. Shen, L., et al., *Algan/aln/gan high-power microwave hemt.* Ieee Electron Device Letters, 2001. **22**(10) p. 457-459.

139. Fang, Z.Q., et al., *Traps in algan/gan/sic heterostructures studied by deep level transient spectroscopy.* Applied Physics Letters, 2005. **87**(18) p. 182115.

140. Higashiwaki, M., T. Mimura, and T. Matsui, *Gan-based fets using cat-cvd sin passivation for millimeter-wave applications.* Thin Solid Films, 2008. **516**(5) p. 548-552.

141. Feng, Q., Y. Hao, and Y.Z. Yue, *The reduction of gate leakage of algan/gan metal-insulator-semiconductor high electron mobility transistors by n(2) plasma pretreatment.* Semiconductor Science and Technology, 2009. **24**(2) p. 025030.

142. Pozzovivo, G., et al., *Gate insulation and drain current saturation mechanism in inaln/gan metal-oxide-semiconductor high-electron-mobility transistors.* Applied Physics Letters, 2007. **91**(4) p. 043509.

143. Arslan, E., S. Butun, and E. Ozbay, *Leakage current by frenkel-poole emission in ni/au schottky contacts on al(0.83)in(0.17)n/aln/gan heterostructures.* Applied Physics Letters, 2009. **94**(14) p. 142106.

144. Bera, M.K., et al., *High frequency characterization and continuum modeling of ultrathin high-k (zro2) gate dielectrics on strained-si.* Thin Solid Films, 2006. **504**(1-2) p. 183-187.

145. Bulbul, M.M., et al., *On the profile of temperature dependent series resistance in al/si3n4/p-si (mis) schottky diodes.* Microelectronic Engineering, 2006. **83**(3) p. 577-581.

146. Castagné, R. and A. Vapaille, *Description of the sio2si interface properties by means of very low frequency mos capacitance measurements.* Surface Science, 1971. **28**(1) p. 157-193.

147. Desmaris, V., et al., *Influence of oxynitride (sioxny) passivation on the microwave performance of algan/gan hemts.* Solid-State Electronics, 2008. **52**(5) p. 632-636.

148. Gaffey, B., et al., *High-quality oxide/nitride/oxide gate insulator for gan mis structures.* Ieee Transactions on Electron Devices, 2001. **48**(3) p. 458-464.

149. Liu, C., E.F. Chor, and L.S. Tan, *Enhanced device performance of algan/gan hemts using hfo2 high-k dielectric for surface passivation and gate oxide.* Semiconductor Science and Technology, 2007. **22**(5) p. 522-527.

150. Liu, C.Y. and T.Y. Tseng, *Correlation between deep depletion and current-voltage saturation of srtio3 gate dielectric capacitor.* Ceramics International, 2004. **30**(7) p. 1101-1106.

151. Park, B.H., et al., *Imprint failures and asymmetric electrical properties induced by thermal processes in epitaxial bi4ti3o12 thin films.* Journal of Applied Physics, 1998. **84**(8) p. 4428-4435.

152. Karatas, S., et al., *Temperature dependence of characteristic parameters of the h-terminated sn/p-si(100) schottky contacts.* Applied Surface Science, 2003. **217**(1-4) p. 250-260.

153. Rhoderick, E.H. and R.H. Williams, *Metal-semiconductor contacts*. 1988: Claredon Press.

154. Sullivan, J.P., et al., *Electron-transport of inhomogeneous schottky barriers - a numerical study.* Journal of Applied Physics, 1991. **70**(12) p. 7403-7424.

155. Cowley, A.M. and S.M. Sze, *Surface states and barrier height of metal-semiconductor systems.* Journal of Applied Physics, 1965. **36**(10) p. 3212-3220.

156. Card, H.C. and E.H. Rhoderick, *Studies of tunnel mos diodes i. Interface effects in silicon schottky diodes.* Journal of Physics D: Applied Physics, 1971. **4**(10) p. 1589.

157. Hudait, M.K. and S.B. Krupanidhi, *Interface states density distribution in au/n-gaas schottky diodes on n-ge and n-gaas substrates.* Materials Science and Engineering B-Solid State Materials for Advanced Technology, 2001. **87**(2) p. 141-147.

158. Cheung, S.K. and N.W. Cheung, *Extraction of schottky diode parameters from forward current-voltage characteristics.* Applied Physics Letters, 1986. **49**(2) p. 85-87.

159. Hudait, M.K., P. Venkateswarlu, and S.B. Krupanidhi, *Electrical transport characteristics of au/n-gaas schottky diodes on n-ge at low temperatures.* Solid-State Electronics, 2001. **45**(1) p. 133-141.

160. Singh, A., K.C. Reinhardt, and W.A. Anderson, *Temperature-dependence of the electrical characteristics of yb/p-inp tunnel metal-insulator-semiconductor junctions.* Journal of Applied Physics, 1990. **68**(7) p. 3475-3483.

161. Tekeli, Z., et al., *The profile of temperature and voltage dependent series resistance and the interface states in (ni/au)/al(0.3)ga(0.7)n/aln/gan heterostructures.* Microelectronic Engineering, 2008. **85**(11) p. 2316-2321.

162. Turut, A., et al., *Interpreting the nonideal reverse bias c-v characteristics and importance of the dependence of schottky-barrier height on applied voltage.* Physica B, 1995. **205**(1) p. 41-50.

163. Edgar, J.H., *Properties, processing and applications of gallium nitride and related semiconductors*. 1999: INSPEC.

164. Chattopadhyay, P. and B. Raychaudhuri, *New technique for the determination of series resistance of schottky-barrier diodes.* Solid-State Electronics, 1992. **35**(7) p. 1023-1024.

165. Chattopadhyay, P. and B. Raychaudhuri, *Frequency-dependence of forward capacitance voltage characteristics of schottky-barrier diodes.* Solid-State Electronics, 1993. **36**(4) p. 605-610.

166. Werner, J., et al., *Origin of the excess capacitance at intimate schottky contacts.* Physical Review Letters, 1988. **60**(1) p. 53-56.

167. Gadanecz, A., et al., *Thermal stability of metal organic vapor phase epitaxy grown alinn.* Applied Physics Letters, 2007. **90**(22) p. 221906.

168. Kuzmik, J., et al., *Inaln/gan hemts: A first insight into technological optimization.* Electron Devices, IEEE Transactions on, 2006. **53**(3) p. 422-426.

169. Chuan, X., et al., *The leakage current of the schottky contact on the mesa edge of algan/gan heterostructure.* Electron Device Letters, IEEE, 2007. **28**(11) p. 942-944.

170. Hsu, J.W.P., et al., *Inhomogeneous spatial distribution of reverse bias leakage in gan schottky diodes.* Applied Physics Letters, 2001. **78**(12) p. 1685-1687.

171. Iucolano, F., et al., *Barrier inhomogeneity and electrical properties of pt/gan schottky contacts.* Journal of Applied Physics, 2007. **102**(11) p. 113701.

172. Iucolano, F., et al., *Influence of high-temperature gan annealed surface on the electrical properties of ni/gan schottky contacts.* Journal of Applied Physics, 2008. **104**(9) p. 093706.

173. Miller, E.J., et al., *Reduction of reverse-bias leakage current in schottky diodes on gan grown by molecular-beam epitaxy using surface modification with an atomic force microscope.* Journal of Applied Physics, 2002. **91**(12) p. 9821-9826.

174. Mitrofanov, O. and M. Manfra, *Dynamics of trapped charge in gan/algan/gan high electron mobility transistors grown by plasma-*

assisted molecular beam epitaxy. Applied Physics Letters, 2004. **84**(3) p. 422-424.

175. Zhang, H., E.J. Miller, and E.T. Yu, *Analysis of leakage current mechanisms in schottky contacts to gan and al[sub 0.25]ga[sub 0.75]n/gan grown by molecular-beam epitaxy.* Journal of Applied Physics, 2006. **99**(2) p. 023703.

176. Jin-Yu, S., et al., *Oxygen ion implantation isolation planar process for algan/gan hemts.* Electron Device Letters, IEEE, 2007. **28**(6) p. 476-478.

177. Shur, M., *Physics of semiconductor devices*. 1990: Prentice-Hall.

Appendix

A. Microfabrication techniques used in this study

A1. Sample Preparation

First of all, we cut the MOCVD grown samples with an automated dicer. We use diamond saw. Prior to dicing samples are coated with a photoresist (preferably a thicker one i.e. TI35s from Micro-chemicals inc.) for protection. Samples are cut in usually 7 by 7 cm^2 in size.

Subsequent to dicing we must clean the surface of the sample. Usually there are cleaving residues and sometimes some organic dust and photoresist residues on the surface. Getting rid of these contaminants is extremely important because they often make the device either open or short. We have two different cleaning techniques.

First technique is used if there is not significant dirt on the sample. We basically put the sample in acetone for a couple of minutes. Acetone dissociates soft organic residues and it helps to remove the inorganic dirt. While the sample rests in acetone we gently sweep the surface with a q-tip if there is not any features previously made on the sample. Then we put the sample in iso-propilic alcohol to remove the acetone. Finally we put the sample under the running de-ionized (DI) water to get rid of the iso-propilic alcohol. Then we dry the sample using a nitrogen gun. We put the sample on a hot plate at 120°C for 2 min for dehydration when the solvent cleaning over. Afterwards, we examine the sample under an optical microscope if there is any dirt remaining. If so we do this process all over again.

The second technique is used when the sample is very dirty with hard organic residues which cannot be removed by acetone. Note that this method can be used only for bare samples. If there is any previously deposited metal this

method cannot be used. We used so called Piranha Etching technique. We prepare a solution of 3:1 H_2SO_4:H_2O_2. This is an extremely strong solution for organic and metallic materials. We put our sample in this solution for 5-10 min (according to the dirt level of the sample). Then we use DI water to clean the sample. Finally we again use hot plate for dehydration at 120°C for 2 min. typically one round is enough with this technique for cleaning the surface

A2. Photolithography

Photolithography is the most important part of the microfabrication processes. Because it is the part in which we define the features on the sample. Thus it is required in every step. We use a polymer called photoresist which is sensitive to UV light. By exposing with UV over a photomask we transfer the patterns on the mask to the photoresist. Then etching and material deposition can be performed on patterned photoresist.

We use TI35E image reversal photoresist which is sensitive to 360 nm UV light and capable of patterning feature sizes ~1 µm. It can also be used as positive photoresist and it is etch resistant. AZ400K developer is used to remove exposed parts of the photoresist. We utilize Karl Suzz MA6 Mask aligner for positioning and the aligning of the mask.

Then the photoresist is coating is done. The thickness of the photoresist is related to the speed of the spinner. Every step requires its own photoresist thickness. The spin rate is chosen according to the manufacturer's recipe. After the spin samples are pre-baked at 110°C for 120 s.

There are two types of lithography such as positive and image reversal photolithography. The basic difference in these two is that in positive lithography the features on the mask are transferred the same to the sample. That is the closed (dark) features in the mask will be transferred. The advantage of the image reversal photolithography is in the negative wall profile of the photo resist after development. Its desirable to have negative wall profile if a lift-off

process is subsequent. On the contrary if an etch process is aimed, positive wall profile is preferable.

The exposure and the development of the photoresist are done by the manufacturer's guide lines.

A3. Etching

We use inductively coupled reactive ion etching to etch the AlGaN layers. BCl_3 $+Cl_2$ mixture is used as reactants. Reactor pressure was 1 mTorr. The samples were back cooled with He during etching.

A4. Metallization

We have an ultra high vacuum (UHV) e-beam evaporator for metal depositions. Sources are placed in various crucibles according to the manufacturer's specifications. Typical chamber pressure is 5×10^{-6} mbar. Deposited metal thickness is monitored throughout the process via quartz crystal monitor Therefore we can adjust and monitor the deposited metal thickness precisely.

A5. Dielectric Coating

The dielectric coating steps are done in a Plasma Enhanced Chemical Vapor Deposition (PECVD) system in our laboratory. System uses different gases as the reaction precursors. For SiN_x coating we use silane (2% SiH_4+98% N_2) as Si source and ammonia (NH_3) as N source. We basically have a vacuum chamber in which we create plasma of silane and ammonia mixture. The flow rates of each gas are crucial for the composition of the deposited material. The ions of plasma are accelerated towards the sample surface which is heated to 300°C. Then the reaction occurs. Si and N atoms are deposited as SiN_x and the rest is taken out through exhaust.

B. Nanofabrication techniques used in this study

B1. E-beam lithography

We used Raith E-line system for the fabrication of the nanostructures. Poly(methyl methacrylate) (PMMA) 950A is used in almost all processes. The thickness of the resist is altered by intermixing the different concentrations of the resist or by changing the spin rate. Resist is baked at 200°C for 90 s on a hot plate.

Typical exposure base doses are 110 μC/cm^2 for areas, 300 μC/cm for single pixel lines and 0.01pC for single dots at 10 kV accelerating voltage.

We develop the samples with (1:3) methyl-isobutyl-ketone : isopropanol (MIBK:ISO) solution. Typical develop time is calculated as 30 s for first 100nm of resist than 15 s more for each 100nm resist.

C. Publication list in SSI journals

1. Serkan Bütün, Neval Ayşegül Cinel and Ekmel Özbay *GaN Nanoantenna photodetectors enhanced by UV surface plasmons*, Optics Express. December, 2011. (Submitted)

2. Serkan Bütün, Neval Ayşegül Cinel and Ekmel Özbay,U*V-LSPR enhanced GaN MSM photodetectors using Al nano-particles* Nanotechnology. December, 2011.(Submitted)
3. Mutlu Gokkavas, Serkan Bütün, Wlodek Strupinski and Ekmel Özbay *Four-color ultraviolet metal-semiconductor-metal AlGaN photodetectors*, Semicond. Sci. Tech. October, 2011. (Submitted)
4. Arslan, E., S. Butun, Y. Safak, H. Uslu, I. Tascioglu, S. Altindal, and E. Ozbay, *Electrical characterization of MS and MIS structures on AlGaN/AlN/GaN heterostructures.* Microelectronics Reliability, 2011. **51**(2): p. 370-375.

5. Arslan, E., S. Butun, Y. Safak, H. Cakmak, H.B. Yu, and E. Ozbay, *Current transport mechanisms and trap state investigations in (Ni/Au)-*

AlN/GaN Schottky barrier diodes. Microelectronics Reliability, 2011. **51**(3): p. 576-580.

6. Arslan, E., S. Butun, Y. Safak, and E. Ozbay, *Investigation of Trap States in AlInN/AlN/GaN Heterostructures by Frequency-Dependent Admittance Analysis.* Journal of Electronic Materials, 2010. **39**(12): p. 2681-2686.
7. Arslan, E., S. Butun, and E. Ozbay, *Leakage current by Frenkel-Poole emission in Ni/Au Schottky contacts on Al(0.83)In(0.17)N/AlN/GaN heterostructures.* Applied Physics Letters, 2009. **94**(14).
8. Arslan, E., S. Butun, S.B. Lisesivdin, M. Kasap, S. Ozcelik, and E. Ozbay, *The persistent photoconductivity effect in AlGaN/GaN heterostructures grown on sapphire and SiC substrates.* Journal of Applied Physics, 2008. **103**(10).
9. Gokkavas, M., S. Butun, T. Tut, N. Biyikli, and E. Ozbay, *AlGaN-based high-performance metal-semiconductor-metal photodetectors.* Photonics and Nanostructures-Fundamentals and Applications, 2007. **5**(2-3): p. 53-62.
10. Yu, H.B., W. Strupinski, S. Butun, and E. Ozbayl, *Mg-doped AlGaN grown on an AlN/sapphire template by metalorganic chemical vapour deposition.* Physica Status Solidi a-Applications and Materials Science, 2006. **203**(5): p. 868-873.
11. Tut, T., M. Gokkavas, B. Butun, S. Butun, E. Ulker, and E. Ozbay, *Experimental evaluation of impact ionization coefficients in AlxGa1-xN based avalanche photodiodes.* Applied Physics Letters, 2006. **89**(18).
12. Gokkavas, M., S. Butun, H.B. Yu, T. Tut, B. Butun, and E. Ozbay, *Dual-color ultraviolet metal-semiconductor-metal AlGaN photodetectors.* Applied Physics Letters, 2006. **89**(14).

ELSEVIER LICENSE
TERMS AND CONDITIONS

Nov 20, 2011

This is a License Agreement between Serkan Butun ("You") and Elsevier ("Elsevier") provided by Copyright Clearance Center ("CCC"). The license consists of your order details, the terms and conditions provided by Elsevier, and the payment terms and conditions.

All payments must be made in full to CCC. For payment instructions, please see information listed at the bottom of this form.

Supplier	Elsevier Limited The Boulevard,Langford Lane Kidlington,Oxford,OX5 1GB,UK
Registered Company Number	1982084
Customer name	Serkan Butun
Customer address	Nanotechnology Research Center Bilkent
	cankaya, Ankara 06800
License number	2793351194704
License date	Nov 20, 2011
Licensed content publisher	Elsevier
Licensed content publication	Microelectronics Reliability
Licensed content title	Electrical characterization of MS and MIS structures on AlGaN/AlN/GaN heterostructures
Licensed content author	Engin Arslan,Serkan Bütün,Yasemin Şafak,Habibe Uslu,İlke Taşçıoğlu,Şemsettin Altındal,Ekmel Özbay
Licensed content date	February 2011
Licensed content volume number	51
Licensed content issue number	2
Number of pages	6
Start Page	370
End Page	375
Type of Use	reuse in a thesis/dissertation
Portion	full article
Format	both print and electronic
Are you the author of this Elsevier article?	Yes
Will you be translating?	No
Order reference number	
Title of your	AlGaN UV photodetectors: from micro to nano

Estimated size (number of pages)	120
Elsevier VAT number	GB 494 6272 12
Permissions price	0.00 USD
VAT/Local Sales Tax	0.0 USD / 0.0 GBP
Total	0.00 USD

Terms and Conditions

INTRODUCTION

1. The publisher for this copyrighted material is Elsevier. By clicking "accept" in connection with completing this licensing transaction, you agree that the following terms and conditions apply to this transaction (along with the Billing and Payment terms and conditions established by Copyright Clearance Center, Inc. ("CCC"), at the time that you opened your Rightslink account and that are available at any time at http://myaccount.copyright.com).

GENERAL TERMS

2. Elsevier hereby grants you permission to reproduce the aforementioned material subject to the terms and conditions indicated.

3. Acknowledgement: If any part of the material to be used (for example, figures) has appeared in our publication with credit or acknowledgement to another source, permission must also be sought from that source. If such permission is not obtained then that material may not be included in your publication/copies. Suitable acknowledgement to the source must be made, either as a footnote or in a reference list at the end of your publication, as follows:

“Reprinted from Publication title, Vol /edition number, Author(s), Title of article / title of chapter, Pages No., Copyright (Year), with permission from Elsevier [OR APPLICABLE SOCIETY COPYRIGHT OWNER].” Also Lancet special credit - “Reprinted from The Lancet, Vol. number, Author(s), Title of article, Pages No., Copyright (Year), with permission from Elsevier.”

4. Reproduction of this material is confined to the purpose and/or media for which permission is hereby given.

5. Altering/Modifying Material: Not Permitted. However figures and illustrations may be altered/adapted minimally to serve your work. Any other abbreviations, additions, deletions and/or any other alterations shall be made only with prior written authorization of Elsevier Ltd. (Please contact Elsevier at permissions@elsevier.com)

6. If the permission fee for the requested use of our material is waived in this instance, please be advised that your future requests for Elsevier materials may attract a fee.

7. Reservation of Rights: Publisher reserves all rights not specifically granted in the combination of (i) the license details provided by you and accepted in the course of this licensing transaction, (ii) these terms and conditions and (iii) CCC's Billing and Payment terms and conditions.

8. License Contingent Upon Payment: While you may exercise the rights licensed immediately upon issuance of the license at the end of the licensing process for the transaction, provided that you have

Billing and Payment terms and conditions. If full payment is not received on a timely basis, then any license preliminarily granted shall be deemed automatically revoked and shall be void as if never granted. Further, in the event that you breach any of these terms and conditions or any of CCC's Billing and Payment terms and conditions, the license is automatically revoked and shall be void as if never granted. Use of materials as described in a revoked license, as well as any use of the materials beyond the scope of an unrevoked license, may constitute copyright infringement and publisher reserves the right to take any and all action to protect its copyright in the materials.

9. Warranties: Publisher makes no representations or warranties with respect to the licensed material.

10. Indemnity: You hereby indemnify and agree to hold harmless publisher and CCC, and their respective officers, directors, employees and agents, from and against any and all claims arising out of your use of the licensed material other than as specifically authorized pursuant to this license.

11. No Transfer of License: This license is personal to you and may not be sublicensed, assigned, or transferred by you to any other person without publisher's written permission.

12. No Amendment Except in Writing: This license may not be amended except in a writing signed by both parties (or, in the case of publisher, by CCC on publisher's behalf).

13. Objection to Contrary Terms: Publisher hereby objects to any terms contained in any purchase order, acknowledgment, check endorsement or other writing prepared by you, which terms are inconsistent with these terms and conditions or CCC's Billing and Payment terms and conditions. These terms and conditions, together with CCC's Billing and Payment terms and conditions (which are incorporated herein), comprise the entire agreement between you and publisher (and CCC) concerning this licensing transaction. In the event of any conflict between your obligations established by these terms and conditions and those established by CCC's Billing and Payment terms and conditions, these terms and conditions shall control.

14. Revocation: Elsevier or Copyright Clearance Center may deny the permissions described in this License at their sole discretion, for any reason or no reason, with a full refund payable to you. Notice of such denial will be made using the contact information provided by you. Failure to receive such notice will not alter or invalidate the denial. In no event will Elsevier or Copyright Clearance Center be responsible or liable for any costs, expenses or damage incurred by you as a result of a denial of your permission request, other than a refund of the amount(s) paid by you to Elsevier and/or Copyright Clearance Center for denied permissions.

LIMITED LICENSE

The following terms and conditions apply only to specific license types:

15. **Translation**: This permission is granted for non-exclusive world **English** rights only unless your license was granted for translation rights. If you licensed translation rights you may only translate this content into the languages you requested. A professional translator must perform all translations and reproduce the content word for word preserving the integrity of the article. If this license is to re-use 1 or 2 figures then permission is granted for non-exclusive world rights in all languages.

password-protected and made available only to bona fide students registered on a relevant course if:
This license was made in connection with a course,
This permission is granted for 1 year only. You may obtain a license for future website posting,
All content posted to the web site must maintain the copyright information line on the bottom of each image,
A hyper-text must be included to the Homepage of the journal from which you are licensing at http://www.sciencedirect.com/science/journal/xxxxx or the Elsevier homepage for books at http://www.elsevier.com , and
Central Storage: This license does not include permission for a scanned version of the material to be stored in a central repository such as that provided by Heron/XanEdu.

17. **Author website** for journals with the following additional clauses:

All content posted to the web site must maintain the copyright information line on the bottom of each image, and
he permission granted is limited to the personal version of your paper. You are not allowed to download and post the published electronic version of your article (whether PDF or HTML, proof or final version), nor may you scan the printed edition to create an electronic version,
A hyper-text must be included to the Homepage of the journal from which you are licensing at http://www.sciencedirect.com/science/journal/xxxxx , As part of our normal production process, you will receive an e-mail notice when your article appears on Elsevier's online service ScienceDirect (www.sciencedirect.com). That e-mail will include the article's Digital Object Identifier (DOI). This number provides the electronic link to the published article and should be included in the posting of your personal version. We ask that you wait until you receive this e-mail and have the DOI to do any posting.
Central Storage: This license does not include permission for a scanned version of the material to be stored in a central repository such as that provided by Heron/XanEdu.

18. **Author website** for books with the following additional clauses:
Authors are permitted to place a brief summary of their work online only.
A hyper-text must be included to the Elsevier homepage at http://www.elsevier.com

All content posted to the web site must maintain the copyright information line on the bottom of each image
You are not allowed to download and post the published electronic version of your chapter, nor may you scan the printed edition to create an electronic version.
Central Storage: This license does not include permission for a scanned version of the material to be stored in a central repository such as that provided by Heron/XanEdu.

19. **Website** (regular and for author): A hyper-text must be included to the Homepage of the journal from which you are licensing at http://www.sciencedirect.com/science/journal/xxxxx. or for books to the Elsevier homepage at http://www.elsevier.com

20. **Thesis/Dissertation**: If your license is for use in a thesis/dissertation your thesis may be submitted to your institution in either print or electronic form Should your thesis be published

permission for UMI to supply single copies, on demand, of the complete thesis. Should your thesis be published commercially, please reapply for permission.

21. **Other Conditions**:

v1.6

If you would like to pay for this license now, please remit this license along with your payment made payable to "COPYRIGHT CLEARANCE CENTER" otherwise you will be invoiced within 48 hours of the license date. Payment should be in the form of a check or money order referencing your account number and this invoice number RLNK500668330. Once you receive your invoice for this order, you may pay your invoice by credit card. Please follow instructions provided at that time.

Make Payment To:
Copyright Clearance Center
Dept 001
P.O. Box 843006
Boston, MA 02284-3006

For suggestions or comments regarding this order, contact RightsLink Customer Support: customercare@copyright.com or +1-877-622-5543 (toll free in the US) or +1-978-646-2777.

Gratis licenses (referencing $0 in the Total field) are free. Please retain this printable license for your reference. No payment is required.

AMERICAN INSTITUTE OF PHYSICS LICENSE
TERMS AND CONDITIONS

Dec 01, 2011

This is a License Agreement between Serkan Butun ("You") and American Institute of Physics ("AIP") provided by Copyright Clearance Center ("CCC"). The license consists of your order details, the terms and conditions provided by American Institute of Physics , and the payment terms and conditions.

All payments must be made in full to CCC. For payment instructions, please see information listed at the bottom of this form.

License Number	2800491502540
License date	Dec 01, 2011
Licensed content publisher	American Institute of Physics
Licensed content publication	Applied Physics Letters
Licensed content title	Leakage current by Frenkel–Poole emission in Ni/Au Schottky contacts on Al0.83In0.17N/AlN/GaN heterostructures
Licensed content author	Engin Arslan, Serkan Bütün, Ekmel Ozbay
Licensed content date	Apr 8, 2009
Volume number	94
Issue number	14
Type of Use	Thesis/Dissertation
Requestor type	Author (original article)
Format	Print and electronic
Portion	Excerpt (> 800 words)
Will you be translating?	No
Title of your thesis / dissertation	AlGaN UV photodetectors: from micro to nano
Expected completion date	Dec 2011
Estimated size (number of pages)	120
Total	0.00 USD

Terms and Conditions

American Institute of Physics -- Terms and Conditions: Permissions Uses

American Institute of Physics ("AIP") hereby grants to you the non-exclusive right and license to use and/or distribute the Material according to the use specified in your order, on a one-time basis, for the specified term, with a maximum distribution equal to the number that you have ordered. Any links or other content accompanying the Material are not the subject of this license.

1. You agree to include the following copyright and permission notice with the reproduction of the Material: "Reprinted with permission from [FULL CITATION]. Copyright [PUBLICATION YEAR], American Institute of Physics." For an article, the copyright and

Material, in a footnote, or in the reference list.

2. If you have licensed reuse of a figure, photograph, cover, or table, it is your responsibility to ensure that the material is original to AIP and does not contain the copyright of another entity, and that the copyright notice of the figure, photograph, cover, or table does not indicate that it was reprinted by AIP, with permission, from another source. Under no circumstances does AIP, purport or intend to grant permission to reuse material to which it does not hold copyright.
3. You may not alter or modify the Material in any manner. You may translate the Material into another language only if you have licensed translation rights. You may not use the Material for promotional purposes. AIP reserves all rights not specifically granted herein.
4. The foregoing license shall not take effect unless and until AIP or its agent, Copyright Clearance Center, receives the Payment in accordance with Copyright Clearance Center Billing and Payment Terms and Conditions, which are incorporated herein by reference.
5. AIP or the Copyright Clearance Center may, within two business days of granting this license, revoke the license for any reason whatsoever, with a full refund payable to you. Should you violate the terms of this license at any time, AIP, American Institute of Physics, or Copyright Clearance Center may revoke the license with no refund to you. Notice of such revocation will be made using the contact information provided by you. Failure to receive such notice will not nullify the revocation.
6. AIP makes no representations or warranties with respect to the Material. You agree to indemnify and hold harmless AIP, American Institute of Physics, and their officers, directors, employees or agents from and against any and all claims arising out of your use of the Material other than as specifically authorized herein.
7. The permission granted herein is personal to you and is not transferable or assignable without the prior written permission of AIP. This license may not be amended except in a writing signed by the party to be charged.
8. If purchase orders, acknowledgments or check endorsements are issued on any forms containing terms and conditions which are inconsistent with these provisions, such inconsistent terms and conditions shall be of no force and effect. This document, including the CCC Billing and Payment Terms and Conditions, shall be the entire agreement between the parties relating to the subject matter hereof.

This Agreement shall be governed by and construed in accordance with the laws of the State of New York. Both parties hereby submit to the jurisdiction of the courts of New York County for purposes of resolving any disputes that may arise hereunder.

If you would like to pay for this license now, please remit this license along with your payment made payable to "COPYRIGHT CLEARANCE CENTER" otherwise you will be invoiced within 48 hours of the license date. Payment should be in the form of a check or money order referencing your account number and this invoice number RLNK500676172. Once you receive your invoice for this order, you may pay your invoice by credit card. Please follow instructions provided at that time.

Make Payment To:
Copyright Clearance Center
Dept 001
P.O. Box 843006
Boston, MA 02284-3006

For suggestions or comments regarding this order, contact RightsLink Customer Support: customercare@copyright com or +1-877-622-5543 (toll free in the US) or +1-978-646-

license for your reference. No payment is required.

AMERICAN INSTITUTE OF PHYSICS LICENSE TERMS AND CONDITIONS

Dec 01, 2011

This is a License Agreement between Serkan Butun ("You") and American Institute of Physics ("AIP") provided by Copyright Clearance Center ("CCC"). The license consists of your order details, the terms and conditions provided by American Institute of Physics , and the payment terms and conditions.

All payments must be made in full to CCC. For payment instructions, please see information listed at the bottom of this form.

License Number	2800490336991
License date	Dec 01, 2011
Licensed content publisher	American Institute of Physics
Licensed content publication	Journal of Applied Physics
Licensed content title	Electronic band structures and effective-mass parameters of wurtzite GaN and InN
Licensed content author	Y. C. Yeo, T. C. Chong, M. F. Li
Licensed content date	Dec 31, 1969
Volume number	83
Issue number	3
Type of Use	Thesis/Dissertation
Requestor type	Student
Format	Print and electronic
Portion	Figure/Table
Number of figures/tables	1
Title of your thesis / dissertation	AlGaN UV photodetectors: from micro to nano
Expected completion date	Dec 2011
Estimated size (number of pages)	120
Total	0.00 USD

Terms and Conditions

American Institute of Physics -- Terms and Conditions: Permissions Uses

American Institute of Physics ("AIP") hereby grants to you the non-exclusive right and license to use and/or distribute the Material according to the use specified in your order, on a one-time basis, for the specified term, with a maximum distribution equal to the number that you have ordered. Any links or other content accompanying the Material are not the subject of this license.

1. You agree to include the following copyright and permission notice with the reproduction of the Material: "Reprinted with permission from [FULL CITATION]. Copyright [PUBLICATION YEAR], American Institute of Physics." For an article, the copyright and

Material, in a footnote, or in the reference list.

2. If you have licensed reuse of a figure, photograph, cover, or table, it is your responsibility to ensure that the material is original to AIP and does not contain the copyright of another entity, and that the copyright notice of the figure, photograph, cover, or table does not indicate that it was reprinted by AIP, with permission, from another source. Under no circumstances does AIP, purport or intend to grant permission to reuse material to which it does not hold copyright.
3. You may not alter or modify the Material in any manner. You may translate the Material into another language only if you have licensed translation rights. You may not use the Material for promotional purposes. AIP reserves all rights not specifically granted herein.
4. The foregoing license shall not take effect unless and until AIP or its agent, Copyright Clearance Center, receives the Payment in accordance with Copyright Clearance Center Billing and Payment Terms and Conditions, which are incorporated herein by reference.
5. AIP or the Copyright Clearance Center may, within two business days of granting this license, revoke the license for any reason whatsoever, with a full refund payable to you. Should you violate the terms of this license at any time, AIP, American Institute of Physics, or Copyright Clearance Center may revoke the license with no refund to you. Notice of such revocation will be made using the contact information provided by you. Failure to receive such notice will not nullify the revocation.
6. AIP makes no representations or warranties with respect to the Material. You agree to indemnify and hold harmless AIP, American Institute of Physics, and their officers, directors, employees or agents from and against any and all claims arising out of your use of the Material other than as specifically authorized herein.
7. The permission granted herein is personal to you and is not transferable or assignable without the prior written permission of AIP. This license may not be amended except in a writing signed by the party to be charged.
8. If purchase orders, acknowledgments or check endorsements are issued on any forms containing terms and conditions which are inconsistent with these provisions, such inconsistent terms and conditions shall be of no force and effect. This document, including the CCC Billing and Payment Terms and Conditions, shall be the entire agreement between the parties relating to the subject matter hereof.

This Agreement shall be governed by and construed in accordance with the laws of the State of New York. Both parties hereby submit to the jurisdiction of the courts of New York County for purposes of resolving any disputes that may arise hereunder.

If you would like to pay for this license now, please remit this license along with your payment made payable to "COPYRIGHT CLEARANCE CENTER" otherwise you will be invoiced within 48 hours of the license date. Payment should be in the form of a check or money order referencing your account number and this invoice number RLNK500676166. Once you receive your invoice for this order, you may pay your invoice by credit card. Please follow instructions provided at that time.

Make Payment To:
Copyright Clearance Center
Dept 001
P.O. Box 843006
Boston, MA 02284-3006

For suggestions or comments regarding this order, contact RightsLink Customer Support: customercare@copyright com or +1-877-622-5543 (toll free in the US) or +1-978-646-

license for your reference. No payment is required.

AMERICAN INSTITUTE OF PHYSICS LICENSE TERMS AND CONDITIONS

Dec 01, 2011

This is a License Agreement between Serkan Butun ("You") and American Institute of Physics ("AIP") provided by Copyright Clearance Center ("CCC"). The license consists of your order details, the terms and conditions provided by American Institute of Physics , and the payment terms and conditions.

All payments must be made in full to CCC. For payment instructions, please see information listed at the bottom of this form.

License Number	2800491131955
License date	Dec 01, 2011
Licensed content publisher	American Institute of Physics
Licensed content publication	Applied Physics Letters
Licensed content title	Dual-color ultraviolet metal-semiconductor-metal AlGaN photodetectors
Licensed content author	Mutlu Gökkavas, Serkan Butun, HongBo Yu, Turgut Tut, et al.
Licensed content date	Oct 2, 2006
Volume number	89
Issue number	14
Type of Use	Thesis/Dissertation
Requestor type	Author (original article)
Format	Print and electronic
Portion	Excerpt (> 800 words)
Will you be translating?	No
Title of your thesis / dissertation	AlGaN UV photodetectors: from micro to nano
Expected completion date	Dec 2011
Estimated size (number of pages)	120
Total	0.00 USD

Terms and Conditions

American Institute of Physics -- Terms and Conditions: Permissions Uses

American Institute of Physics ("AIP") hereby grants to you the non-exclusive right and license to use and/or distribute the Material according to the use specified in your order, on a one-time basis, for the specified term, with a maximum distribution equal to the number that you have ordered. Any links or other content accompanying the Material are not the subject of this license.

1. You agree to include the following copyright and permission notice with the reproduction of the Material: "Reprinted with permission from [FULL CITATION]. Copyright [PUBLICATION YEAR], American Institute of Physics." For an article, the copyright and

Material, in a footnote, or in the reference list.

2. If you have licensed reuse of a figure, photograph, cover, or table, it is your responsibility to ensure that the material is original to AIP and does not contain the copyright of another entity, and that the copyright notice of the figure, photograph, cover, or table does not indicate that it was reprinted by AIP, with permission, from another source. Under no circumstances does AIP, purport or intend to grant permission to reuse material to which it does not hold copyright.
3. You may not alter or modify the Material in any manner. You may translate the Material into another language only if you have licensed translation rights. You may not use the Material for promotional purposes. AIP reserves all rights not specifically granted herein.
4. The foregoing license shall not take effect unless and until AIP or its agent, Copyright Clearance Center, receives the Payment in accordance with Copyright Clearance Center Billing and Payment Terms and Conditions, which are incorporated herein by reference.
5. AIP or the Copyright Clearance Center may, within two business days of granting this license, revoke the license for any reason whatsoever, with a full refund payable to you. Should you violate the terms of this license at any time, AIP, American Institute of Physics, or Copyright Clearance Center may revoke the license with no refund to you. Notice of such revocation will be made using the contact information provided by you. Failure to receive such notice will not nullify the revocation.
6. AIP makes no representations or warranties with respect to the Material. You agree to indemnify and hold harmless AIP, American Institute of Physics, and their officers, directors, employees or agents from and against any and all claims arising out of your use of the Material other than as specifically authorized herein.
7. The permission granted herein is personal to you and is not transferable or assignable without the prior written permission of AIP. This license may not be amended except in a writing signed by the party to be charged.
8. If purchase orders, acknowledgments or check endorsements are issued on any forms containing terms and conditions which are inconsistent with these provisions, such inconsistent terms and conditions shall be of no force and effect. This document, including the CCC Billing and Payment Terms and Conditions, shall be the entire agreement between the parties relating to the subject matter hereof.

This Agreement shall be governed by and construed in accordance with the laws of the State of New York. Both parties hereby submit to the jurisdiction of the courts of New York County for purposes of resolving any disputes that may arise hereunder.

If you would like to pay for this license now, please remit this license along with your payment made payable to "COPYRIGHT CLEARANCE CENTER" otherwise you will be invoiced within 48 hours of the license date. Payment should be in the form of a check or money order referencing your account number and this invoice number RLNK500676170. Once you receive your invoice for this order, you may pay your invoice by credit card. Please follow instructions provided at that time.

Make Payment To:
Copyright Clearance Center
Dept 001
P.O. Box 843006
Boston, MA 02284-3006

For suggestions or comments regarding this order, contact RightsLink Customer Support: customercare@copyright com or +1-877-622-5543 (toll free in the US) or +1-978-646-

license for your reference. No payment is required.

ELSEVIER LICENSE
TERMS AND CONDITIONS

Dec 01, 2011

This is a License Agreement between Serkan Butun ("You") and Elsevier ("Elsevier") provided by Copyright Clearance Center ("CCC"). The license consists of your order details, the terms and conditions provided by Elsevier, and the payment terms and conditions.

All payments must be made in full to CCC. For payment instructions, please see information listed at the bottom of this form.

Supplier	Elsevier Limited The Boulevard,Langford Lane Kidlington,Oxford,OX5 1GB,UK
Registered Company Number	1982084
Customer name	Serkan Butun
Customer address	Nanotechnology Research Center Bilkent
	cankaya, Ankara 06800
License number	2800491363918
License date	Dec 01, 2011
Licensed content publisher	Elsevier
Licensed content publication	Microelectronics Reliability
Licensed content title	Current transport mechanisms and trap state investigations in (Ni/Au)–AlN/GaN Schottky barrier diodes
Licensed content author	Engin Arslan,Serkan Bütün,Yasemin Şafak,Hüseyin Çakmak,Hongbo Yu,Ekmel Özbay
Licensed content date	March 2011
Licensed content volume number	51
Licensed content issue number	3
Number of pages	5
Start Page	576
End Page	580
Type of Use	reuse in a thesis/dissertation
Intended publisher of new work	other
Portion	full article
Format	both print and electronic
Are you the author of this Elsevier article?	Yes
Will you be translating?	No

Expected completion date	Dec 2011
Estimated size (number of pages)	120
Elsevier VAT number	GB 494 6272 12
Permissions price	0.00 USD
VAT/Local Sales Tax	0.0 USD / 0.0 GBP
Total	0.00 USD
Terms and Conditions	

INTRODUCTION

1. The publisher for this copyrighted material is Elsevier. By clicking "accept" in connection with completing this licensing transaction, you agree that the following terms and conditions apply to this transaction (along with the Billing and Payment terms and conditions established by Copyright Clearance Center, Inc. ("CCC"), at the time that you opened your Rightslink account and that are available at any time at http://myaccount.copyright.com).

GENERAL TERMS

2. Elsevier hereby grants you permission to reproduce the aforementioned material subject to the terms and conditions indicated.

3. Acknowledgement: If any part of the material to be used (for example, figures) has appeared in our publication with credit or acknowledgement to another source, permission must also be sought from that source. If such permission is not obtained then that material may not be included in your publication/copies. Suitable acknowledgement to the source must be made, either as a footnote or in a reference list at the end of your publication, as follows:

“Reprinted from Publication title, Vol /edition number, Author(s), Title of article / title of chapter, Pages No., Copyright (Year), with permission from Elsevier [OR APPLICABLE SOCIETY COPYRIGHT OWNER].” Also Lancet special credit - “Reprinted from The Lancet, Vol. number, Author(s), Title of article, Pages No., Copyright (Year), with permission from Elsevier.”

4. Reproduction of this material is confined to the purpose and/or media for which permission is hereby given.

5. Altering/Modifying Material: Not Permitted. However figures and illustrations may be altered/adapted minimally to serve your work. Any other abbreviations, additions, deletions and/or any other alterations shall be made only with prior written authorization of Elsevier Ltd. (Please contact Elsevier at permissions@elsevier.com)

6. If the permission fee for the requested use of our material is waived in this instance, please be advised that your future requests for Elsevier materials may attract a fee.

7. Reservation of Rights: Publisher reserves all rights not specifically granted in the combination of (i) the license details provided by you and accepted in the course of this licensing transaction, (ii) these terms and conditions and (iii) CCC's Billing and Payment terms and conditions.

8 Li C ti t U P t Whil i th i ht li d i di t l

and until full payment is received from you (either by publisher or by CCC) as provided in CCC's Billing and Payment terms and conditions. If full payment is not received on a timely basis, then any license preliminarily granted shall be deemed automatically revoked and shall be void as if never granted. Further, in the event that you breach any of these terms and conditions or any of CCC's Billing and Payment terms and conditions, the license is automatically revoked and shall be void as if never granted. Use of materials as described in a revoked license, as well as any use of the materials beyond the scope of an unrevoked license, may constitute copyright infringement and publisher reserves the right to take any and all action to protect its copyright in the materials.

9. Warranties: Publisher makes no representations or warranties with respect to the licensed material.

10. Indemnity: You hereby indemnify and agree to hold harmless publisher and CCC, and their respective officers, directors, employees and agents, from and against any and all claims arising out of your use of the licensed material other than as specifically authorized pursuant to this license.

11. No Transfer of License: This license is personal to you and may not be sublicensed, assigned, or transferred by you to any other person without publisher's written permission.

12. No Amendment Except in Writing: This license may not be amended except in a writing signed by both parties (or, in the case of publisher, by CCC on publisher's behalf).

13. Objection to Contrary Terms: Publisher hereby objects to any terms contained in any purchase order, acknowledgment, check endorsement or other writing prepared by you, which terms are inconsistent with these terms and conditions or CCC's Billing and Payment terms and conditions. These terms and conditions, together with CCC's Billing and Payment terms and conditions (which are incorporated herein), comprise the entire agreement between you and publisher (and CCC) concerning this licensing transaction. In the event of any conflict between your obligations established by these terms and conditions and those established by CCC's Billing and Payment terms and conditions, these terms and conditions shall control.

14. Revocation: Elsevier or Copyright Clearance Center may deny the permissions described in this License at their sole discretion, for any reason or no reason, with a full refund payable to you. Notice of such denial will be made using the contact information provided by you. Failure to receive such notice will not alter or invalidate the denial. In no event will Elsevier or Copyright Clearance Center be responsible or liable for any costs, expenses or damage incurred by you as a result of a denial of your permission request, other than a refund of the amount(s) paid by you to Elsevier and/or Copyright Clearance Center for denied permissions.

LIMITED LICENSE

The following terms and conditions apply only to specific license types:

15. **Translation**: This permission is granted for non-exclusive world **English** rights only unless your license was granted for translation rights. If you licensed translation rights you may only translate this content into the languages you requested. A professional translator must perform all translations and reproduce the content word for word preserving the integrity of the article. If this license is to re-use 1 or 2 figures then permission is granted for non-exclusive world rights in all

Electronic reserve: If licensed material is to be posted to website, the web site is to be password-protected and made available only to bona fide students registered on a relevant course if:
This license was made in connection with a course,
This permission is granted for 1 year only. You may obtain a license for future website posting,
All content posted to the web site must maintain the copyright information line on the bottom of each image,
A hyper-text must be included to the Homepage of the journal from which you are licensing at http://www.sciencedirect.com/science/journal/xxxxx or the Elsevier homepage for books at http://www.elsevier.com , and
Central Storage: This license does not include permission for a scanned version of the material to be stored in a central repository such as that provided by Heron/XanEdu.

17. **Author website** for journals with the following additional clauses:

All content posted to the web site must maintain the copyright information line on the bottom of each image, and
he permission granted is limited to the personal version of your paper. You are not allowed to download and post the published electronic version of your article (whether PDF or HTML, proof or final version), nor may you scan the printed edition to create an electronic version,
A hyper-text must be included to the Homepage of the journal from which you are licensing at http://www.sciencedirect.com/science/journal/xxxxx , As part of our normal production process, you will receive an e-mail notice when your article appears on Elsevier's online service ScienceDirect (www.sciencedirect.com). That e-mail will include the article's Digital Object Identifier (DOI). This number provides the electronic link to the published article and should be included in the posting of your personal version. We ask that you wait until you receive this e-mail and have the DOI to do any posting.
Central Storage: This license does not include permission for a scanned version of the material to be stored in a central repository such as that provided by Heron/XanEdu.

18. **Author website** for books with the following additional clauses:
Authors are permitted to place a brief summary of their work online only.
A hyper-text must be included to the Elsevier homepage at http://www.elsevier.com

All content posted to the web site must maintain the copyright information line on the bottom of each image
You are not allowed to download and post the published electronic version of your chapter, nor may you scan the printed edition to create an electronic version.
Central Storage: This license does not include permission for a scanned version of the material to be stored in a central repository such as that provided by Heron/XanEdu.

19. **Website** (regular and for author): A hyper-text must be included to the Homepage of the journal from which you are licensing at http://www.sciencedirect.com/science/journal/xxxxx. or for books to the Elsevier homepage at http://www.elsevier.com

20 **Thesis/Dissertation**: If your license is for use in a thesis/dissertation your thesis may be

and Archives of Canada to supply single copies, on demand, of the complete thesis and include permission for UMI to supply single copies, on demand, of the complete thesis. Should your thesis be published commercially, please reapply for permission.

21. **Other Conditions**:

v1.6

If you would like to pay for this license now, please remit this license along with your payment made payable to "COPYRIGHT CLEARANCE CENTER" otherwise you will be invoiced within 48 hours of the license date. Payment should be in the form of a check or money order referencing your account number and this invoice number RLNK500676171. Once you receive your invoice for this order, you may pay your invoice by credit card. Please follow instructions provided at that time.

Make Payment To:
Copyright Clearance Center
Dept 001
P.O. Box 843006
Boston, MA 02284-3006

For suggestions or comments regarding this order, contact RightsLink Customer Support: customercare@copyright.com or +1-877-622-5543 (toll free in the US) or +1-978-646-2777.

Gratis licenses (referencing $0 in the Total field) are free. Please retain this printable license for your reference. No payment is required.

AMERICAN INSTITUTE OF PHYSICS LICENSE TERMS AND CONDITIONS

Dec 01, 2011

This is a License Agreement between Serkan Butun ("You") and American Institute of Physics ("AIP") provided by Copyright Clearance Center ("CCC"). The license consists of your order details, the terms and conditions provided by American Institute of Physics , and the payment terms and conditions.

All payments must be made in full to CCC. For payment instructions, please see information listed at the bottom of this form.

License Number	2800490798464
License date	Dec 01, 2011
Licensed content publisher	American Institute of Physics
Licensed content publication	Journal of Applied Physics
Licensed content title	Optical constants of epitaxial AlGaN films and their temperature dependence
Licensed content author	D. Brunner, H. Angerer, E. Bustarret, F. Freudenberg, et al.
Licensed content date	Nov 15, 1997
Volume number	82
Issue number	10
Type of Use	Thesis/Dissertation
Requestor type	Student
Format	Print and electronic
Portion	Figure/Table
Number of figures/tables	1
Title of your thesis / dissertation	AlGaN UV photodetectors: from micro to nano
Expected completion date	Dec 2011
Estimated size (number of pages)	120
Total	0.00 USD

Terms and Conditions

American Institute of Physics -- Terms and Conditions: Permissions Uses

American Institute of Physics ("AIP") hereby grants to you the non-exclusive right and license to use and/or distribute the Material according to the use specified in your order, on a one-time basis, for the specified term, with a maximum distribution equal to the number that you have ordered. Any links or other content accompanying the Material are not the subject of this license.

1. You agree to include the following copyright and permission notice with the reproduction of the Material: "Reprinted with permission from [FULL CITATION]. Copyright [PUBLICATION YEAR], American Institute of Physics." For an article, the copyright and

Material, in a footnote, or in the reference list.

2. If you have licensed reuse of a figure, photograph, cover, or table, it is your responsibility to ensure that the material is original to AIP and does not contain the copyright of another entity, and that the copyright notice of the figure, photograph, cover, or table does not indicate that it was reprinted by AIP, with permission, from another source. Under no circumstances does AIP, purport or intend to grant permission to reuse material to which it does not hold copyright.
3. You may not alter or modify the Material in any manner. You may translate the Material into another language only if you have licensed translation rights. You may not use the Material for promotional purposes. AIP reserves all rights not specifically granted herein.
4. The foregoing license shall not take effect unless and until AIP or its agent, Copyright Clearance Center, receives the Payment in accordance with Copyright Clearance Center Billing and Payment Terms and Conditions, which are incorporated herein by reference.
5. AIP or the Copyright Clearance Center may, within two business days of granting this license, revoke the license for any reason whatsoever, with a full refund payable to you. Should you violate the terms of this license at any time, AIP, American Institute of Physics, or Copyright Clearance Center may revoke the license with no refund to you. Notice of such revocation will be made using the contact information provided by you. Failure to receive such notice will not nullify the revocation.
6. AIP makes no representations or warranties with respect to the Material. You agree to indemnify and hold harmless AIP, American Institute of Physics, and their officers, directors, employees or agents from and against any and all claims arising out of your use of the Material other than as specifically authorized herein.
7. The permission granted herein is personal to you and is not transferable or assignable without the prior written permission of AIP. This license may not be amended except in a writing signed by the party to be charged.
8. If purchase orders, acknowledgments or check endorsements are issued on any forms containing terms and conditions which are inconsistent with these provisions, such inconsistent terms and conditions shall be of no force and effect. This document, including the CCC Billing and Payment Terms and Conditions, shall be the entire agreement between the parties relating to the subject matter hereof.

This Agreement shall be governed by and construed in accordance with the laws of the State of New York. Both parties hereby submit to the jurisdiction of the courts of New York County for purposes of resolving any disputes that may arise hereunder.

If you would like to pay for this license now, please remit this license along with your payment made payable to "COPYRIGHT CLEARANCE CENTER" otherwise you will be invoiced within 48 hours of the license date. Payment should be in the form of a check or money order referencing your account number and this invoice number RLNK500676167. Once you receive your invoice for this order, you may pay your invoice by credit card. Please follow instructions provided at that time.

Make Payment To:
Copyright Clearance Center
Dept 001
P.O. Box 843006
Boston, MA 02284-3006

For suggestions or comments regarding this order, contact RightsLink Customer Support: customercare@copyright com or +1-877-622-5543 (toll free in the US) or +1-978-646-

license for your reference. No payment is required.